UNIVERSITY OF SOUTHAMPTON

The estimation of bubble populations in the surf-zone by inversion of acoustic propagation

by Steven Douglas Meers

Doctor of Philosophy

Faculty of Engineering and Applied Science
Institute of Sound and Vibration Research

May 2005

UNIVERSITY OF SOUTHAMPTON

ABSTRACT

FACULTY OF ENGINEERING AND APPLIED SCIENCE
INSTITUTE OF SOUND AND VIBRATION RESEARCH

Doctor of Philosophy

THE ESTIMATION OF BUBBLE POPULATIONS IN THE SURF-ZONE BY INVERSION OF ACOUSTIC PROPAGATION

by Steven Douglas Meers

For several decades the propagation characteristics of acoustic pulses (attenuation and sound speed) have been inverted in attempts to measure the size distributions of gas bubbles in liquids. Primarily this has been attempted in the ocean for defence and environmental purposes, however there are a growing number of biomedical and industrial applications. In order to simplify the inversion, previous investigators have assumed that that the bubbles are undergoing linear, steady-state monochromatic pulsations in a free field, without interacting. These assumptions are always contravened to some extent. This study examines the validity of the assumptions and identifies the need for a new time-dependent nonlinear method of determining a bubble's extinction cross section. Such a model is developed and employed in an experiment to estimate the bubble population in the surf-zone, an important but seldom measured region of the ocean, where large populations of bubbles are generated by breaking waves. The necessary theoretical framework to exploit this new model (based on the current state-of-the-art technique) is developed and employs a new method of determining the optimal regularisation parameter for use in the inversion process. A series of laboratory tests and surf-zone sea trials are described that result in a set of bubble populations calculated using linear and, for the first time, nonlinear techniques.

Contents

List of Figures

List of Symbols

A	attenuation per unit length due to the presence of bubbles
A_i	attenuation measured at the i^{th} measurement position
a	length of a line of point sources
a_1	the point source at one end of a line of point sources
a_2	the point source at the opposite extremity (to a_1) of a line of point sources
B	bulk modulus
B_w	bulk modulus of a bubble-free liquid
B_g	bulk modulus of a gas
B_h	the linear B-spline in the h^{th} radius bin
B_c	bulk modulus of a bubble cloud
b_{RF}	the linear damping constant of a bubble in the radius-force frame
C	curvature
c_{ph}	plane wave phase speed
c_w	sound speed in a bubble-free liquid
c_g	sound speed in a gas
c_c	sound speed in a bubble cloud
c_{bin}	approximation to the sound speed in a bubble cloud made using a binomial expansion
D_g	thermal diffusivity of a gas
d	near-field extent of an acoustic source
d_{tot}	the total dimensionless damping constant of a bubble
d_{rad}	the radiation dimensionless damping constant of a bubble
d_{th}	the thermal dimensionless damping constant of a bubble

d_{vis}	the viscous dimensionless damping constant of a bubble
E_{loop}	the energy subtracted from a bubble per cycle of the insonifying pulse
e	the exponent in a binomial expansion
f	frequency
f_0	the resonance frequency of a bubble
f_{res}	resonant frequency of an element in an acoustic source
f_{low}	low frequency extent of the band of an acoustic source
f_{high}	high frequency extends of the band of an acoustic source
G	total number of frequencies
g	index in a discrete set of frequencies
H_i^b	the amplitude of the fourier transform in bubbly conditions at the i^{th} measurement position
H_i^{bf}	the amplitude of the fourier transform in bubble-free conditions at the i^{th} measurement position
H	total number of bubble radii
h	index in a discrete set of bubble radii
I	acoustic intensity
I_b	acoustic intensity in a bubbly environment
I_{bf}	acoustic intensity in a bubble-free environment
I_0	the acoustic intensity at 1 metre from a source
i	index of measurement positions
j	$\sqrt{-1}$
K	a matrix representing the response of the bubbles in a cloud
K_w	compressibility of water
K_g	compressibility of gas
K_c	compressibility of a bubble cloud
K_{bub}	compressibility of all the bubbles within a cloud
k_c	the complex wavenumber of a sound propagating in a bubbly medium
k_e	the effective complex wavenumber through a cloud of interacting bubbles
k_{RF}	the damping constant (in the radius-force frame) of a bubble when represented as a linear oscillator

l_D	thickness of the thermal boundary layer in a bubble
L_p	acoustic pulse length (pulse duration × sound speed)
m_{RF}^{rad}	the radiation mass of a bubble in the radius-force frame
n	the number of bubbles per unit volume having equilibrium radius between R_0 and $R_0 + dR_0$
N	the total number of bubbles in a cloud having equilibrium radius between R_0 and $R_0 + dR_0$
N_{tot}	the number of bubbles in a cloud all having the same radius
0 P	acoustic pressure
P_A	amplitude of driving pressure
P_{tot}	total pressure
p	spatially varying complex pressure
p_0	the hydrostatic pressure in the liquid outside the bubble
$p_{blocked}$	the pressure seen if a bubble were replaced by a rigid sphere of equal radius
p_{dyn}	the pressure within a bubble caused by the motion of the liquid when the bubble is displaced
p_g	the instantaneous gas pressure within a bubble
p_i	the instantaneous total internal pressure within a bubble
p_L	the pressure in the liquid outside the bubble wall
p_v	the vapour pressure within a bubble
p_σ	the pressure within a bubble due to surface tension
p_∞	the pressure at some point remote from a bubble wall
Q	the heat transfer to a gas
R	the instantaneous radius of a spherical bubble
R_0	the equilibrium radius of a spherical bubble
R_ϵ	the displacement of a bubble's radius from equilibrium
R_{res}	the resonant bubble radii
S	entropy
s	the largest dimension of an element in an acoustic source
t	time

t_p	arrival time of multiple path reflections at reciver
U	the internal energy of a gas
u	real part of the complex sound speed c_c
v	imaginary part of the complex sound speed c_c
V	the instantaneous volume of a single bubble
$V_{2\omega}$	the 2nd harmonic response of a bubble
$V_{3\omega}$	the 3rd harmonic response of a bubble
V_0	the equilibrium volume of a single bubble
V_w	volume of a bubble-free liquid (an additional subscript l denotes that value in the l^{th} layer of a multi-layer cloud
V_g	volume of gas (an additional subscript l denotes that value in the l^{th} layer of a multi-layer cloud
V_c	volume of a bubble cloud (an additional subscript l denotes that value in the l^{th} layer of a multi-layer cloud
$V_{i\rightarrow i+1}$	the sampling volume defined by two measuring positions
V_F	void fraction
W	power
w	the work done by a gas
$\langle W \rangle$	time averaged power
x	distance co-ordinate
x_d	distance between two measurement positions
x_i	distance to the i$^{\text{th}}$ measurement position
x_r	vertical standoff between source/receiver and the nearest reflecting surface
x_p	perpendicular distance from a line array of point sources
z	depth
α	acoustic propagation characteristics, i.e. phase speed and attenuation
β	regularisation parameter
β_{tot}	the frame-independent linear total damping constant
β_{vis}	the frame-independent linear viscous damping constant
β_{th}	the frame-independent linear thermal damping constant

β_{rad}	the frame-independent linear radiation damping constant
β_{ve}	effective viscous resistive constant leading to damping
β_{te}	effective thermal resistive constant leading to damping
β_{re}	effective acoustic radiation resistive constant leading to damping
γ	the ratio of the specific heat of a gas at constant pressure to that at constant volume
δ_{tot}	the total dimensionless damping constant of a bubble evaluated at resonance
ξ_c	a function equivalent to the square root of the ratio of the bulk modulus of a bubble cloud to its density (an additional subscript l denotes that value in the l^{th} layer of a multi-layer cloud
η	shear viscosity
θ	angle
θ_{bw}	the beamwidth of an acoustic source
θ_{low}	the beamwidth of an acoustic source at its lower frequency bound
θ_{high}	the beamwidth of an acoustic source at its upper frequency bound
κ	polytropic index of a gas
λ	wavelength
Ψ	least squares cost function
ρ_w	density of a bubble-free liquid
ρ_g	density of a gas
ρ_c	density of a a bubble cloud
σ	the surface tension of a liquid
φ	ratio of a bubbles radius to the width of its thermal boundary layer R_0/l_D
ω	angular frequency ($\omega = 2\pi f$)
ω_0	angular resonance frequency of a bubble
Ω_b^{abs}	the absorption cross section of a single bubble
Ω_b^{ext}	the extinction cross section of a single bubble
Ω_b^{scat}	the scattering cross section of a single bubble
Ω_c^{ext}	the total extinction cross section per unit volume presented by the bubbles in a cloud

Publications

- Leighton, T. G., Meers, S. D. & White, P. R., *Propagation through nonlinear time-dependent bubble clouds, and the estimation of bubble populations from measured acoustic characteristics*, Proc. R. Soc. Lond. A, **460**, 2521-2550

- Rhodes, C. & Meers, S. D., *Poster: The acoustic detection of high energy neutrinos*, Dstl Internal Symposium. University of Oxford, 2003

- Meers, S. D. & Leighton, T. G., *Poster: The rapid assessment of bubble populations in a shallow water environment*, EPSRC Theme day on Acoustics, Institute of Acoustics 2002 Spring conference

- Meers, S. D., Leighton, T. G., Clarke, J. W. L., Heald, G. J., Dumbrell, H. A. & White, P. R., *The importance of bubble ring-up and pulse length in estimating the bubble distribution from acoustic propagation measurements*, in 'Acoustical Oceanography' (eds. T. G. Leighton, G. J. Heald, H. Griffiths & G. Griffiths), Proc. Inst. Acoust. **23**(2), 235-241

- Leighton, T. G., Meers, S. D., Simpson, M. D., Clarke, J. W. L., Yim, G. T., Birkin, P. R., Watson, Y. E., White, P. R., Heald, G. J., Dumbrell, H. A., Culver, R. L. & Richards, S. D. *The Hurst Spit experiment: The characterisation of bubbles in the surf zone using multiple acoustic techniques*, in 'Acoustical Oceanography' (eds. T. G. Leighton, G. J. Heald, H. Griffiths & G. Griffiths), Proc. Inst. Acoust. **23**(2), 227-234

- Meers, S. D., Simpson, M. D. & Leighton, T. G., *Feasibility study for an ultrasonic flow system*, ISVR Technical Report, University of Southampton, 2000

- Leighton, T. G., Simpson, M. D., Clarke, J. W. L. & Meers, S. D., *A Report on the Development of an Algorithm that Incorporates Depth Dependence in the Dispersion Relation for Bubbly Media*, ISVR Contract Report No. 00/07, University of Southampton, 2000.

Awards

- Institute of Acoustics conference 'Acoustical Oceanography', 2001 Southampton Oceanography Centre, 9 - 12 April 2001

  - Best student prize for paper, poster and oral presentation.

    Prize awarded by an international panel of judges.

Acknowledgements

This work was carried out under a full-time PhD studentship funded by the Engineering and Physical Science Research Council (Grant number GR/M38094) and to them I express my gratitude for their support and funding. I have been extremely fortunate to be involved in a fascinating area of research and that has involved the full spectrum of research activity from theory, through laboratory to the real world.

I am indebted to my PhD supervisor, Professor Tim Leighton, for his tireless support and encouragement throughout this study. His rigorous scientific approach, careful attention to detail, unending enthusiasm and approachable manner have enabled me to overcome many obstacles and have taught me many lessons for the future. I am also extremely grateful to Dr. Paul White for numerous instances of help where he translated the seemingly incomprehensible into plain English. Additionally I particularly owe thanks to Professor Chris Morfey who helped refine the theory behind the non-linear theory presented here, Professor Phil Nelson who helped me understand the finer points of matrix inversion and Dr. Peter Birkin & Dr. Justin Dix for chemical analysis of sea water specimens (and coming along to laugh at our attempts at the beach, see figure 5.5). My thanks also go to many other members of the academic staff at ISVR, who were all extremely supportive throughout my time there.

With a large practical element forming part of this study the academic input would have proven fruitless without practical support from the technical staff at ISVR. I would like to thank John Taylor for all his help and

advice regarding many hopelessly impractical ideas, Tony Edgeley & Rob Stainsbridge for building a complex and robust electronic rig without which no data could have been collected and Keith Sims and the other technicians for numerous instances of practical help. Also on the practical side I would like to thank New Forest District Council for the use of their facilities at Hurst Spit and for permission to conduct both sets of sea trials.

I am also grateful to a number of other associates over the course of my studies. Mr. Hugh Dumbrell for providing MATLAB code to solve the Herring-Keller equation, Dr. Simon Richards for modelling the effect of suspended sediments and Mr. Paul Doust for enthusiastic support and hard-work designing an acoustic source suitable for our experiments. I would also like to thank Sue Brindle and Maureen Strickland at ISVR for their extremely efficient but equally friendly secretarial support. To my fellow PhD students I would like to offer thanks for many instances of support and a large number of very funny and memorable moments throughout the study.

I would like to thank my parents for all their unconditional support over the years and attempts to understand what on earth it is all about - here's hoping the photograph is a little better this time around! Finally, and most importantly, Christine, sorry for all the deadlines I've missed and all the evenings I've spent chained to the computer and thank you for all the love and support you have given me over the first few years of our marriage.

Do not worry about your difficulties in Mathematics.
I can assure you mine are still greater.
Albert Einstein (1879 - 1955)

Chapter 1

Introduction

The study of acoustic propagation in the ocean is a field which has been the subject of a large amount of research over many years. It has spawned a huge range of applications as diverse as measuring the speed of sound in the ocean in order to investigate global warming [1], the estimation of fish stocks [2] and the location of stranded air-men in the Atlantic Ocean [3].

Bubbles are an important physical phenomena in the ocean. It has been estimated [4] that the flux of atmospheric carbon between atmosphere and ocean exceeds 1000 million tonnes per annum. This estimate makes no account of bubble activity which could dramatically increase this figure. Hence the estimation of bubble populations is potentially of benefit to climate modelling and the understanding of global warming, as well as being of interest to physical oceanographers. In addition, the presence of bubbles has a significant impact on the propagation of sound in the ocean owing to the high efficiency of bubbles as acoustic scatterers [5]. Understanding of propagation in bubbly environments is of key importance in a number of defence and commercial applications [5] and is dependent upon the size distribution of the bubbles in the medium.

As a result of the scattering efficiency of a bubble, techniques based upon acoustics have proven the most successful at determining bubble populations in an oceanic environment. Of these techniques, the most widely used is

inversion of acoustic propagation characteristics and this is the subject considered herein. Given the long history of this technique it is surprising the assumptions inherent within it are still extensive and, providing the technique produces a plausible solution, the temptation is to accept that solution without examining the extent to which the assumptions have been contravened. This is especially true when making measurements in the surf-zone, an important region in which few measurements [6 9] have been made. This study attempts to estimate bubble populations in the surf-zone and will examine the validity of the assumptions inherent in that estimate.

This chapter serves as an introduction to the field and reviews landmark papers in the development of bubble estimation via inversion of acoustic propagation. Because of their key importance to such estimates, a brief review of the different models available for describing the response of the bubbles will be presented.

Chapter 2 discusses two alternative models (complex sound speed and extinction cross section) upon which an inversion could be based and their results are shown to converge in the low void fraction, linear regime. One of these models is then used to describe the implementation of both the forward problem (prediction of the acoustic propagation characteristics through a known population) and the inverse problem (estimation of a bubble population from propagation characteristics measured within it). The assumptions inherent in the model are considered with specific reference to measurements made in the surf-zone and the need for a new nonlinear model is discussed.

Chapter 3 details the theoretical development of such a model. An attempt is made to describe a nonlinear complex sound speed and, while the linearisation of this expression yields the standard result, errors are shown to exist in the nonlinear regime. Discussion of the reasons for these errors results in development of an expression for the nonlinear extinction cross section. Comparison is made of standard theory and low and high amplitude nonlinear theory. Techniques for numerically implementing the new expression are discussed.

Chapter 4 describes the development of a system suitable for making measurements in the surf-zone. Consideration is given to the design of the acoustic signal used, and to the accurate measurement of acoustic propagation from that signal. In addition the development of a suitable sound source is described. Experimental setups are described for signal generation and acquisition and finally a complete system test is performed in the laboratory.

Chapter 5 documents the acquisition of sea trial data. Development of a rig suitable for deployment of apparatus in the harsh environment encountered in the surf-zone proved very challenging, and the evolution of such a rig is described. The experimental setup used, and the environmental conditions encountered, are documented and an initial review of the data is discussed.

Chapter 6 goes on to perform detailed analysis of the data collected during the sea trials. Comparison is made of results processed using standard linear theory and the new nonlinear theory. Chapter 7 summarizes the work, draws conclusions and provides recommendations for future work.

1.1 Inversion of acoustic propagation: a literature review of landmark papers

As discussed in the previous section, acoustical techniques have proven particularly successful at the estimation of bubble size distributions. This is partly owing to the efficiency of bubbles as acoustical scatters, which, when combined with theoretical models of the extent of this effect, allows estimation of bubbles numbers. An equally important factor, though, is the relation between a bubble's resonant frequency and its radius. It was Minnaert [10] who first calculated the relation,

$$\omega_0 = \frac{1}{R_0}\sqrt{\frac{3\gamma p_0}{\rho_w}} \tag{1.1}$$

where ω_0 is the bubble's angular resonance frequency, R_0 is the equilibrium radius of the bubble, γ is the ratio of specific heat at constant pressure to

that at constant volume. p_0 is the static pressure in the fluid outside the bubble wall and ρ_w is the density of the liquid surrounding the bubble. This equation, and others, will be discussed in more detail in section 1.2, which will review different models of bubble response. These two phenomena allow the number of bubbles to be estimated as a function of their radius. This estimate is the objective of the papers described in this section.

1.1.1 A review of the paper by Medwin, 1970 [11]

Medwin pioneered the estimation of bubble population via inversion of acoustic propagation. Previous investigators, for example Blanchard & Woodcock [12], had used optical methods of bubble estimation, a technique which suffers from a lack of discrimination between bubbles and suspended particulates, and in which it is difficult to establish a well-defined sampling volume.

Medwin used the concept of the extinction cross section (Ω_b^{ext}) of a bubble in order to estimate the number and size distribution of bubbles excited by an acoustic plane wave. The extinction cross section is the ratio of the time averaged power subtracted from a wave by the presence of a bubble to the intensity of that wave. It can be considered as the sum of two further cross sections, the scattering cross section Ω_b^{scat} and the absorption cross section Ω_b^{abs}:

$$\Omega_b^{ext} = \frac{\langle W \rangle}{I} = \Omega_b^{scat} + \Omega_b^{abs} \tag{1.2}$$

where $\langle W \rangle$ is time averaged power lost from an incident wave of intensity, I. Using this concept the change of intensity (due to bubbles) with distance x, of a plane wave propagating through a cloud of bubbles with a total extinction cross section per unit volume of Ω_c^{ext} is given by

$$\frac{\mathrm{d}I}{\mathrm{d}x} = I\Omega_c^{ext} \tag{1.3}$$

Integrating with respect to x gives

$$I = I_0 e^{\Omega_c^{ext} x} \tag{1.4}$$

where I_0 is the intensity at $x = 0$. The attenuation[1] per unit distance (caused by the presence of bubbles), A, is therefore given by

$$A = 10\log_{10}\left(\frac{I}{I_0}\right)/x = 10\Omega_c^{ext}\log_{10}e \approx 4.34\Omega_c^{ext} \tag{1.5}$$

Medwin used a form of the extinction cross section that assumes a bubble, driven by a plane wave, that oscillates linearly in a free field (derived from the work of Foldy [13, 14])

$$\Omega_b^{ext} = \frac{d_{tot}}{d_{rad}}\Omega_b^{scat} = \frac{d_{tot}}{d_{rad}}\frac{4\pi R_0^2}{((\omega_0/\omega)^2 - 1)^2 + (d_{tot}\omega_0^2/\omega^2)^2} \tag{1.6}$$

where ω is the angular excitation frequency, ω_0 is the bubble's angular resonant frequency, d_{tot} is the dimensionless total bubble damping constant and d_{rad} is the dimensionless radiation damping constant. In order to calculate the cross section presented by a spectrum of bubbles the cross section must be integrated across all radii.

$$\Omega_c^{ext} = \int_0^\infty \Omega_b^{ext} n(R_0) dR_0 \tag{1.7}$$

where $n(R_0)\ \mathrm{d}R_0$ represents the number of bubbles per m^3 between R_0 and $R_0 + \mathrm{d}R_0$. Medwin performs this integration by making a number of simplifying assumptions. These are: (1) that the damping is constant across all radii i.e. $d_{tot} = \delta_{tot}$, the damping constant at resonance; (2) that, within one radius increment, $\mathrm{d}R_0$, the bubble population is constant and equal to the number of resonant bubbles $n(R_0) = n(R_{res})$; and (3) that only resonant bubbles significantly contribute to the attenuation of propagating sound. These assumptions allow a closed form analytical solution to be calculated relating

[1] Attenuation is defined as 'the reduction in acoustic intensity of a sound field, where acoustic intensity is the average rate of flow of energy through a unit area normal the the direction of propagation' [67].

attenuation at a frequency, f, to the number of bubbles at the corresponding resonant bubble radii

$$A(f) = 4.34\Omega_c^{ext} = \frac{8.68\pi^2 R_0^3 n(R_{res})}{\delta_{rad}} \tag{1.8}$$

It is then trivial to invert this equation to find $n(R_{res})$. The key assumption (which was later criticised by Commander & McDonald, as described section 1.1.3) in Medwin's formulation is that in a distributed population of bubble radii, only resonant bubbles significantly contribute to the attenuation of propagating sound. At the time this assumption was justified by the observation that resonant bubbles have a scattering cross section that is several orders of magnitude greater than the corresponding geometric cross section (the cross sectional area presented by the a rigid sphere of equal radius to the bubble). While this observation was correct, it failed to take into account the fact that larger bubbles may present a geometric cross-section of greater magnitude than the scattering cross section. Figure 1.1 illustrates this by plotting the scattering cross section of a bubble excited at 100 kHz against the geometric cross section as a function of radius.

Medwin fielded the technique using an experimental system based upon transducer mounted approximately 0.76 m from a reflective plate. The transducer acted as both source and receiver and operated from 20-200 kHz. The attenuation was calculated by comparing the amplitudes of successive pulses. In order to distinguish between attenuation caused by the presence of bubbles and that caused by other effects, for example divergence and reflection losses, the system was calibrated in degassed water prior to deployment. The experimental work detailed was carried out in two locations, one in 60 feet of water, 1 mile offshore and another in 27 feet of water 300 yards offshore. Medwin's work estimated bubble numbers of approximately $1000/m^3$ in 1 μm bands for bubble radii $< 60\,\mu m$ in sea states one and two. Following this landmark paper the author published further papers [15, 16] describing measurements made employing the same theoretical techniques but making refinements to the experimental method and investigation of the affect of var-

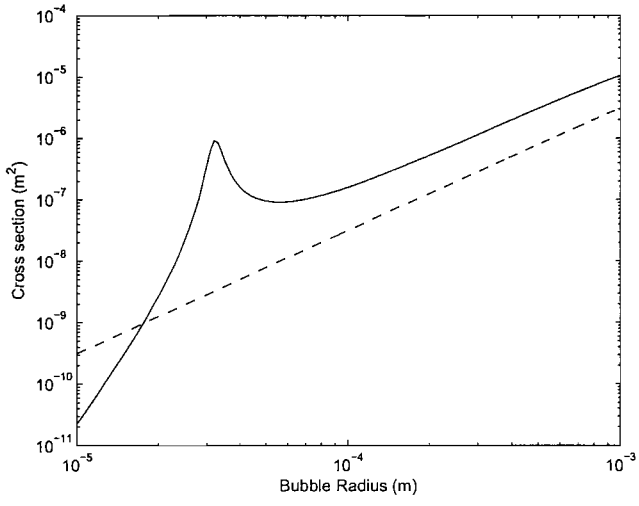

Figure 1.1: Scattering cross section (solid) of a bubble excited at 100 kHz plotted against the corresponding geometric cross section (dashed) as a function of bubble radius. Note that the two curves do not converge as the scattering cross section is related to the surface area of the bubble and not its cross sectional area.

ious oceanographic features. These papers showed that the original estimate of the population was an undercount and reported populations exceeding 10^5 bubbles per m^3 in a 1 μm radius bin.

1.1.2 A review of the paper by Commander & Moritz, 1989 [17]

This paper investigated discrepancies at small bubble radii ($< 50\,\mu m$) that had been noted between bubble size spectra that had been estimated acoustically (using Medwin's technique) and those estimated optically. Crucially, as described above, the acoustical techniques assumed that in a broad spectrum of bubble radii, only bubbles at resonance contribute to the scattering of a propagating sound wave. The flaw in this assumption can be shown by examination of figure 1.1. Medwin's observation that, at resonance, the scat-

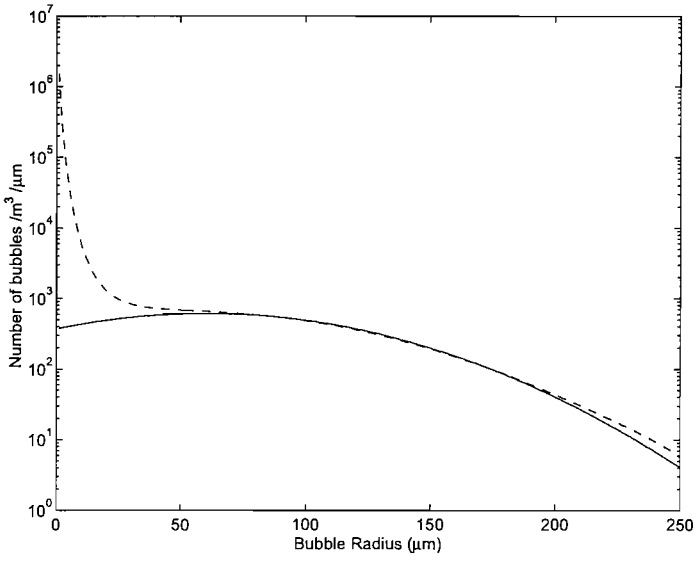

Figure 1.2: Commander & Mortiz's key result shows the original Gaussian population (solid line) and the result of Medwin's technique (dashed line) for estimating bubble numbers from an attenuation calculated using equation 1.5. The effect of the neglect of off-resonant scatters is shown as an error in the estimation of small bubble numbers.

tering cross section of a bubble is several orders of magnitude greater than its geometric cross section is correct. However, it fails to take into account the fact that larger bubbles may have a geometric cross section greater than the resonant cross section.

Commander & Moritz investigated the affect of this assumption by calculating the attenuation for a synthetic, Gaussian, bubble distribution. This attenuation was calculated including the effect of off-resonant scatterers. Then, using this attenuation as an input, they attempted to recover the original population by use of the relation shown in equation 1.8. Figure 1.2 shows the result, which exhibits a large error in the calculated numbers at small radii.

In conclusion Commander & Moritz proposed a corrected form of equation 1.7 that requires the extinction cross section of each bubble to be evaluated

at all bubble radii, hence removing Medwin's assumptions one and three.

$$\Omega_c^{ext}(f) = \int_0^\infty \Omega_b^{ext}(f, R_0) n(R_0) dR_0 \tag{1.9}$$

where $\Omega_c^{ext}(f)$ is the total extinction cross section presented by a cloud of bubbles and $\Omega_b^{ext}(f, R_0)$ is the extinction cross section of a single bubble of radius R_0, at driven at frequency f. This equation (a Fredholm integral of the first kind) is a significantly more challenging equation to solve than equation 1.7 and this is the subject of the final paper in this review.

1.1.3 A review of the paper by Commander & McDonald, 1991 [18]

Commander & McDonald [18] propose a finite-element method of estimating the bubble population that incorporates scattering from off-resonant bubbles. This was shown to be important in inverse methods of bubble determination by Commander & Moritz [17]. Equation 1.9 describes the total extinction cross section of a cloud of bubbles and incorporates off-resonant scattering. In order to solve this equation the bubble distribution is approximated using linear splines as shown in equation 1.10

$$n(R_0) = \sum_{h=1}^{H} n_h B_h(R_0) \tag{1.10}$$

where B_h represents a linear B-spline[2] and n_h the value of n at the h^{th} radius value. Substituting 1.10 into 1.9 presents the following system of equations.

$$\Omega_c^{ext}(f_g) = \sum_{h=1}^{H} K_{gh} n_h \tag{1.11}$$

where the elements in the matrix K_{gh} are given by

[2]The linear b-spline linearly interpolates across a radius bin and is zero for all values outside that bin.

$$K_{gh} = \int_{R_{0_{min}}}^{R_{0_{max}}} \Omega_b^{ext}(f_g, R_0) B_h dR_0 \tag{1.12}$$

Equation 1.12 is a particularly useful result since it describes the total behaviour of a bubble cloud. It is also flexible in that the 'kernel' function, K_{gh}, can be changed from the extinction cross section to some other model of bubble response.

As discussed in section 1.1.2 the extinction cross section of a bubble only contains a *local* maximum at resonance and the scattering from geometrical scattering above resonance can be significantly greater. This renders the inverse solution of equation 1.12 '*ill-conditioned*', meaning that small changes in the input vector, Ω_c^{ext}, can cause very large changes in the output, n. In order to obtain a meaningful answer from this inversion, a method of stabilizing this solution must be employed. This process is referred to as *regularisation*. There are many different regularisation techniques which may be employed and Commander & McDonald [18] recommend a method of regularisation imposing a 'smoothness' constraint upon the solution. Commander & McDonald demonstrate their technique by recreating series of synthetic distributions from their calculated attenuation. However no experimental data is presented to validate the work.

Subsequent authors have proposed minor refinements and have experimentally verified the technique. Duraiswami *et al.* [19] outlines a method that uses phase speed as well as attenuation as the input to the system of equations. They find similar results to those achieved using optical estimates on a laboratory bubble cloud generated using electrolysis. Terrill and Melville [20] detail an experimental technique using broadband signals rather than the more usual pulse train of narrowband pulses. Experimental results are reported, firstly from a 50 metre wave channel and secondly from a site approximately 150m away from the surf-zone at Scripps pier in California.

The formulation proposed by Commander & McDonald represents the current 'state-of-the-art' in the estimation of bubble populations via inversion of acoustic propagation. Despite a significant amount of following work no

fundamental advance in the underlying theory has been proposed and the benefits of some of the refinements made are still to be proven.

1.2 Models of bubble dynamics: a literature review of landmark papers

The modelling of bubble oscillations is a formidable task that has been the subject of very many papers over 70 years or more. As such this section will not attempt to derive the different models from first principles but will provide an insight into the underlying physics of the models employed later in this work and the assumptions made within each of those. For a more detailed treatment of the subject a number of authoritative texts are available [5, 21].

1.2.1 A review of the paper by Minneart, 1933 [10]

The simplest 'model' of bubble dynamics was developed by Minnaert [10] and related a bubble's resonant frequency to its equilibrium radius. Minnaert's formulation assumed a spherical gas bubble in a liquid undergoing low amplitude simple harmonic motion. The gas inside the bubble is assumed to behave adiabatically and the product of the wave number ($k = \omega/c_w$, where c_w is the ambient sound speed in the bubble-free liquid), and the equilibrium bubble radius is assumed to be much less than one ($kR_0 \ll 1$). Such an assumption is common in many models of bubble dynamics and is made throughout this study. Minnaert equates the maximum kinetic energy in the liquid to the maximum potential energy within the gas (neglecting damping due to surface tension and viscosity). This yields the result

$$\omega_0 = \frac{1}{R_0}\sqrt{\frac{3\gamma p_0}{\rho_w}} \tag{1.13}$$

In the case of air bubbles in water at one atmosphere hydrostatic pressure equation 1.13 can be approximated by

$$2\pi\omega_0 R_0 \approx 3Hz.m \tag{1.14}$$

However such approximations are undesirable when attempting to determine an accurate bubble size distribution. Minnaert's formulation for bubble resonant frequency can be adjusted to include heat conduction by assuming that the heat transfer is neither adiabatic nor isothermal but, as will really be the case, some intermediate rate of transfer. This is achieved by substitution of a polytropic index κ (which can vary from unity, the isothermal case, to γ, the adiabatic case) into equation 1.13.

$$\omega_0 = \frac{1}{R_0}\sqrt{\frac{3\kappa p_0}{\rho_w}} \tag{1.15}$$

Leighton [5]§4.4.2 cites the following expression for κ

$$\kappa = \gamma(1+\delta_{th}^2)^{-1}\left[1+\frac{3(\gamma-1)}{R_0/l_D}\left(\frac{\sinh(R_0/l_D)-\sin(R_0/l_D)}{\cosh(R_0/l_D)-\cos(R_0/l_D)}\right)\right]^{-1} \tag{1.16}$$

where $l_D = \sqrt{D_g/2\omega}$ represents the thickness of the thermal boundary layer (D_g is the thermal diffusivity of the gas within the bubble) and δ_{th} is the thermal damping constant and is discussed in more detail in section 1.2.4. Equation 1.15 neglects terms due to surface tension, viscosity and the vapour pressure within the bubble. Adding these terms gives ([5] §4.2.1(c))

$$\omega_0 = \frac{1}{R_0\sqrt{\rho_w}}\sqrt{3\kappa\left(p_0+\frac{2\sigma}{R_0}-p_v\right)-\frac{2\sigma}{R_0}+p_v-\frac{4\mu^2}{\rho_w R_0^2}} \tag{1.17}$$

where σ is the surface tension co-efficient, p_v is the vapour pressure within the bubble and μ the shear viscosity co-efficient. Throughout this work this equation is used to calculate bubble resonant frequencies.

1.2.2 A review of the paper by Commander & Prosperetti, 1989 [22]

Commander & Prosperetti's paper derives an expression for the effective complex wavenumber of a plane wave propagating through a bubbly liquid. This quantity can be related to the phase speed of the wave as well as the attenuation experienced by it. This, in a similar fashion to the extinction cross section described above, makes it a suitable model for use in inverse methods of bubble estimation. As a result the paper has been cited in excess of 100 times since publication. The expression for the complex wavenumber is derived by making a first order approximation (hence linearising the expression) to the Herring-Keller equation (see section 1.2.3). A more intuitive derivation is based upon the concept of the compressibility of a cloud of bubbles, K_c, and its reciprocal, the bulk modulus, B_c, given by

$$K_c = \frac{1}{B_c} = -\frac{1}{V_c}\frac{\mathrm{d}V_c}{\mathrm{d}P_{tot}} = \frac{1}{\rho_c c_c^2} \tag{1.18}$$

where V_c is the volume of a cloud of bubbles and P_{tot} is the total pressure (i.e. the ambient pressure plus the acoustic pressure). Consider a medium containing n identical bubbles per unit volume. The compressibility of the bubbly medium K_c is equal to the sum of the compressibility of the bubble-free liquid, K_w, and all the gas forming the bubbles within it K_{bub} (which is complex).

$$K_c = K_w + K_{bub} \tag{1.19}$$

The wavenumber of a plane wave propagating through the bubbly liquid, k_c (which can be thought of as a *spatial* frequency [24]) is given by

$$k_c = \frac{2\pi}{\lambda} = \frac{\omega}{c_c} = \omega\sqrt{\rho_c K_c} \tag{1.20}$$

where λ is the wavelength of the plane wave and c_c is the sound speed in the bubbly liquid. Substitution of 1.19 into 1.20 and the approximation that the

density of the cloud is approximately equal to the density of the bubble-free liquid yields

$$k_c = \sqrt{\frac{\omega^2}{c_w^2} - \rho_w \omega^2 K_{bub}} \tag{1.21}$$

Each bubble has a volume, V, which will change in time in response to an applied pressure. If we assume that there are N_{tot} bubbles in the cloud all with the same radius then, when the whole population experiences such a change the compressibility of all the bubbles in the medium, K_{bub}, is given by

$$K_{bub} = -N_{\text{tot}} \frac{\Delta V}{\Delta P} \tag{1.22}$$

where P is the applied acoustic pressure, in this case proportional to a simple harmonic plane wave varying with time, $P = P_A e^{j\omega t}$. By assuming that the bubble responds with small amplitude linear oscillations away from equilibrium and remains spherical at all times, the volume of the bubble may be approximate to first order as

$$V = \frac{4}{3}\pi R^3 = \frac{4}{3}\pi R_0^3 \left(1 + \frac{R_\epsilon}{R_0}\right)^3 \approx \frac{4}{3}\pi R_0^3 \left(1 + 3\frac{R_\epsilon}{R_0}\right) \tag{1.23}$$

where R_ϵ is the amplitude of the oscillations away from equilibrium. Noting that $\Delta V = 4\pi R_0^2 R_\epsilon$ some simple algebra (combining equations 1.21, 1.22 and 1.23) yields

$$k_c = \sqrt{\frac{\omega^2}{c_w^2} - 4\pi\omega^2 \frac{\rho_w R_\epsilon R_0^2 N_{\text{tot}}}{\Delta P}} \tag{1.24}$$

The value of R_ϵ may be derived by modelling the bubble as a forced, damped linear oscillator. The equation of motion is given (in the radius-force frame[3]) by

[3] for discussion of the different frames of reference that may be used in models of bubble response see [5] §3.2.1.

$$m_{RF}^{rad}\ddot{R}_\epsilon + b_{RF}^{tot}\dot{R}_\epsilon + k_{RF}R_\epsilon = F_0 e^{j\omega t} \tag{1.25}$$

where the 'mass' of the bubble m_{RF}^{rad} comes from the surrounding liquid into which the bubble radiates (see [5] §2.3.1(c)), the resistive term leading to damping is given by b_{RF}^{tot} and the stiffness of the bubble is given by k_{RF}. Implicit in this equation are several key assumptions:

1. that the bubble remains spherical at all times.
2. that the bubble's radius is much smaller than the wavelength of the exciting force.
3. that the bubble exists in an infinite medium.
4. that the bubble radiates into a free field.
5. that the bubble is driven at small-amplitude by a monochromatic plane wave.

Equation 1.25 is solved by setting $\omega_0 = \sqrt{k_{RF}/m_{RF}^{rad}}$ and $b_{RF}^{tot} = 2m_{RF}^{rad}\beta_{tot}$ before dividing by m_{RF}^{rad}. If the steady-state response ($t \to \infty$) of the bubble is considered (thus taking the particular integral and neglecting the complementary function) and it is assumed that $R_\epsilon \propto e^{j\omega t}$, then the following result is yielded

$$(\omega_0^2 - \omega^2 + j2\beta_{tot}\omega)R_\epsilon = \frac{F_0}{m_{RF}^{rad}}e^{j\omega t} \tag{1.26}$$

Equating the force experienced across the bubble wall to the amplitude of the driving sound field ($F_0 = -P_A 4\pi R_0^2$, where the minus sign indicates that an increase in pressure causes a decrease in radius) and the 'mass' of the bubble to the mass of the displaced liquid ($m_{RF}^{rad} = \rho_w 4\pi R_0^3$) allows the following expression of R_ϵ to be derived

$$R_\epsilon = -\frac{P_A e^{j\omega t}}{\rho_w R_0}\frac{1}{\omega_0^2 - \omega^2 + j2\beta_{tot}\omega} \tag{1.27}$$

This result is the same as that derived in [5] (equation 4.43). Substituting 1.27 into 1.24 and noting that $\Delta P = P_A e^{j\omega t}$, yields

$$k_c = \sqrt{\frac{\omega^2}{c_w^2} - 4\pi\omega^2 \frac{R_0 N_{tot}}{\omega_0^2 - \omega^2 + j2\beta_{tot}\omega}} \tag{1.28}$$

If a distributed population of bubble radii exists and n now represents the number of bubbles with radius between R_0 and $R_0 + dR_0$, equation 1.28 may be re-expressed as an integral across all radii

$$k_c = \sqrt{\frac{\omega^2}{c_w^2} + 4\pi\omega^2 \int_0^\infty \frac{R_0 n(R_0)}{\omega_0^2 - \omega^2 + j2\beta_{tot}\omega} dR_0} \tag{1.29}$$

This is the expression for the complex wavenumber derived by Commander & Prosperetti. However, several restrictive assumptions have been during its derivation, for instance small-amplitude oscillations. Subsequent investigators have attempted to derive models without recourse to such assumptions.

1.2.3 A discussion of nonlinear models

Many investigators have attempted to derive nonlinear models of bubble oscillations in order to describe more fully the motion of bubbles, especially when driven to large-oscillations. While such models are not directly the subject of this work they can be useful as the basis for estimating the bubble's affect on acoustic propagation. As such, two of the most commonly used models will be briefly reviewed here.

The first of the two models employs the Rayleigh-Plesset equation, so called because the form of the equation has been formulated by a number of contributors [25–28] who have expanded upon the original work of Rayleigh [29]. The equation assumes a spherically symmetric bubble initially at rest in an incompressible liquid. When the bubble is excited by a pressure $P(t)$ it will change its radius to a new value, R. During this change of radius the liquid surrounding the bubble will acquire kinetic energy. If this energy is

equated to the work done by the bubble as it expands the follow equation is derived (Leighton [5] §4.2.1(a))

$$\int_{R_0}^{R}(p_L - p_\infty)4\pi R^2 \mathrm{d}R = 2\pi R^3 \dot{R}^2 \rho_w \tag{1.30}$$

where p_L represents the pressure in the liquid outside the bubble wall, p_∞ is the pressure remote from the bubble and the dot represents the first derivative with respect to time. Differentiation of equation 1.30 yields

$$\frac{p_L - p_\infty}{\rho_w} = \frac{3\dot{R}^2}{2} + R\ddot{R} \tag{1.31}$$

By substituting an expression for p_L derived from equality of pressure across the bubble wall (assuming polytropic behaviour of the gas and a quasi-static expansion i.e. spatially uniform conditions exist within the bubble) and setting $p_\infty = p_0 + P(t)$ an initial form of the Rayleigh-Plesset equation is yielded

$$\frac{3\dot{R}^2}{2} + R\ddot{R} = \frac{1}{\rho_w}\left(\left(p_0 + \frac{2\sigma}{R} - p_v\right)\left(\frac{R_0}{R}\right)^{3\kappa} + p_v - \frac{2\sigma}{R} - p_0 - P(t)\right) \tag{1.32}$$

where σ is the surface tension of the liquid and p_v is the vapour pressure inside the liquid. A viscous term (see [5] §4.2.1(b)) may be added [28] to equation 1.32 by consideration of the rates of strain within the bubble wall. This yields the most commonly used form of the Rayleigh-Plesset equation

$$\frac{3\dot{R}^2}{2} + R\ddot{R} = \frac{1}{\rho_w}\left(\left(p_0 + \frac{2\sigma}{R} - p_v\right)\left(\frac{R_0}{R}\right)^{3\kappa} + p_v - \frac{2\sigma}{R} - \frac{4\eta\dot{R}}{R} - p_0 - P(t)\right) \tag{1.33}$$

While assumptions similar to those made in the expression derived by Commander & Prosperetti[4] no assumption of linearity has been made. How-

[4]i.e. that the bubble remains spherical; is small in comparison to the wavelength of the driving field; that it exists in an infinite medium; that it radiates into a free field and that it is driven by a plane wave.

ever the Rayleigh-Plesset equation does make the restrictive assumption of liquid incompressibility. This precludes the inclusion of damping due to the re-radiation of sound by the bubble into the medium. Also, while the treatment of the gas as polytropic simulates heat flow during the expansion and contraction cycle, it does not allow for any net loss of energy due to thermal damping. Thus, two of the three main damping mechanisms in the system are neglected in the Rayleigh-Plesset equation. In order to address this shortcoming subsequent investigators [30,31] have attempted to derive an equation of motion that treats the surrounding liquid as compressible. However, the most commonly used equation (which assumes a time-invariant finite sound speed in the liquid) is the Herring-Keller equation [32,33] given by

$$\frac{3\dot{R}^2}{2}\left(1-\frac{\dot{R}}{3c_w}\right)+R\ddot{R}\left(1-\frac{\dot{R}}{c_w}\right)= \left(1+\frac{\dot{R}}{c_w}\right)\frac{1}{\rho_w}\left(p_L-p_0-P\left(t+\frac{R}{c_w}\right)\right)+\frac{R}{\rho_w c_w}\frac{\mathrm{d}p_L}{\mathrm{d}t} \qquad (1.34)$$

In equation 1.34 the final term allows the storage of energy in the medium surrounding the bubble. In the limit $c_w \rightarrow \infty$ equation 1.34 reduces to equation 1.33. Crucial to the evaluation of equation 1.34 is p_L, the pressure in the liquid surrounding the bubble. This is typically obtained from the behaviour of the gas, and hence the internal pressure, p_i, within the bubble. This can be calculated by applying the perfect gas law to the spatially averaged pressure within the bubble [34–36]. Such a solution is non-trivial and typically requires numerical techniques for solution[5]. Equation 1.34 is used throughout this work (see especially chapter 3) to model the nonlinear behaviour of bubbles.

[5]MATLAB^{TM} code for solving equation 1.34 was provided by Mr. H. A. Dumbrell of the Defence Science and Technology Laboratory. This code enables the radius-time history of a bubble to be determined for an arbitrary pulse. The author gratefully acknowledges use of this code.

1.2.4 A discussion of linear damping constants

A number of different conventions for representing bubble damping are used in different models, and, in some cases, different investigators use different terms for the same model. As such, some clarification and discussion of the different terms may be beneficial. Total damping is the expression used to describe all the energy lost from the bubble by various different mechanisms. There are three primary means by which energy is lost from the bubble: viscous damping, where work is done against the viscosity of the surrounding fluid; thermal damping, where thermal conduction across the bubble wall takes place and radiation damping where energy is lost as the bubble radiates acoustically. Other damping mechanisms may exist although these three are usually considered to dominate.

Total damping (in the radius-force frame [5] §3.2.1(a)) is expressed in equation 1.25 by the co-efficient b_{RF}^{tot}. This equation can be made independent of the frame of reference by dividing by the radiation mass of the bubble expressed in that same frame of reference. This yields β_{tot}, an equivalent damping constant, with units of time^{-1}, that is independent of the frame of reference:

$$\beta_{tot} = \frac{b_{RF}^{tot}}{2m_{RF}^{rad}} \tag{1.35}$$

By dividing the bubble's frame-dependent radiation damping by its stiffness, the damping of the bubble can represented as a dimensionless damping constant

$$d_{tot} = \frac{\omega b_{RF}^{tot}}{k_{RF}} = \frac{2\omega\beta_{tot}}{\omega_0^2} \tag{1.36}$$

Expressions for these dimensionless damping constants are given by Eller [37] as

$$d_{th} = \frac{3(\gamma-1)(\varphi(\sinh\varphi+\sin\varphi)-2(\cosh\varphi-\cos\varphi))}{\varphi^2(\cosh\varphi-\cos\varphi)+3(\gamma-1)\varphi(\sinh\varphi+\sin\varphi)} \tag{1.37}$$

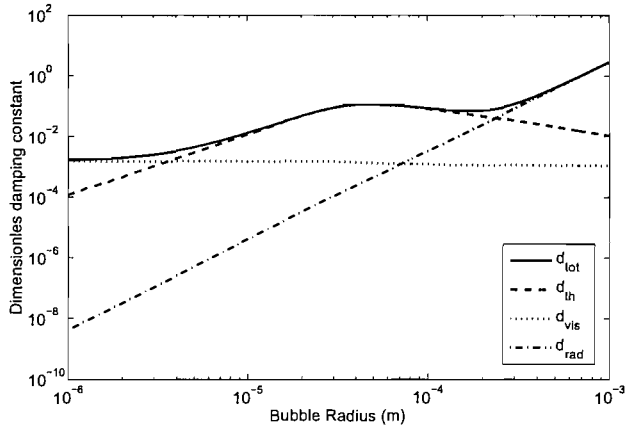

Figure 1.3: Dimensionless damping constants calculated using Eller's [37] expressions (equations 1.37 to 1.39) for a range of bubble radii driven at 20 kHz. As can be seen the total damping (solid) experienced by the bubble is a sum of three damping mechanisms: thermal (dashed), viscous (dotted) and radiation (dash-dot). Different mechanisms dominate in different parts of the bubble size spectrum.

where φ represents the ratio of bubble radius to the thickness of the thermal boundary layer in the bubble, $R_0/l_D = R_0/\sqrt{D_g/2\omega}$, and D_g is the thermal diffusivity of the gas contained in the bubble.

$$d_{rad} = \frac{\rho_w}{3\kappa p_0}\frac{(R_0\omega)^3}{c_w} \tag{1.38}$$

$$d_{vis} = \frac{4\eta\omega}{3\kappa p_0} \tag{1.39}$$

where κ is the polytropic index of the gas contained within the bubble, p_0 is the hydrostatic pressure in the liquid outside the bubble and η is the shear viscosity of that liquid. Figure 1.3 shows Eller's damping constants for a range of bubble radii driven by a fixed frequency of 20 kHz. As can be seen in the figure, different damping mechanisms dominate at different bubble radii, and hence all three of these primary mechanisms should be evaluated in order to ensure that the system is fully described. A final special case is δ_{tot}

which corresponds to the total dimensionless damping constant evaluated *at resonance*. Incorporation of damping into nonlinear models is less straightforward and the interested reader is referred to Propseretti *et al.* [35].

1.3 Summary

This chapter has sought to introduce the reader to some of the theoretical concepts, techniques and equations that will be used later in this work. As such it has performed reviews of key papers in the fields of inversion estimation of bubble estimation and different methods of modelling the behaviour of bubbles. The appreciation gained in this chapter lays down the basis for the development of a system for estimating bubble populations in the surf-zone. The next chapter will discuss the development of a theoretical framework for such a system.

Chapter 2

Theoretical development of an inverse technique for estimating bubble populations

The estimation of bubble population by inversion of acoustic propagation has been the subject of study and research for over thirty years (see section 1.1). However the principles and techniques which must be applied in order to obtain a meaningful answer are demanding, and there is a danger of not fully considering all the implications of the different assumptions that must be made. This chapter aims to develop a theoretical framework upon which to base a system for estimating bubble populations. Initially this will use the current state-of-the-art methods but will seek to explore and expand the regions where benefit might be found from a more rigorous approach. The eventual aim is a system suitable for measuring oceanic bubble populations, especially those within the surf-zone. The system will be rigorously designed taking into account all the assumptions and considerations necessary for an accurate assessment of the bubble population. While the theory and techniques are developed with oceanic populations in mind, the principles could easily be translated into equivalent fields providing that the same rigour is applied to the consideration of any assumptions made.

2.1 The forward problem

Solving the forward problem (i.e. predicting the propagation characteristics of a acoustic wave traveling in a known bubble population) is considerably more straight-forward than the inverse problem, and hence will be studied first. The ability to solve the forward problem will be vital in many elements of the system design and will also provide a useful method of checking the accuracy of any results obtained (the population predicted by the inversion should, providing the estimate is accurate, allow reconstruction of the original measured propagation characteristics).

The general form of the problem to be solved is

$$\int_{\Omega} system(\Lambda, \Omega) \times input \, d\Omega = output \tag{2.1}$$

The forward problem predicts the output of a system using a mathematical description of it combined with a known input. The inverse problem focuses on determination of either the input *or* the system given the output. The ability to estimate the system function is one which can be overlooked and there may be applications in the study of bubbles where this would be a useful technique. An example of this might be the validation of bubble models, but this is outside the scope of this study and will not be considered further.

When applying equation 2.1 to the problem under consideration, the system is some model of bubble response, the input represents the bubble population being measured, and the output is the propagation characteristics. The crux of the technique is to relate bubble population to a physically measurable parameter. The mathematical model used to formulate the system is important to the accurate solution of either the forward or the inverse problems. If the model is inaccurate, or if any of its inherent assumptions are compromised, then the reliability of any results will be questionable. Hence an important aspect of any solution to either the forward or the inverse problem is accurate modelling.

For the initial stage of this study the model used will assume linear, steady-state oscillation of a bubble in a free field, being driven by a plane wave. The validity of these assumptions will be examined later in the chapter. Review of the open source literature [18 20.38 43.72] has shown that this 'class' of model is used in all the current state-of-the-art bubble estimation systems that employ inversion of acoustic propagation. The two models that will be considered here concern the complex sound speed in the bubbly liquid and the bubble's extinction cross section (see section 1.1.1).

2.1.1 The linear complex sound speed

The most commonly cited linear formulation of the complex wavenumber is that given by Commander & Prosperetti [22] (see section 1.2.2).

$$k_c = \sqrt{\frac{\omega^2}{c_w^2} + 4\pi\omega^2 \int_0^\infty \frac{R_0 n(R_0)}{\omega_0^2 - \omega^2 + \mathrm{j}2\beta_{tot}\omega} \mathrm{d}R_0} \tag{2.2}$$

The ratio of the speed of sound in pure water, c_w, to that in the bubbly water, c_c, is therefore given by

$$\frac{c_w}{c_c} = \sqrt{1 + 4\pi c_w^2 \int_0^\infty \frac{R_0 n(R_0)}{\omega_0^2 - \omega^2 + \mathrm{j}2\beta_{tot}\omega} \mathrm{d}R_0} \tag{2.3}$$

Commander & Prosperetti present an alternative set of expressions for the frame-independent damping constant derived from the work of Prosperetti *et al.* [35].

$$\beta_{tot} = \beta_{vis} + \beta_{th} + \beta_{rad} = \frac{2\eta}{\rho_w R_0^2} + \frac{p_0}{2\rho_w \omega R_0^2} \Im(\Phi) + \frac{\omega^2 R_0}{2c_w} \tag{2.4}$$

where $\Im(\Phi)$ represents the imaginary component of Φ, given by

$$\Phi = \frac{3\gamma}{1 - 3(\gamma - 1)\mathrm{j}\chi((\mathrm{j}/\chi)^{(1/2)}(\mathrm{j}/\chi)^{(1/2)} \coth(\mathrm{j}/\chi)^{(1/2)} - 1)} \tag{2.5}$$

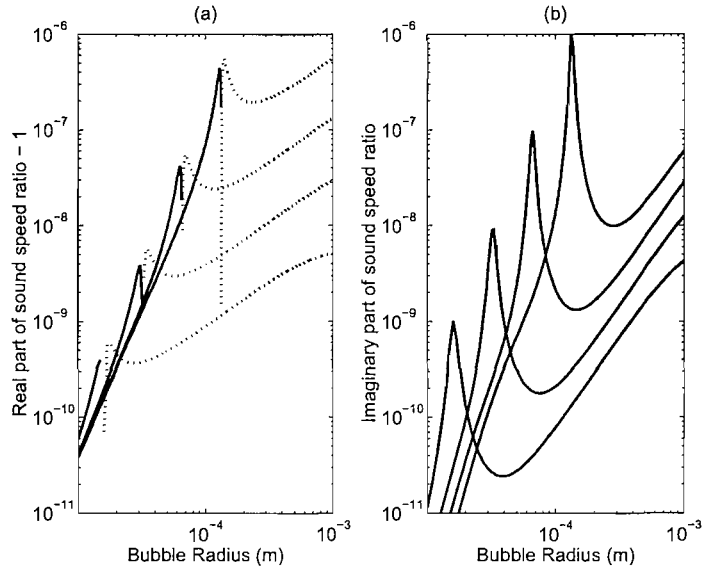

Figure 2.1: Real and imaginary parts of the complex ratio of sound speeds (equation 2.3) plotted as a function of bubble radius at four different frequencies. In both cases the frequency curves are (from left to right) 200, 100, 50 & 25 kHz (a) Real part of sound speed ratio minus one ($\Re\left(\frac{c_w}{c_c}\right) - 1$) (to enable logarithmic plotting the negative portion of this graph is shown dashed). This quantity is related to the phase speed variation in the medium (see equations 2.10 and 2.12). (b) Imaginary part ($\Im\left(\frac{c_w}{c_c}\right)$). This quantity is related to the attenuation in the medium (equation 2.13).

where

$$\chi = \frac{D_g}{\omega R_0^2} \tag{2.6}$$

Figure 2.1 shows plots of the real and imaginary parts of the complex ratio of sound speeds (equation 2.3) for a range of bubble radii (assuming a uniform distribution) insonified at four different frequencies. As can be seen the real part, which is related to the phase speed in the medium (as described by equations equations 2.10 and 2.12), goes from negative to positive at the bubble resonance. The imaginary part, which is related to the attenuation (equation 2.13), goes through a peak at resonance and then increases in

value as geometrical scattering becomes dominant (provided $kR_0 \ll 1$). If it is assumed that $n(R_0)$ is sufficiently small that the fractional term in equation 2.3 is less than one (a valid assumption at low void fractions. for further discussion see section 2.3.2) the square root can be expanded using a binomial expansion:

$$(1+\zeta)^e = 1 + e\zeta + \frac{e(e-1)}{2!}\zeta^2 + \frac{e(e-1)(e-2)}{3!}\zeta^3 + \ldots \quad \text{for } |\zeta| < 1 \quad (2.7)$$

This yields the following expression

$$\frac{c_w}{c_c} = 1 + 2\pi c_w^2 \int_0^\infty \frac{R_0 n(R_0)}{\omega_0^2 - \omega^2 + \mathrm{j}2\beta_{tot}\omega} \mathrm{d}R_0 \quad (2.8)$$

In order to simplify the expression. equation 2.8 can be re-expressed as the deviation of the complex sound speed from ambient sound speed in the liquid

$$\frac{c_w}{c_c} - 1 = 2\pi c_w^2 \int_0^\infty \frac{R_0 n(R_0)}{\omega_0^2 - \omega^2 + \mathrm{j}2\beta_{tot}\omega} \mathrm{d}R_0 \quad (2.9)$$

Equation 2.9 linearly relates the variation in complex sound speed in the bubbly medium to the number of bubbles in that medium. If equation 2.9 is split into real and imaginary parts it can be shown that they correspond to the phase speed and attenuation respectively. This can be shown as follows:

$$\frac{c_w}{c_c} - 1 = u - \mathrm{j}v \quad (2.10)$$

It is assumed that a plane wave is traveling through the medium in a positive direction, with time, t and distance, x. This can be expressed as

$$\exp\left(\mathrm{j}(\omega t - k_c x)\right) = \exp\left(-\frac{\omega v}{c_w}x\right) \exp\left(\mathrm{j}\omega\left(t - \frac{u}{c_w}x\right)\right) \quad (2.11)$$

From this it can be seen that the phase speed c_{ph} of the sound wave is given by

$$c_{ph} = \frac{c_w}{u} \tag{2.12}$$

and that the attenuation coefficient, A (in dB/m) is given by

$$A = 20 \left(\frac{\omega v}{c_w} \right) log_{10}(e) \tag{2.13}$$

Equations 2.12 and 2.13 show the relation between the complex sound speed in the bubbly medium and physical parameters that are more easily measured. Since the complex sound speed is dependent upon the bubble size distribution, then measurement of such parameters may form the basis of an inverse technique for estimation of the bubble size distribution.

2.1.2 The linear extinction cross section

An alternative model that could be used to relate bubble numbers to a measurable acoustic property is the extinction cross section. This was used in the pioneering works of Medwin (section 1.1.1) and Commander & McDonald (section 1.1.3). Leighton [5] (equation 4.27) shows that the extinction cross section of bubble when driven into small amplitude linear pulsations by a plane wave is given by

$$\Omega_b^{ext} = \frac{d_{tot}}{d_{rad}} \Omega_b^{scat} = \frac{d_{tot}}{d_{rad}} \frac{4\pi R_0^2}{((\omega_0/\omega)^2 - 1)^2 + (d_{tot}\omega_0^2/\omega^2)^2} \tag{2.14}$$

where Ω_{scat} is the scattering cross section of the bubble (the ratio of the sound re-radiated by the bubble to the incident intensity) and d_{tot} and d_{rad} are the bubble's total and radiation dimensionless damping constants respectively.

Calculation of the appropriate damping terms in equation 2.14 yields the linear extinction cross section of a bubble. Figure 2.2 shows the calculated extinction cross section for a range of bubble radii driven at 25, 50 100 and 200 kHz. The extinction cross section is related to attenuation as discussed in sections 1.1.1 and 1.1.2. A plot of the extinction cross-section (figure

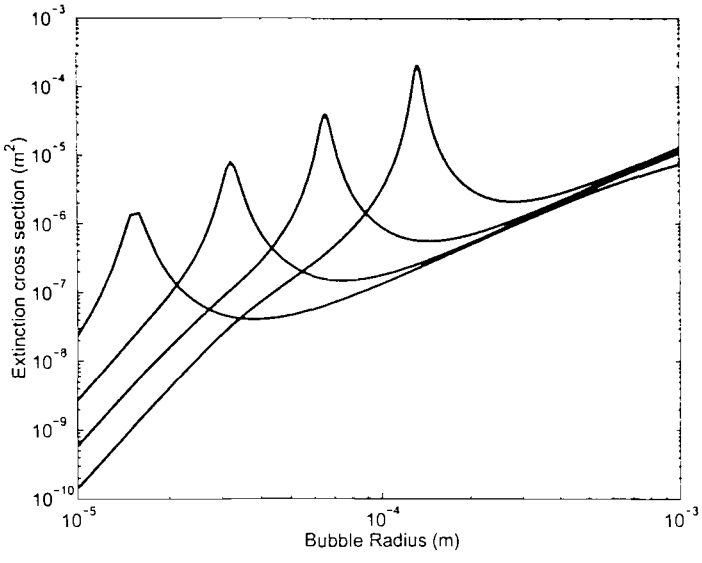

Figure 2.2: The linear extinction cross section calculated using equation 2.14 for a range of bubble radii driven at 25, 50, 100 & 200 kHz from left to right on the graph.

2.2) at a number of fixed frequencies as a function of bubble radius shows qualitative similarities to the imaginary part of the extinction cross-section (figure 2.1(b)), for example the position of the peaks.

These two sections have shown three different methods of obtaining the attenuation of a plane wave propagating in a bubbly medium: (1) determination of the ratio of sound speeds in the medium (equation 2.3); (2) the binomial approximation to the ratio of sound speeds in the medium (equation 2.9); and (3) determination of the bubble extinction cross section (equation 2.14). The following sections will solve the forward problem using each of these methods, first using synthetic data and then for real oceanic data as collected by previous investigators.

2.1.3 Numerical evaluation of integral equations

The numerical evaluation of equations 2.3, 2.9 and 2.14 requires that the bubble population is expressed as a discrete series of radius 'bins', i.e. the number of bubbles per unit volume between radius R_0 and $R_0 + \mathrm{d}R_0$. This leads to the following matrix formulation (bold symbols denote matrix or vector quantities)

$$\boldsymbol{\alpha} = \boldsymbol{K}\boldsymbol{n} \tag{2.15}$$

where $\boldsymbol{\alpha}$, a column vector, represents the acoustic propagation characteristics (either the complex ratio of sound speeds or extinction cross section, as appropriate); $\boldsymbol{K}$, a matrix, represents the response of the bubbles as described by either equation 2.3, 2.9 or 2.14; and $\boldsymbol{n}$ is a column vector representing the number of bubbles per cubic metre within each radius bin. In matrix notation equation 2.15 can be expressed as

$$\begin{pmatrix} \alpha(\omega_1) \\ \alpha(\omega_2) \\ \alpha(\omega_3) \\ \vdots \\ \alpha(\omega_G) \end{pmatrix} = \begin{pmatrix} K(\omega_1, R_{0_1}) & K(\omega_1, R_{0_2}) & \dots & K(\omega_1, R_{0_H}) \\ K(\omega_2, R_{0_1}) & K(\omega_2, R_{0_2}) & \dots & K(\omega_2, R_{0_H}) \\ K(\omega_3, R_{0_1}) & K(\omega_3, R_{0_2}) & \dots & K(\omega_3, R_{0_H}) \\ \vdots & \vdots & \ddots & \vdots \\ K(\omega_G, R_{0_1}) & K(\omega_G, R_{0_2}) & \dots & K(\omega_G, R_{0_H}) \end{pmatrix} \begin{pmatrix} n(R_{0_1}) \\ n(R_{0_2}) \\ n(R_{0_3}) \\ \vdots \\ n(R_{0_H}) \end{pmatrix} \tag{2.16}$$

While G does not necessarily equal H, it is normal for the selected frequencies to correspond to the resonant radii of each bubble radius bin hence $\boldsymbol{K}$ is typically square. The individual elements of the matrix in equation 2.16 represent the summation of the affect on the propagation of all the bubble radii within a particular radius bin. The value of each element depends upon the model used. If the full complex sound speed (equation 2.3) is used the matrix values are given by

$$K_{g,h} = \int_0^\infty \frac{c_w}{c_c} B_h \mathrm{d}R_0 \tag{2.17}$$

(where B_h represents a linear B-spline see section 1.1.3) and the $\boldsymbol{\alpha}$ values are given by

$$\alpha_g = \frac{c_w}{c_{ph}} + \mathrm{j}\frac{c_w}{\omega}\frac{A}{20\log_{10}(e)} \tag{2.18}$$

If the binomially expanded complex sound speed (equation 2.9) is used the $\boldsymbol{\alpha}$ values are given by equation 2.18 and the matrix values are given by

$$K_{g,h} = \int_0^\infty \frac{c_w}{c_{bin}} B_h \mathrm{d}R_0 \tag{2.19}$$

where c_{bin} represents the binomial expansion of the complex sound speed. The matrix values when using the extinction cross section (equation 2.14) are

$$K_{g,h} = \int_0^\infty \Omega_b^{ext} B_h \mathrm{d}R_0 \tag{2.20}$$

and the $\boldsymbol{\alpha}$ values are

$$\alpha_g = \frac{A}{10\log_{10}\mathrm{e}} \tag{2.21}$$

In equations 2.17, 2.19 and 2.20 B_h represents the h^{th} linear B spline. This basis function is defined as zero outside the region of the radius bin and linearly interpolates the function within it. Figure 2.3 shows a visualization of this matrix calculated using the complex ratio of sound speeds. It is plotted for a range of bubble radii from 1 μm to 1 mm and, for clarity, on both linear and logarithmic scales. Since the real part of the K matrix is negative above the bubble's resonance, the logarithmic plot of the real part is the absolute value. A similar visualization of a matrix of extinction cross-sections would, obviously, contain no imaginary part.

The interpretation of the elements contributing to this matrix is as follows:

- Elements lying along the leading diagonal correspond to the scattering caused by bubbles being driven at their resonance frequency;

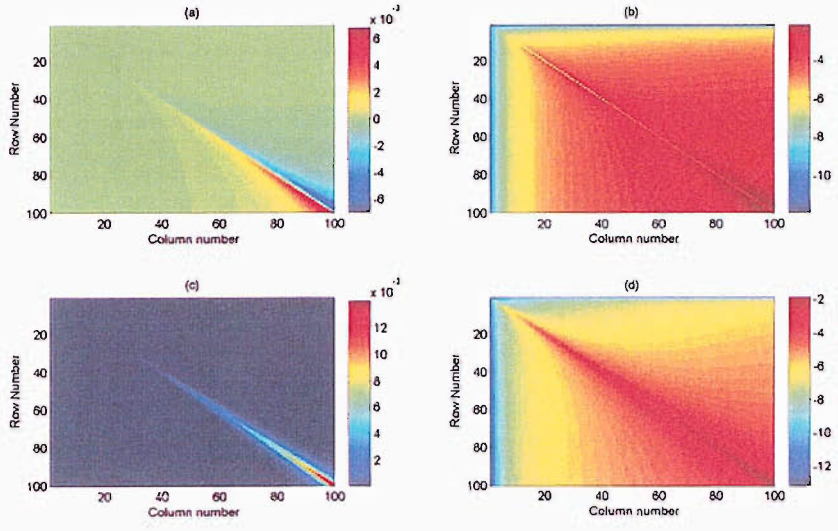

Figure 2.3: Elements of K Matrix plotted for bubble radii ranging from 1 μm to 1 mm. (a) Real part of K matrix (linear scale) (b) Absolute value of real part of K matrix (log scale) (c) Imaginary part of K matrix (linear scale) (d) Imaginary part of K matrix (log scale).

- Elements in the lower left portion of the matrix correspond to small bubbles when driven at low frequencies;
- Elements in the upper right portion of the matrix correspond to large bubbles when driven at high frequencies.

Once this matrix is calculated it is a simple process to calculate the propagation characteristics for a given bubble population. The next two sections will solve the forward problem for both artificial and measured bubble populations.

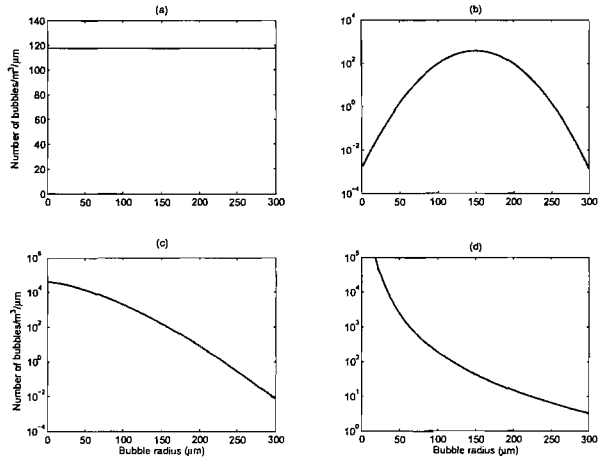

Figure 2.4: Synthetic bubble populations (a) Uniform (b) Gaussian (c) Exponential (d) Power Law.

2.1.4 Solution of forward problem: Synthetic data

In order to demonstrate the methods described in the previous section, the forward problem will be solved for four synthetic bubble populations. The attenuation will be calculated using the complex ratio of sound speeds, its binomial expansion and the extinction cross section while the phase speed will only be calculated using the complex ratio of sound speed and the binomial expansion. The synthetic populations were taken from Commander & McDonald [18] and the results compared to those shown in the paper. The trial populations used are shown in figure 2.4. The attenuations and phase speeds calculated using the different methods are shown in figures 2.5 and 2.6 respectively.

The results from all three methods match exactly those presented by Commander and McDonald. This gives confidence for the prediction of the likely propagation characteristics of oceanic bubble populations based upon previous data, which is the subject of the next section.

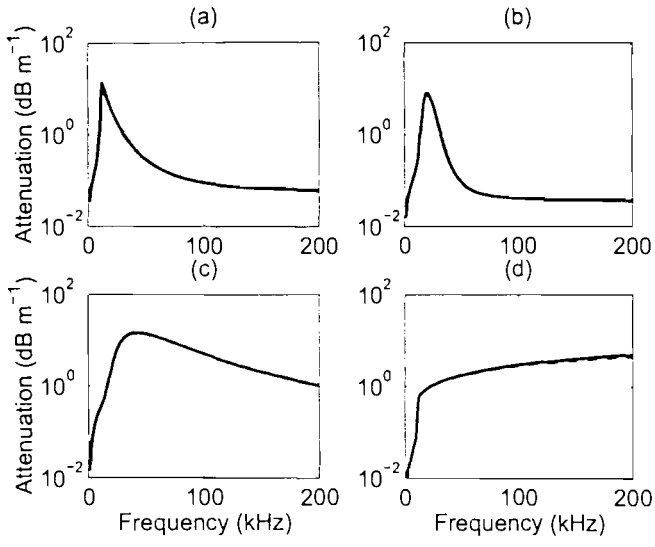

Figure 2.5: Attenuation calculated using the complex ratio of sound speeds, its binomial expansion and the extinction cross section (all three curves overlay each other) for four synthetic bubble populations. (a) Uniform (b) Gaussian (c) Exponential (d) Power Law.

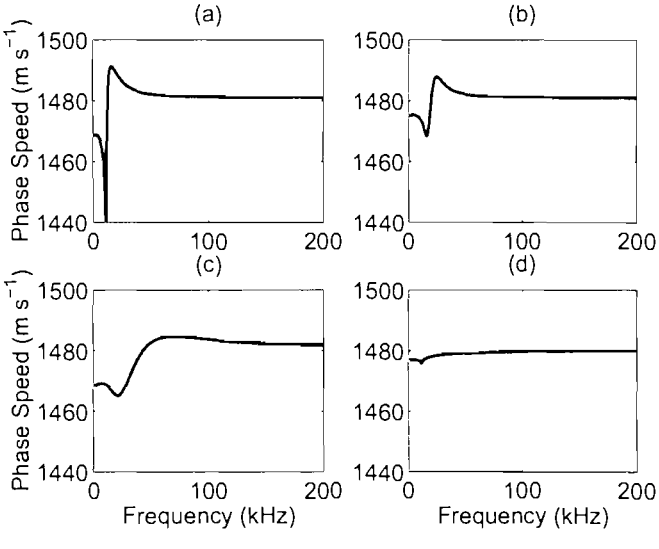

Figure 2.6: Phase speed calculated using the complex ratio of sound speeds and its binomial expansion (the curves overlay each other) for four synthetic bubble populations. (a) Uniform (b) Gaussian (c) Exponential (d) Power Law.

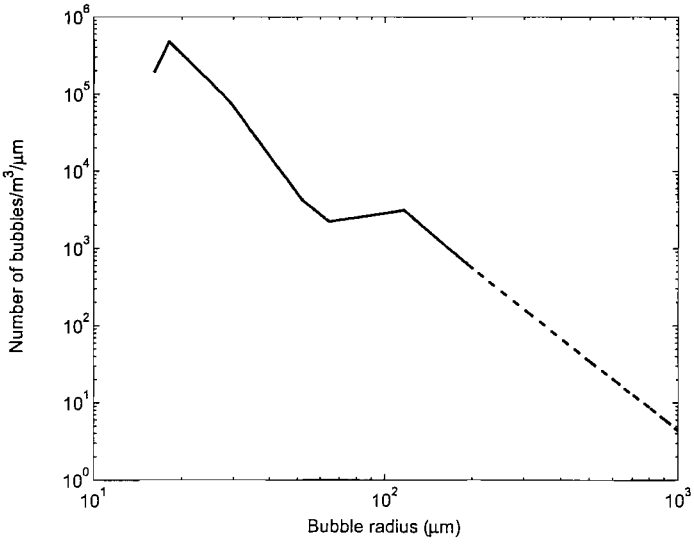

Figure 2.7: Oceanic bubble population obtained using the combination frequency technique [45] in open water. The extrapolated curve has a gradient of R^{-3} and the calculated void fraction is 1.7×10^{-6}.

2.1.5 Solution of forward problem: Oceanic data

Knowledge of the likely propagation characteristics in realistic oceanic environments is vital for rigorous development of a technique for measuring oceanic bubble populations. A number of previous investigators [6, 20, 43–46] have made measurements of oceanic bubble populations, primarily in open ocean.

A representative open ocean bubble population is that taken by Phelps & Leighton [45]. It was obtained using a combination frequency technique at 10 bubble radii equally space between 16 μm and 192 μm in water depths ranging from 17 to 22 m and wind speed gusting up to 16 ms^{-1}. Figure 2.7 shows the measured population and an extrapolation of the data to larger bubble sizes for the estimation of void fraction. The extrapolation is taken up to 1 mm. Bubbles above this radius will be very few in number due to their large buoyancy and can be expected to make minimal contribution to the total void fraction. The void fraction of a population described by H radius bins is calculated by

$$V_F = \sum_{h=1}^{H} \frac{4}{3}\pi R_{0_h}^3 n_h \tag{2.22}$$

Using the population measured by Phelps & Leighton as an input into the forward problem, an estimate can be made of the likely agreement between the three different models developed above at oceanic void fractions. Figure 2.8(a) shows the phase speed predicted by two techniques (the complex sound speed and the binomial expansion) and figure 2.8(b) shows the attenuation predicted by all three of the techniques. As can be seen from the figure the two curves based upon the ratio of complex sound speeds overlay each other and disagree slightly at high frequency with the extinction cross section. The maximum extent of the disagreement occurs at 150 kHz and is 0.72 m/s in the phase speed and 0.21 dB in the attenuation. This could be explained by differences in the two damping models used. However at a typical open ocean void fraction, the complex sound speed and the binomial expansion agree well.

The open water bubble population gives rise to an attenuation as high as 30 dB/m. The high attenuation experienced in bubbly liquids can make measurement of acoustic propagation demanding, especially in the surf-zone where void fractions are expected to be higher than those encountered in open ocean. Only two of these investigations mentioned above [6, 44] have made measurements directly in the surf-zone and only one [6] made measurements at bubble radii $< 100\mu$m. However this measurement was at a small number of bubble radii and was taken during stormy conditions directly under breaking waves. Figure 2.9 shows the estimated population. Again, the void fraction has been estimated by extrapolating the data. However in this case only four data points exist which cover a limited radius range (35 μm to 150 μm). Therefore the validity of the extrapolated curve is questionable but does give an indication of the order of magnitude to be expected.

Figure 2.10 shows the phase speed and attenuation predicted by the forward models for that population. It should be emphasized that figure 2.10 has been calculated using a linear model, and many of the assumptions in-

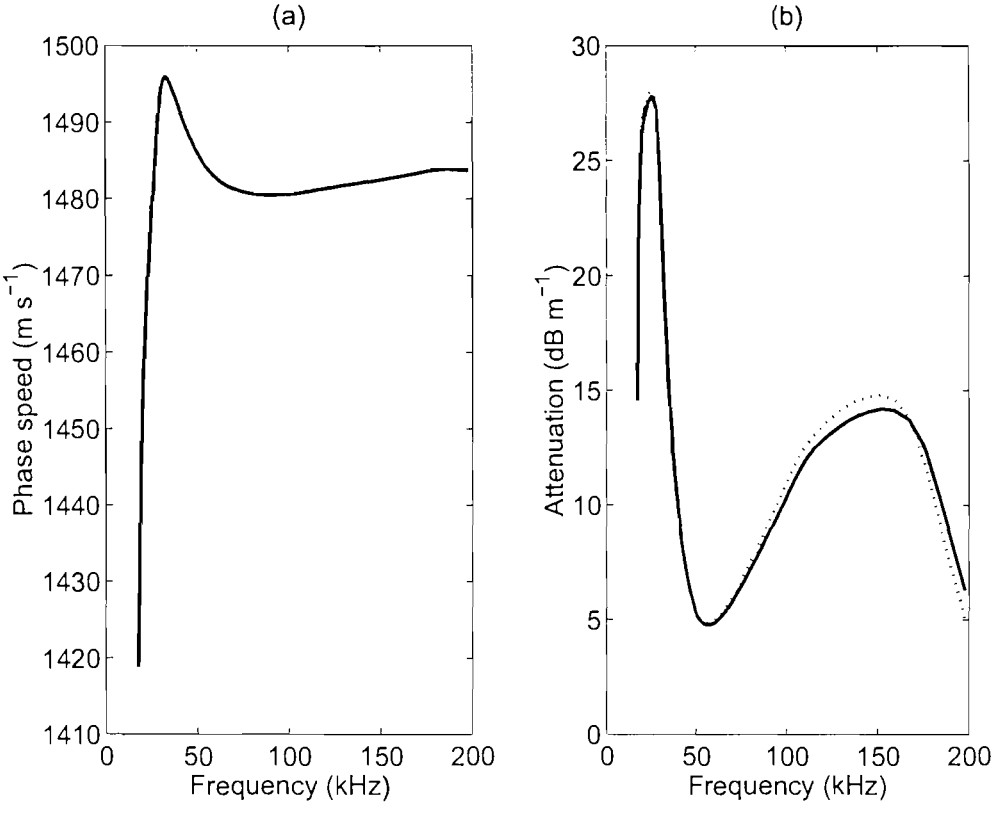

Figure 2.8: Acoustic propagation characteristics in a typical open water oceanic bubble population (a) phase speed calculated using two different techniques: the ratio of complex sound speeds (solid) and the binomial expansion (dashed) (b) attenuation calculated using three different techniques: the ratio of complex sound speeds (solid), the binomial expansion (dashed) and the extinction cross section (dotted). The maximum disagreement in attenuation between the three models is 0.21 dB/m.

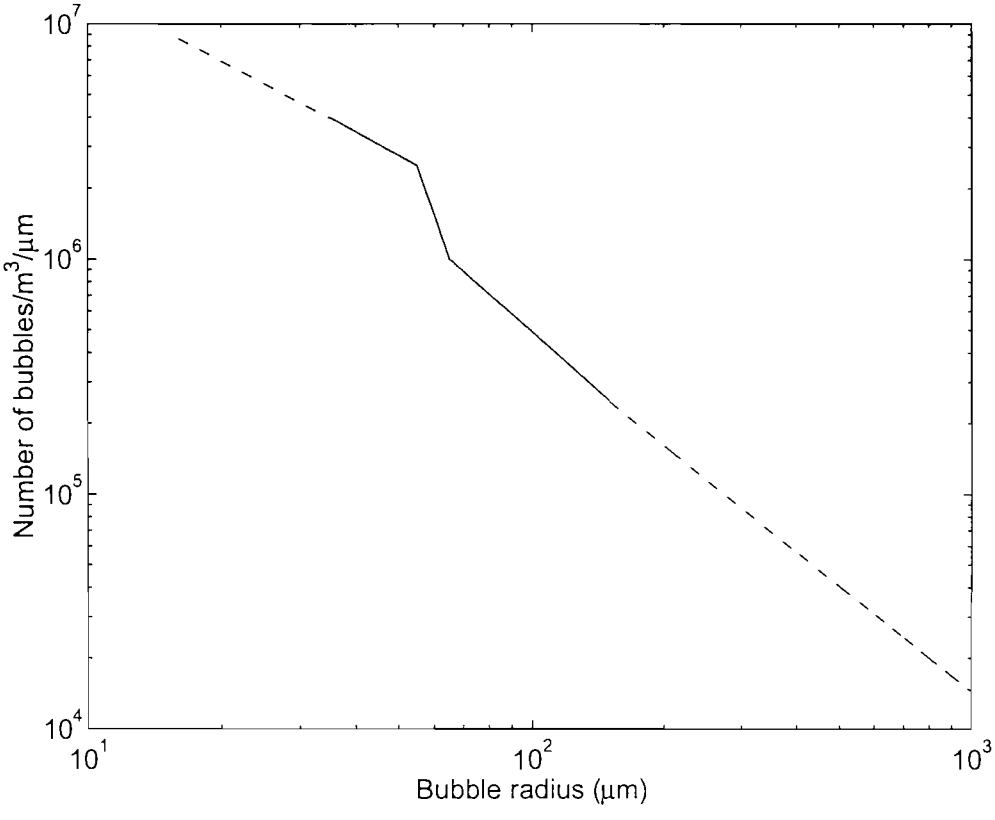

Figure 2.9: Surf-zone bubble population obtained using the combination frequency technique [6] in stormy conditions directly under breaking waves. Notice the different y-scale from figure 2.7. The population is extrapolated with a gradient of R^{-1} at the small radii and $R^{-1.5}$ at the large radii. The calculated void fraction is 0.0241 but is based upon an extrapolation from a very limited data set.

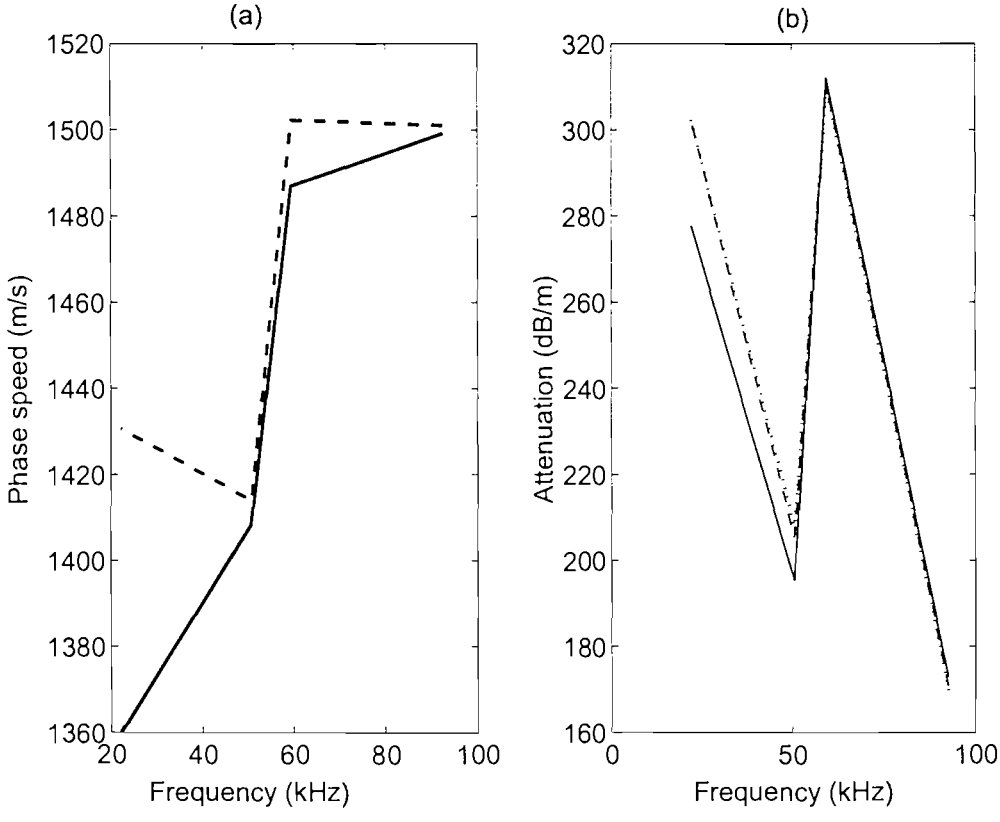

Figure 2.10: Acoustic propagation characteristics in a stormy surf-zone bubble population directly under a breaking wave (a) phase speed calculated using two different techniques: the ratio of complex sound speeds (solid) and the binomial expansion (dashed) (b) attenuation calculated using three different techniques: the ratio of complex sound speeds (solid), the binomial expansion (dashed) and the extinction cross section (dotted). The dashed and dotted curves almost overlay one another. *Owing to the small number of radii at which the measurement was made, predictions only exist at four frequencies. The line connecting these points is for clarity only and does not imply measurements at intermediate frequencies. These results are for indication only and are likely to be in error due to the assumptions made in the model.*

herent in that model may be invalid for this dense population. The results are likely to be in error but are shown in order to indicate the magnitude of effects that could be experienced in extreme surf-zone conditions. The level of agreement between the models is surprising, especially in the predictions of attenuation. The extinction cross-section and the binomial expansion agree particularly well with a maximum difference of 2.6 dB (less than one percent of the total). The discrepancy between those two and the full ratio of sound speeds is greater with a maximum difference of 25 dB (approximately 8 percent). When considering the phase speed the discrepancy ranges between 1.8 and 70 m/s.

As can be seen in figure 2.10 the attenuation experienced in the surf-zone could be expected to be in excess of 100 dB/m. This illustrates the difficulty of making measurements in this extremely challenging environment, especially, as will be seen later, as the receiver should be positioned in the far field of the source. When considering that a receiver may have to be O(1m) away from the source to satisfy the far-field condition, it can be seen that surf-zone measurements are very challenging indeed. However, the population modelled represents very extreme conditions, and it may be that in more moderate conditions, not directly underneath the breaking waves surf-zone, measurements may become practical.

2.1.6 Summary of forward solution

The first section of this chapter has developed a method of predicting the acoustic propagation characteristics in a known cloud. The supporting theory was outlined using three different expressions. The complex ratio of sound speeds and its binomial expansion were used to determine phase speed and attenuation while the extinction cross section was used to determine attenuation only. The three models were shown to agree within the range of expected oceanic bubble populations with small discrepancies entering at very high void fractions in the surf-zone. A range of synthetic populations were tested and compared to the results of other investigators. Finally the propa-

gation characteristics were calculated based on measured oceanic data both in open ocean and in the surf-zone. The surf-zone population indicated very high attenuation, but the measurements were taken in very stormy conditions directly under breaking waves. This served to illustrate the challenges that will be encountered in making surf-zone bubble population measurements. While this section has laid down a formulation of the problem, relating bubble number to acoustic propagation characteristics, the inverse solution is more problematic and is the subject of the next section in this chapter.

2.2 The inverse problem

Initial consideration of the inverse problem based upon a knowledge of the forward problem would indicate a relatively straightforward process. In order to estimate the bubble population the vector of propagation characteristics, $\boldsymbol{\alpha}$ is multiplied by the inverse of the matrix of bubble responses

$$\boldsymbol{n} = \boldsymbol{K}^{-1}\boldsymbol{\alpha} \tag{2.23}$$

However, owing to the fact that geometrical scattering causes $\boldsymbol{K}$ to have significant off-diagonal elements (as discussed in sections 1.1.2 and 2.1) the matrix becomes poorly conditioned and is therefore the solution becomes very sensitive to noise. Take, for example, the open ocean population for which the forward problem was solved in section 2.1.5 (figure 2.7). Using standard Gaussian elimination as the method for inverting the matrix $\boldsymbol{K}$ produces an accurate answer when no noise is added. However, when Gaussian noise of just one thousandth of one percent on the mean value is added the solution becomes wildly unstable and meaningless. Figure 2.11 shows the two solutions. Since real measurements will suffer from much greater levels of noise, this method of inversion is of little or no use for experimental work. Therefore a more robust method of inverting '$\boldsymbol{K}$' must be developed and this is the topic of the next section.

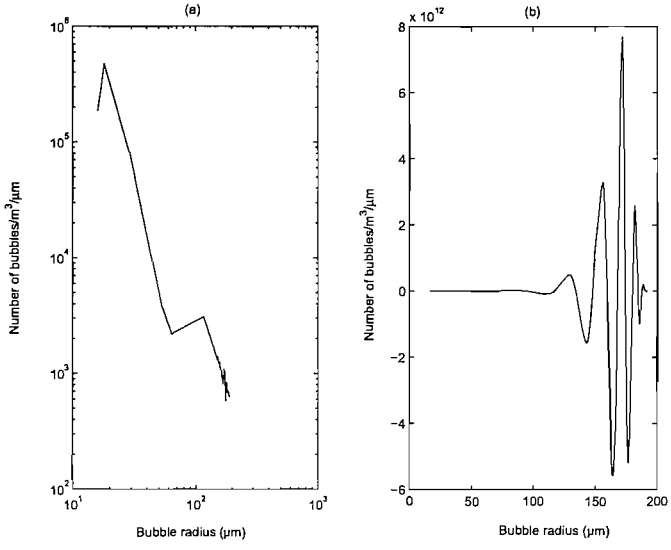

Figure 2.11: Inverted solution (using Gaussian elimination) for acoustic propagation characteristics shown in figure 2.8 with and without Gaussian noise added (a) No noise added (b) 0.001% Gaussian noise added.

2.2.1 Regularisation techniques

The material in this subsection was developed with assistance from Prof. P. A. Nelson and his input is acknowledged.

A widely used technique for inverting ill-conditioned matrices, such as the '$\boldsymbol{K}$' matrix, is *Tikhonov* regularisation [47]. This technique relies upon adding a matrix (usually the identity matrix), scaled by β, a regularisation parameter, to the matrix to be inverted. This has the effect of stabilizing the inverse of the matrix. Where possible the techniques will be discussed based on both real and complex values in order that inverse solutions are possible for all the models discussed in section 2.1.

If $\hat{\boldsymbol{\alpha}}$ represents the modelled input values to the system and $\boldsymbol{\alpha}$ the measured input values then modelling the measured signal as the modelled signal plus a noise vector gives

$$\begin{aligned} \hat{\alpha} &= Kn \\ \alpha &= \hat{\alpha} - e \end{aligned} \tag{2.24}$$

The solution to find an optimal value of n varies depending on whether real values (such as attenuation *or* phase speed) or complex values (both attenuation *and* phase speed) are used in the vector α and the matrix K. In both cases, n, the vector of bubble numbers, is, of course, real.

(a) Real values

The function to be minimized is given by equation 2.25 and represents a compromise between the sum of the squared errors and a weighted sum of the squared solutions.

$$\Psi = e^T e + \beta n^T n \tag{2.25}$$

The superscript T denotes the transpose of the vector/matrix. Since

$$e = \alpha - Kn \tag{2.26}$$

$$\begin{aligned} \Psi &= (\alpha - Kn)^T(\alpha - Kn) + \beta n^T n \\ &= \alpha^T\alpha - n^T K^T\alpha - \alpha^T Kn + n^T K^T Kn + \beta n^T n \\ &= n^T(K^T K + \beta I)n - (n^T K^T\alpha + \alpha^T Kn) + \alpha^T\alpha \end{aligned} \tag{2.27}$$

Since $n^T K^T\alpha$ and $\alpha^T Kn$ are both scalars equation 2.27 can be rewritten

$$\Psi = n^T(K^T K + \beta I)n - 2\alpha^T Kn + \alpha^T\alpha \tag{2.28}$$

In order to find the optimal solution, it is necessary to find the minimum of Ψ. This is done by differentiating and setting the result equal to zero. The differentiation is performed by exploiting two standard identities given in equations 2.29 and 2.30.

$$\frac{\partial \boldsymbol{x}^T \boldsymbol{A} \boldsymbol{x}}{\partial \boldsymbol{x}} = (\boldsymbol{A} + \boldsymbol{A}^T)\boldsymbol{x} \tag{2.29}$$

$$\frac{\partial \boldsymbol{A}^T \boldsymbol{x}}{\partial \boldsymbol{x}} = \boldsymbol{A} \tag{2.30}$$

These identities allow calculation of the derivative.

$$\begin{aligned} \frac{\partial \Psi}{\partial \boldsymbol{n}} &= ((\boldsymbol{K}^T\boldsymbol{K} + \beta\boldsymbol{I}) + (\boldsymbol{K}^T\boldsymbol{K} + \beta\boldsymbol{I})^T)\boldsymbol{n} - 2\boldsymbol{K}^T\boldsymbol{\alpha} \\ &= 2((\boldsymbol{K}^T\boldsymbol{K} + \beta\boldsymbol{I})\boldsymbol{n} - \boldsymbol{K}^T\boldsymbol{\alpha}) \end{aligned} \tag{2.31}$$

Setting $\frac{\partial \Psi}{\partial \boldsymbol{n}} = 0$ and rearranging for n gives

$$\boldsymbol{n}_{opt} = (\boldsymbol{K}^T\boldsymbol{K} + \beta\boldsymbol{I})^{-1}(\boldsymbol{K}^T\boldsymbol{\alpha}) \tag{2.32}$$

(b) Complex values

The function to be minimized in the complex case is similar to equation 2.25 and is given by equation 2.33 where the superscript H represents the hermatian of the vector/matrix i.e. its transposed conjugate $(\boldsymbol{X}^*)^T$.

$$\Psi = \boldsymbol{e}^H\boldsymbol{e} + \beta\boldsymbol{n}^T\boldsymbol{n} \tag{2.33}$$

Similar simple algebra to that outlined above yields the following result.

$$\boldsymbol{n}_{opt} = (\boldsymbol{K}^H\boldsymbol{K} + \boldsymbol{K}^T\boldsymbol{K}^* + 2\beta\boldsymbol{I})^{-1}((\boldsymbol{K}^H\boldsymbol{\alpha}) + (\boldsymbol{K}^H\boldsymbol{\alpha})^*) \tag{2.34}$$

Since $\boldsymbol{K}^H\boldsymbol{K}$ and $\boldsymbol{K}^T\boldsymbol{K}^*$ are complex conjugates, equation 2.34 could be re-written in a form analogous to equation 2.32.

$$\boldsymbol{n}_{opt} = \Re\left\{(\boldsymbol{K}^H\boldsymbol{K} + \beta\boldsymbol{I})^{-1}(\boldsymbol{K}^H\boldsymbol{\alpha})\right\} \tag{2.35}$$

In both the real and complex cases the success of the inversion is determined by the value of β. When β is large, the matrix being inverted will

tend towards a scaled vector, $\boldsymbol{K}^H\boldsymbol{\alpha}$, and where β is small the instabilities caused by the ill-conditioned matrix will cause large errors in the solution. The key to successful inversion using this technique is choosing the correct value of β. There are many different methods of achieving this which will be discussed in the next sub-section.

2.2.2 Determination of the regularisation parameter

Previous investigators have performed the inversion of the ill-conditioned matrix $\boldsymbol{K}$ by imposing physical constraints upon the solution [18, 19] (for example upon the smoothness of the solution). However such methods merely render the solution stable rather than systematically determining the amount of regularisation to add.

A commonly used systematic method of determining the optimal amount of regularisation to add to ill-conditioned matrices is the L-curve method, first developed by Hansen [48, 49]. It plots the Euclidian norm of the regularised solution $\|\boldsymbol{L}\boldsymbol{n}\|_2$ (where $\boldsymbol{L}$ is the additional matrix used for regularisation, in this case the identity matrix) against the corresponding residual norm $\|\boldsymbol{K}\boldsymbol{n} - \boldsymbol{\alpha}\|_2$ (which can also be written $\|\boldsymbol{e}\|_2$ for a given value of β). This, when plotted on a logarithmic scale, forms a well characterized 'L' shaped curve, the corner of which represents a compromise solution between an over and an under regularised solution.

Figure 2.12 shows the curve plotted when attempting to invert propagation characteristics calculated using the forward technique (section 2.1) with 1% noise added to the phase speed and attenuation. The population used was the open ocean population measured by Phelps & Leighton [45] (section 2.1.5). As can be seen when β is small the value of $\|\boldsymbol{n}\|_2$ is large and $\|\boldsymbol{e}\|_2$ is small, indicating a good agreement between measured and modelled values of $\boldsymbol{\alpha}$ but an unstable solution (see figure 2.11(b)) of $\boldsymbol{n}$. When β is large $\|\boldsymbol{n}\|_2$ is small and $\|\boldsymbol{e}\|_2$ is large, indicating a more stable value of $\boldsymbol{n}$ but a larger error between measured and modelled values of $\boldsymbol{\alpha}$.

Numerically the corner of the 'L' corresponds to the maximum curvature

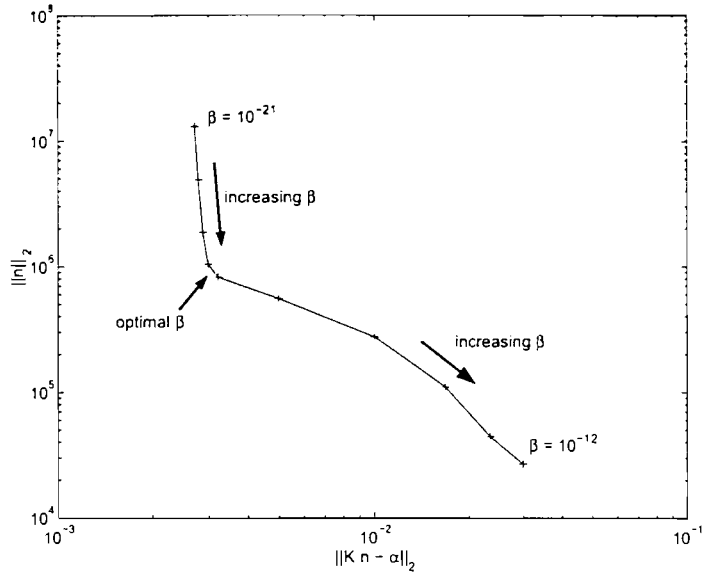

Figure 2.12: A typical L-curve used during inversion to determine the optimal value of β. Curve calculated with 1% noise added to the inputs. The optimal solution lies at the corner of the 'L'.

of the curve given by

$$C(y) = \frac{|z_n''|}{(1 + z_n'^{\,2})^{3/2}} \tag{2.36}$$

where $z_n = \|\boldsymbol{n}\|_2$ and $y = \|\boldsymbol{e}\|_2$ and the primes refer to first and second derivatives with respect to y.

2.2.3 Solution of inverse problem: Synthetic data

This section will aim to reconstruct four synthetic bubble populations: uniform, Gaussian, exponential and power law using the L-curve technique for determining the matrix regularisation parameter. The acoustic propagation characteristics[1] calculated using equation 2.9 (figures 2.5 and 2.6) were used as an input to the inverse problem in an attempt to recover the original populations (figure 2.4).

[1] At this stage both phase speed and attenuation are used.

Figure 2.13 shows the populations estimated via inversion for each of the different bubble populations with 0.001% Gaussian noise added to the input. This quantity of noise rendered the solution unstable when using standard Gaussian elimination to invert the matrix. As can be seen, the technique has generally been successful at reconstructing the populations but at very low numbers of large bubbles begins to diverge from the original population.

Figure 2.14 shows the population estimated with a greater amount of noise added (1%). As can be seen significant inaccuracies are beginning to occur at different parts of the radius spectrum. For example the uniform distribution significantly under-estimates the population below 100 μm. This is due to the scattering by large off-resonant bubbles. However, while these estimation of these synthetic populations is a useful exercise in testing and understanding the performance of the regularisation algorithm they bear little resemblance to real oceanic populations. A more valid test would use historical oceanic data. This will be the subject of the next section.

2.2.4 Solution of inverse problem: Oceanic data

This section will estimate the population from the propagation characteristics solved using the forward problem in section 2.1.5 with Gaussian noise added to the characteristics to simulate the effect of measurement noise. Figures 2.7 and 2.8 show the populations and their predicted propagation characteristics. The L-curve technique will be used to regularise the solution. Figure 2.15 shows both the original input population and the result estimated when 0.001% measurement noise is added. This small value of noise rendered the inversion unstable using standard Gaussian Elimination owing to the ill-conditioning [47] of the matrix being inverted. As can been seen the regularised solution is now in good agreement with the original population.

Figure 2.16 shows the estimation based upon the same oceanic population but this time adding 1% Gaussian noise to the input. While the solution is accurate for the small bubble radii, where the number of bubbles is large, it is less accurate for the large radii where the bubble numbers are smaller.

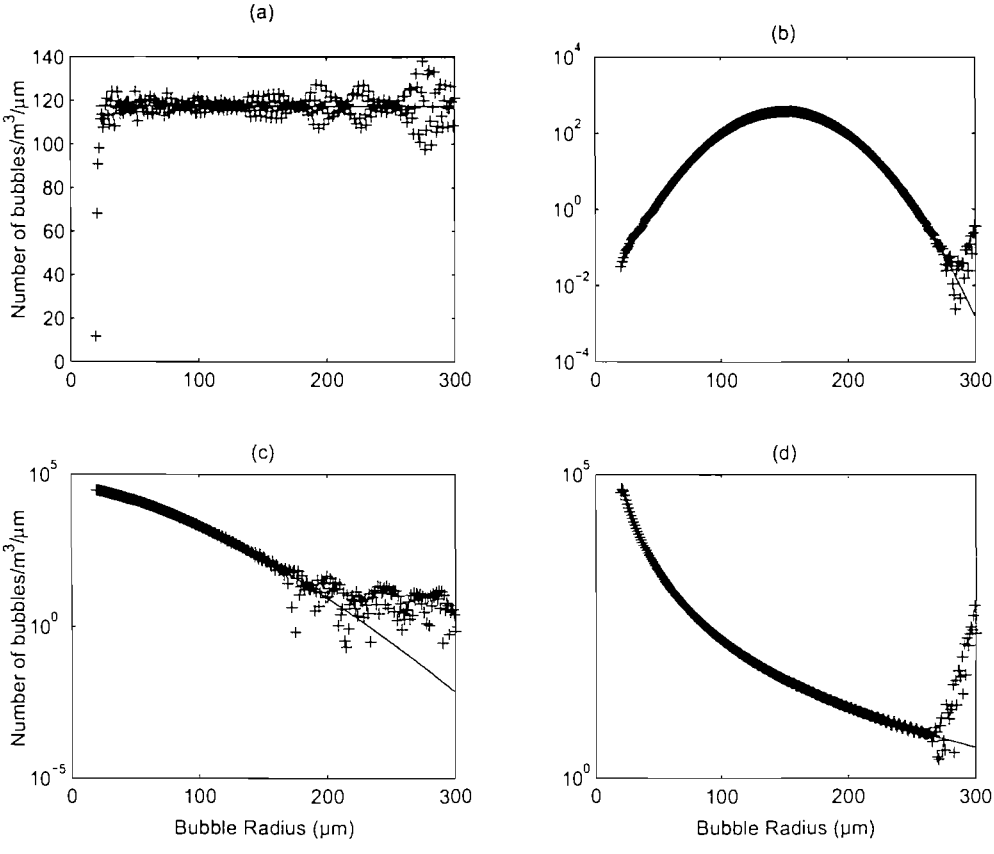

Figure 2.13: Synthetic bubble populations estimated from propagation characteristics predicted using forward problem with 0.001% Gaussian noise added. The continuous line represents the input population and the crosses (+) the estimated population. (a) Uniform distribution (b) Gaussian distribution (c) Exponential distribution (d) Power law distribution. The inversion was performed using the L-curve method and was based upon a complex kernel (equation 2.9). The bin size used was 1 μm.

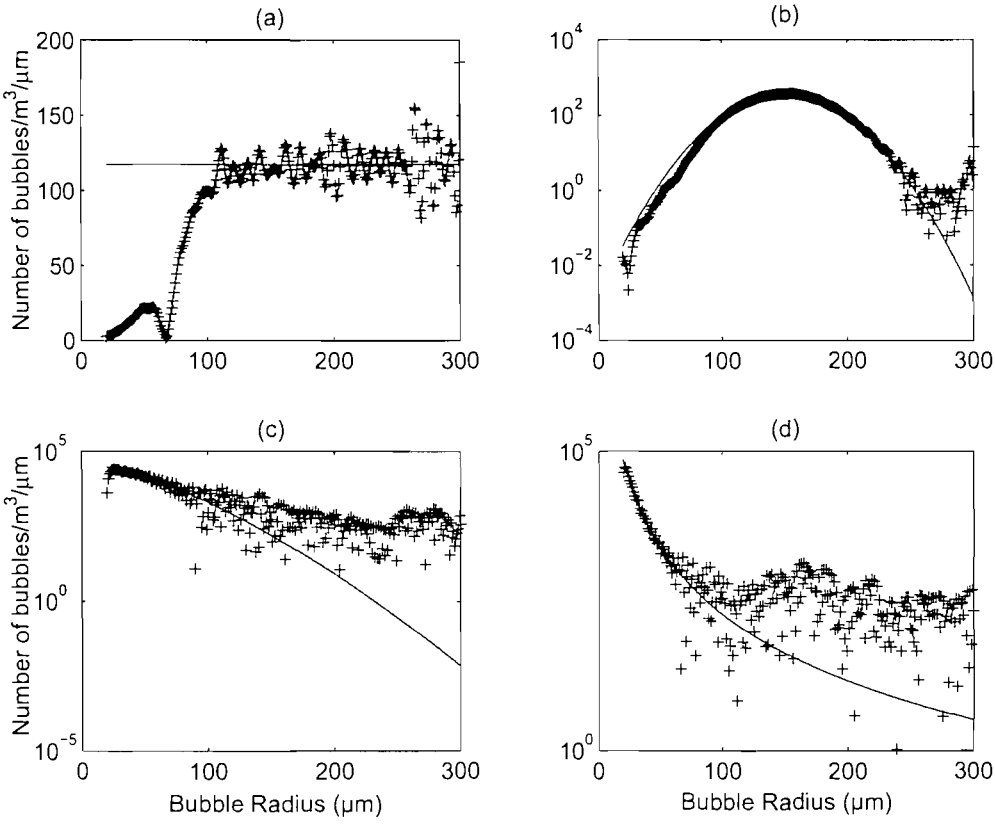

Figure 2.14: Inverted data for the four synthetic bubble populations with 1% Gaussian noise added to the input propagation characteristics. The continuous line represents the input population and the crosses (+) the estimated population.

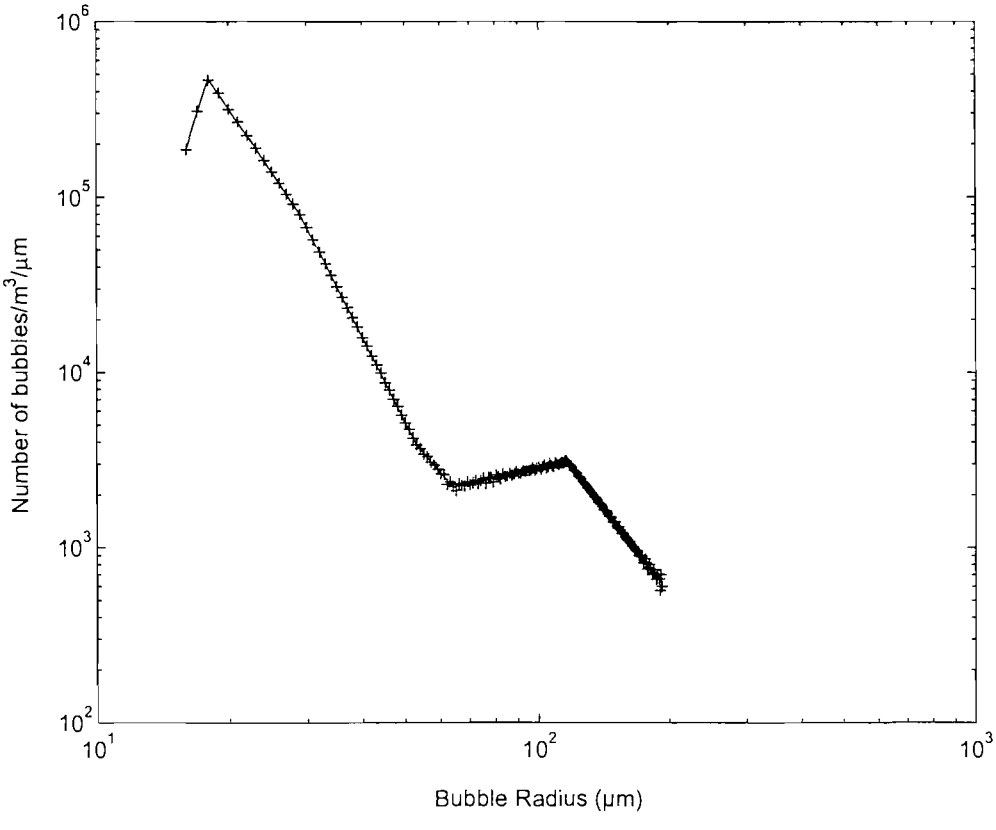

Figure 2.15: Population estimated via L-curve technique with 0.001% noise. The continuous line represents the input population and the crosses (+) the estimated population. N.B. With no regularisation the addition of noise rendered the solution unstable (see figure 2.11).

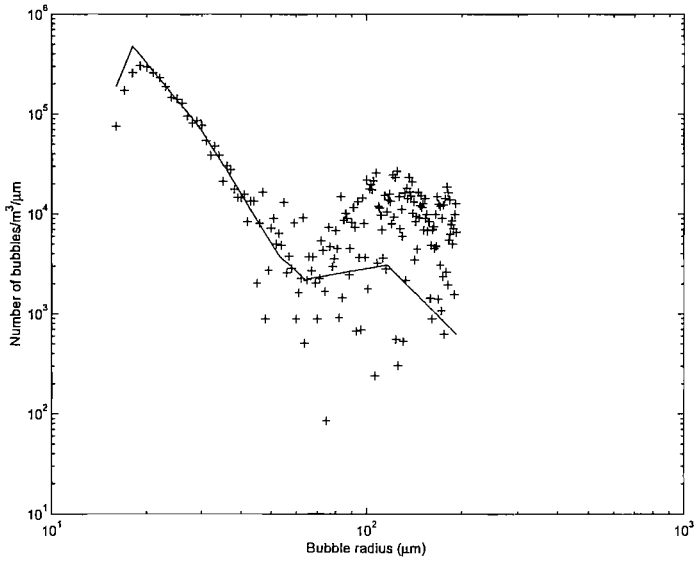

Figure 2.16: Population estimated via L-curve technique with 1% noise. The continuous line represents the input population and the crosses (+) the estimated population.

The error in the inverted solution may be minimized by increasing the bin size used to evaluate the bubble population. Practically speaking, it is likely that be bubble population will be measured using a coarse bin size and the results scaled to be quoted per μm. Figure 2.17 shows the estimation performed using 2, 3, 5 and 10 μm radius bins. The amount of Gaussian noise added is kept constant at 1% throughout.

As can be seen in figure 2.17, increasing the size of the radius bins improves the accuracy of the estimate. This is because the condition number [47] (which is the ratio of the largest to the smallest singular value of the matrix being inverted) becomes smaller as the radius bins become larger. A matrix with a low condition number is less prone to instabilities than one with a high condition number [49]. Table 2.1 shows how matrix size and condition number varies as a function of radius bin size for the oceanic population under consideration.

However, increasing the size of the radius bins has the affect of 'smearing'

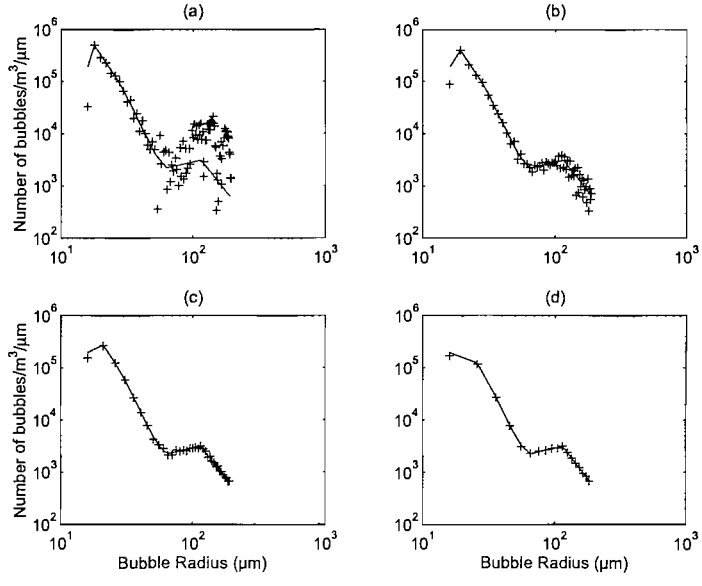

Figure 2.17: The effect of radius bin size upon inverse estimation (a) 2 μm bin (b) 3 μm bin (c) 5 μm bin (d) 10 μm bin. The amount of noise is kept constant at 1%.

Bin Size (μm)	Matrix Size	Condition Number
1	177×177	3.1×10^{15}
2	89×89	3.2×10^{7}
3	59×59	7.4×10^{4}
5	36×36	1.3×10^{4}
10	18×18	5.5×10^{3}

Table 2.1: Matrix size and condition number as a function of bin radius.

the distribution because the magnitude of the bin represents the integral of all the bubble radii falling within the boundary of the bin. It should be noted in figure 2.17 that the largest bin size, (d), obscures the peak in the distribution, therefore it is desirable to keep the size of the radius bins low in order to adequately resolve the characteristics of the population.

2.2.5 Summary of inverse solution

A demonstration was made of the inherent problems encountered when attempting to make an estimate of bubble populations using inverse methods. A technique was then outlined to overcome such difficulties which made use of a least squares fit solution via Tikhonov regularisation. This solution was then implemented on a variety of synthetic populations and real oceanographic measurements. This showed that, while accurate estimates can be made with low noise levels, the inaccuracy becomes intolerable for large amounts of noise. It was then shown how reducing the number of radii under consideration helps de-sensitize the solution to noise. However reducing the number of radii was shown to 'smear' the estimated population, and hence it is beneficial to make measurements with as little noise as possible. All the inverse results presented in this chapter have been based upon complex kernels. However exactly the same techniques apply to real kernels (whether based on complex sound speed or extinction cross section).

The discussion up until this point has mainly focused upon the formulation of the problem and methods of solution without consideration of the inherent acoustics. It is important that these considerations are made and their implications appreciated when making any estimates as contravening the assumptions will effect the validity of the estimate. This discussion will form the subject of the next section.

2.3 Consideration of inherent assumptions

In order to assess the validity of any given estimate of bubble population, it is necessary to appreciate the theoretical assumptions that have been made in obtaining that estimate. The two models used in section 2.1 (the ratio of complex sound speeds and the extinction cross section) are widely employed in existing techniques and make similar assumptions about the response of the bubble and the field driving it. The validity of these assumptions must be assessed when considering the reliability of a given estimate of bubble population obtained using them. The key assumptions are

1. that the acoustic propagation in the bubbly medium is planar;
2. that the bubble oscillates in a free field;
3. that the bubble oscillations are monochromatic (i.e. single frequency which implies linearity).

The following sections will address each of these assumptions in turn specifically considering the case of high amplitude propagation in the surf-zone. This is one of the most challenging of oceanographic environments and also one for which there is the least amount of measured data.

2.3.1 Plane wave propagation

There are two different cases that must be considered when assessing the planarity of a wave: the direct radiation from the source and the arrival of indirect radiation. The former of these two cases refers to the geometry of the field radiated on a direct path from the source. The latter case refers to waves which have traveled an indirect path most commonly by reflection from ocean surface or the ocean floor. The two cases are considered separately.

First consider the direct case: given that the source is radiating into a free field, what conditions must be met in order that plane wave propagation is experienced? Any sound source may be modelled as a collection of

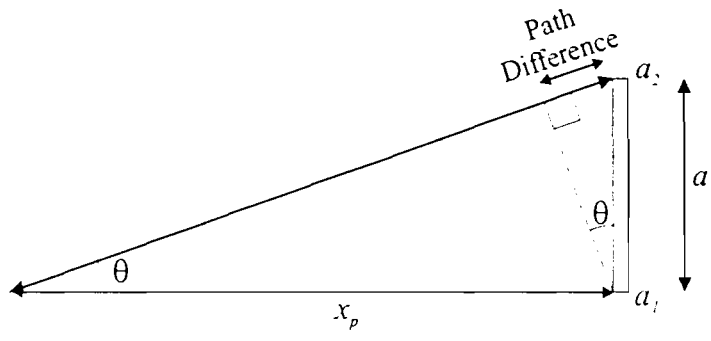

Figure 2.18: A distributed line array of point sources. When x becomes large the path difference is negligible and hence the phase difference between the radiated waveforms is close to zero. When x_p is small the phase difference is significant.

point sources, which are considered to radiate spherical acoustic waveform independently of one another. The resultant waveform can be calculated by the summation of the radiated pressures. Consider a line array, length a, of such point sources all radiating in phase with one another where a_1 and a_2 represent the point sources at each end of the line array (see figure 2.18).

If x_p is the perpendicular distance from the source, it can be seen that as x_p tends to infinity the difference between the path lengths from a_1 and a_2 compared to the wavelength of the sound being radiated becomes negligible. This implies that the phase difference of the waveforms radiated from a_1 and a_2 at point x_p is also negligible. From this it can be inferred that plane wave propagation is occurring. This region is referred to as the far-field of the transducer.

If x_p is small, and hence the path differences are significant compared to the wavelength, the phase relationship becomes important and the summation of the waveforms from each point source must include their phase relationship. This can lead to complicated spatial pressure patterns being formed. This region of the pressure field emitted by a transducer is referred to as the near-field of the transducer.

In order to determine the value of x_p for which far-field effects become

dominant, it is necessary to consider the relationship between the length of the array of point sources, a, and the wavelength of the acoustic field being radiated, λ. Using standard trigonometry it can be seen from figure 2.18 that the path difference, d, between the radiated waveforms from a_1 and a_2 is

$$d = a\sin\theta \approx a\tan\theta = \frac{a^2}{x_p} \tag{2.37}$$

(small angle approximation)

From this it can be seen that when $x_p > a^2/\lambda$ the the path difference will be less than a wavelength which acts as a first approximation for the boundary of the near-field. Any measurements that are made assuming a plane wave should therefore be made at a distance greater than a^2/λ.

The second of the two cases mentioned above refers to sound radiation from the source arriving at the measurement point by an indirect route, most commonly by reflection from the ocean floor/surface. The problem of multi-path reflections can be overcome by windowing the received waveform in such a way that data received after the time of arrival of the first reflection is ignored. This effectively puts a limit on the duration of the acoustic pulse that can be used to insonify the bubble cloud. Simple geometry shows that the difference in arrival times of the direct and indirect pulse, t_p, for a source and receiver separated by distance x, with a perpendicular distance of x_r to the nearest reflecting surface is

$$t_p = \frac{1}{c_w}\left(2\sqrt{\left(\frac{x}{2}\right)^2 + x_r^2} - x\right) \tag{2.38}$$

where the sound speed in the medium is assumed to be the sound speed in pure water, c_w (in bubbly mixtures this may vary slightly). For example, in water two metres deep with a source positioned at a depth of one metre and a distance between that source and a receiver of two metres (to account for being in the far field) t_p would be $\sim$560 μs.

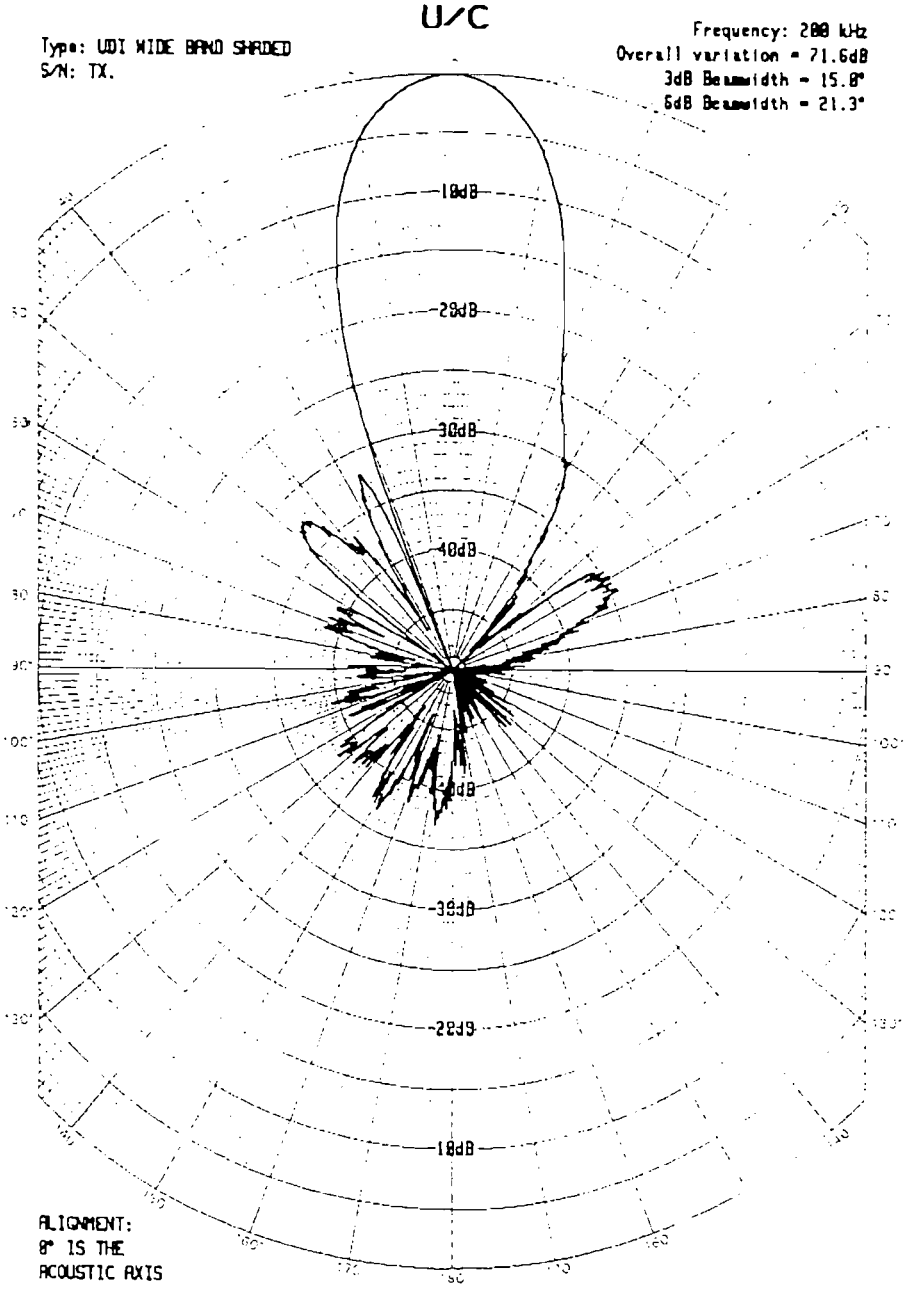

Figure 2.19: Beam pattern for a directional transducer at 200 kHz. The main beam width for this transducer is approximately 8 degrees and side lobes are 30-35 dB less than the main lobe. *Acknowledgement: H. A. Dumbrell, Dstl*

An alternative would be to employ a directional transducer with a focused beam-pattern in order that the reflections were minimized. Figure 2.19 shows a beam-pattern for a directional transducer taken at 200 kHz as an illustration. Use of such a transducer would not impose a restriction on the pulse duration of the driving signal providing it could be assumed that the transducer radiated negligible sound power outside the angle θ of its main beam and that the main beam was sufficiently narrow that reflected paths did not intersect with the receiver. However for a physically realisable transducer it is inevitable that there will be some radiation of sound from outside the transducer's main beam and the level of this side-radiation should be assessed. Also this assumes that the radiated acoustic waveforms travel upon straight paths. In a medium where the sound speed varies with depth, as will be the case in near surface bubble clouds, refraction of these paths will take place [50]. However due to the proximity of the source and receiver such refraction is unlikely to be significant.

2.3.2 Free field conditions

The assumption that the bubble oscillates in a free field is currently the topic of considerable discussion [53 59] in the field of bubble acoustics. When radiating into non-free field conditions many of the characteristics of the bubble will change, for example its resonant frequency [51] or damping constants [52]. Typically this assumption can be contravened either by proximity to a surface or by interaction with neighbouring bubbles. In oceanic conditions bubbles are likely to be multiple wavelengths away from any adjacent surfaces, be they the sea bed or the sea surface, and are much more likely to be affected by interaction with neighbouring bubbles. This is particularly likely to be true in surf-zone environments where high void fractions can be expected.

Even in very simple configurations, fully describing the interactions between bubbles is a difficult problem [60, 61]. In the highly complicated, real conditions that oceanic inverse measurements are likely to be taken under (where the bubbles are moving relative to each other in unknown geometries

at unknown rates) incorporating the precise effect of interactions in the inverse solution is likely to be an intractable problem. As such this section will review the existing literature and attempt identify a means by which the magnitude of the effect could be estimated rather than attempt to account for such interactions in the inversion itself.

Initial review of the available literature reveals that while considerable effort has been expended in understanding the magnitude of the forces between the bubbles, for example [59,60], less work exists on quantifying the affect of these interactions on acoustic propagation. Most investigators overcome the problems associated with the precise geometry of the bubble cloud by considering average quantities and their influence upon the effective wavenumber in the medium.

The effective medium approach uses the same basic premise originally outlined by Foldy [13,14] upon which the models already outlined are based: that the bubbly medium can be considered to be a homogeneous medium with uniform acoustic properties. While models using this premise have traditionally assumed bubble interactions to be negligible, recent work by several investigators has begun to propose corrections to the effective medium equations that incorporate higher orders of multiple scattering.

A recent paper by Kargl [62] builds on the recent work of other investigators [63,64] and describes an alternative expression of the complex wavenumber (equation 2.2). This new expression corrects for multiple scattering by using damping constants that relate to the effective medium rather than to the bubbles themselves. The proposed expression is

$$k_e^2 = k_w^2 + 4\pi\omega^2 \int_0^\infty \frac{R_0 n(R_0)}{\omega_0^2 - \omega^2 + \mathrm{j}(\beta_{ve} + \beta_{te} + \beta_{re})} \mathrm{d}R_0 \qquad (2.39)$$

where k_e is the new effective wavenumber, β_{ve} represents the effective viscous damping, β_{te}, the effective thermal damping and β_{re}, the effective acoustic radiation damping. Comparison with equation 2.2 shows that a 2ω term is missing from the damping, but this is simply factorised into the terms themselves. Of these three damping terms only the radiation losses are likely

to be significantly affected by the multiple interactions. Hence $\beta_{ve} \approx \beta_{vis}$ and $\beta_{te} \approx \beta_{th}$. The acoustic radiation damping is a function of the wavenumber and can be determined iteratively

$$\beta_{re} = \omega^2 k_e R_0 \tag{2.40}$$

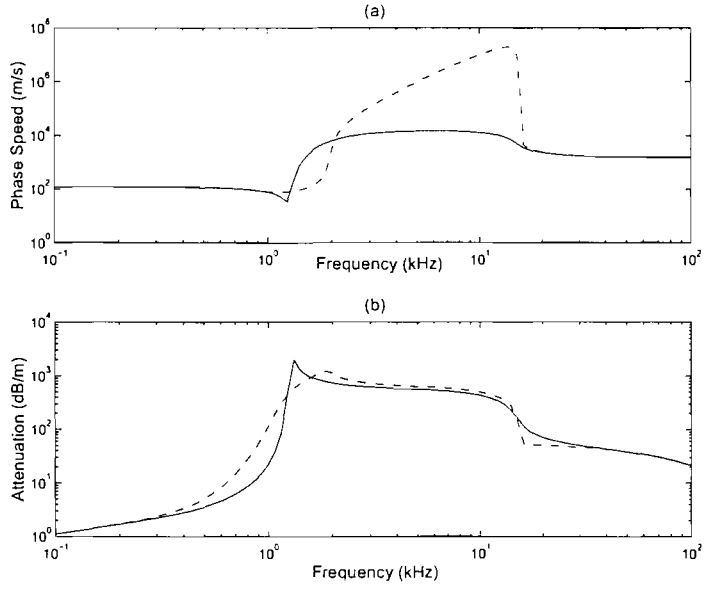

Figure 2.20: Comparison of standard linear theory (solid) and the modified theory accounting for bubble interactions (dashed) for a mono-disperse bubble population with $R_0 = 2.68$mm and $V_F = 0.01$. (a) Phase speed (b) Attenuation.

Comparison of the acoustic propagation characteristics calculated using the linear formulation of Commander & Prosperetti (equation 2.2) and the new formulation for a mono-disperse population shows significant differences, especially in the phase speed (figure 2.20). However comparison of the two expressions for a realistic multi-disperse population for example the oceanic population measured by Phelps & Leighton [45], shows small differences when scaled to a higher void fraction that might be expected in the surf-zone (figure 2.21). The fact that interaction effects are most severe in the mono-disperse

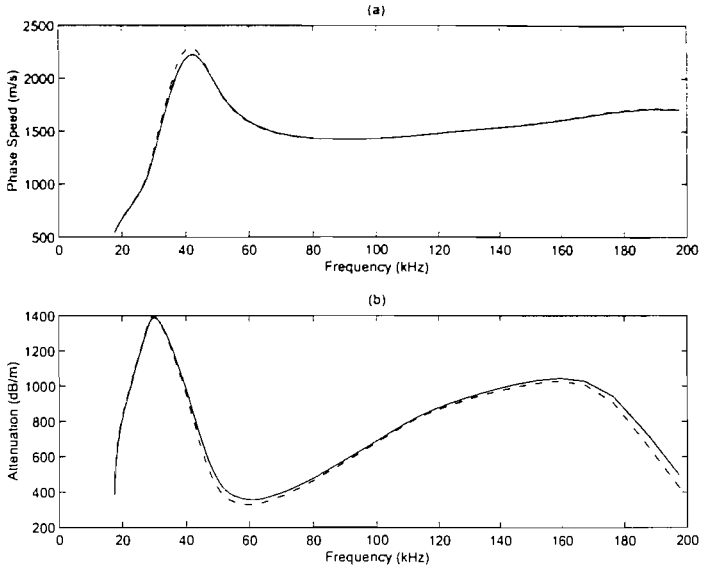

Figure 2.21: Comparison of phase speed and attenuation calculated using standard linear theory (solid) and the modified theory accounting for bubble interactions (dashed) for an oceanic bubble population scaled to a void fraction of 10^{-3} (a) Phase Speed (b) Attenuation.

case is physically reasonable. Interactions when all the bubbles are of the same radius can be expected to be significant because the coupling between the bubbles will be greatest when they share the same resonant frequency. However, in the case where the void fraction is composed of a broad spectrum of bubble radii there are correspondingly fewer bubbles at any one radii and hence the effect of interactions will be smaller. Use of equation 2.39 requires knowledge of the bubble population and hence cannot be included in the inverse method laid out in section 2.2. Instead it will be used to assess the magnitude of the effect of bubble interactions by solving the forward problem using measured populations as the input (see chapter 6).

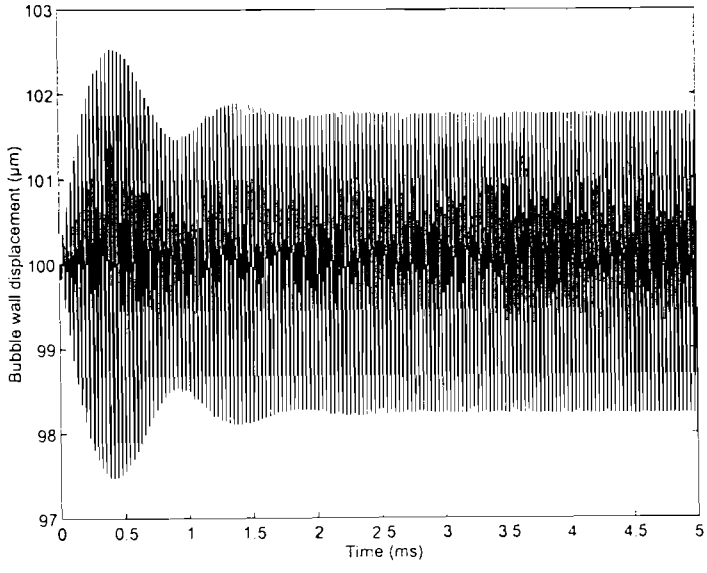

Figure 2.22: Numerical calculation of radial displacement using Herring-Keller formulation for a 100 μm bubble insonified at 500 Pa close to resonance. Notice the bubble response appears monochromatic for $t > 2$ ms.

2.3.3 Monochromatic bubble oscillations

The final assumption inherent in the wavenumber formulation is that of monochromatic (i.e. single frequency) bubble oscillations. In order to achieve such oscillations it is necessary for the bubble to be driven for a long period of time. This is in order that the transient effects caused by the response of the bubble to the broadband nature of the driving signal close to its onset make no contribution to the bubble response. This transient effect is often called the '*ring-up*' period of the bubble and is illustrated in figure 2.22.

Driving the bubble for a long period of time is impractical as this would contradict the plane wave assumptions owing to the arrival of multi-paths. However a monochromatic response could be approximated by assuming that the transient effect can be neglected after a certain period. For example visual inspection of figure 2.22 shows that the initial transient effects have become small after approximately 2 ms leaving a close approximation to a

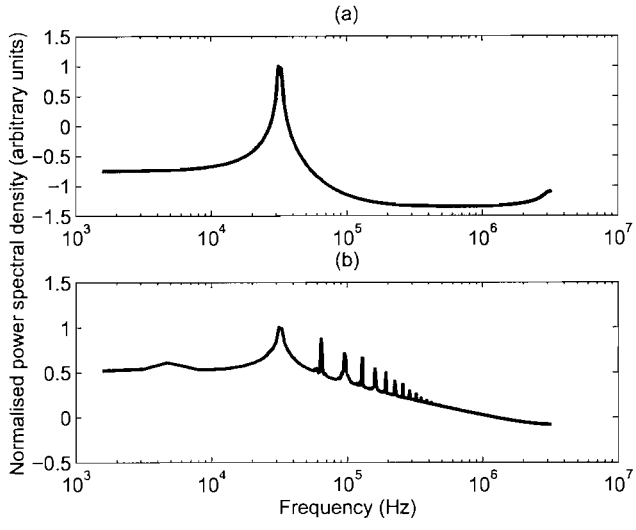

Figure 2.23: The normalised power spectral density of a bubble of radius 115 μm driven by a semi-infinite wave close to its resonant frequency at (a) 100 Pa and (b) 50 kPa. Higher harmonics are excited when the bubble is driven with a high pressure amplitude. The effect of these higher harmonics is ignored in the linear theory.

monochromatic bubble response. However measurements of oceanic bubble populations must be within the top 10 metres of the ocean since this is the greatest depth to which bubbles are known to penetrate [11] and often the region of interest is the top 1-2 metres of the ocean where the higher void fractions can be found. This precludes the use of long pulses owing to the arrival of the first multi-path as discussed in section 2.3.1. Indeed for measurements in the top 2 metres of the ocean with a receiver 2 metres away the duration of the pulse must be less than 1.6 ms. Therefore a limitation of 1.6 ms on the driving pulse would mean that bubbles of size greater than approximately 100 μm^2 could not be driven sufficiently long to ensure a monochromatic response.

Also worthy of consideration is the effect of high amplitude excitation on

[2]Since the duration of the pulse required to drive a resonant bubble to a steady-state increases with the bubble's radius.

Also worthy of consideration is the effect of high amplitude excitation on the response of the bubble. In the surf zones, where high driving pressures are required, a portion of the bubble cloud will be exposed to high driving pressures, potentially causing a nonlinear response in the behaviour of the bubble. Figure 2.23 shows the normalised power spectral density of a bubble of radius 115 μm driven by a semi-infinite wave close to its resonant frequency at 100 Pa and at 50 kPa. As can be seen in the high amplitude case a number of high harmonics of the bubble's natural frequency are excited. The effect of these harmonics is not taken into account in the existing linear theory.

In order to correctly model the response of the bubbles to short pulses of high amplitude, a requirement especially likely in the surf-zone, an advance in the existing theory is required in order to predict the propagation characteristics of time-dependent bubble clouds to high amplitude excitation. Such a model would be of interest, not only in an oceanographic context, but also in other fields for example biomedical ultrasound.

2.4 Summary

This chapter has formulated a method of predicting the effect on acoustic propagation of a known bubble population which compares well with the results of similar techniques already published for synthetic data. The technique was then used with measurements of oceanic bubble populations made by previous investigators to predict the propagation characteristics which are likely to be found in an oceanic environment. This showed that attenuations in excess of 100 dB/m might be expected in the surf-zone. The problem of inversely determining a bubble population from measurements made of acoustic propagation characteristics was then investigated. This was shown to be ill-conditioned and hence required consideration of optimal methods of estimating the population. A solution was developed which involved the systematic determination of an optimal regularisation parameter. This technique was used to reconstruct both synthetic and oceanic populations from

the propagation characteristics predicted by the forward problem. The accuracy of these estimations was found to degrade when Gaussian noise of greater than a few percent was added to the input parameters but it was also shown how the size of the radius bins used improved the conditioning of the matrix and hence the accuracy of the solution.

Having developed a technique capable of estimating bubble populations, the validity of the model used was considered for the case of measurements in the surf-zone. Each of the key assumptions used in the model was examined. It was found that the time taken for larger bubbles to ring-up to a steady-state response is greater than the arrival time of the first, indirect acoustic path. This creates a contradiction between the assumptions of monochromatic bubble response and plane wave excitation. It was also shown how under the high driving pressures necessary in the surf-zone the nonlinear response of the bubble contravenes the assumption of monochromaticity. This demonstrated a need for an advance in the existing theory in order to predict the acoustic propagation characteristics through a nonlinear time-dependent cloud of bubbles. Such a model will be the subject of the next chapter.

Chapter 3

Development of a nonlinear, time-dependent model of acoustic propagation in bubbly liquids

Chapter 2 outlined the need for a model of acoustic propagation in bubbly liquids that does not include the assumptions of linearity, monochromaticity and steady-state that are inherent in the current theory [18]. Such a model will be of use when high driving pressures are incident on the bubble population being measured, causing a nonlinear response or when the excitation is sufficiently short that not all the bubbles are oscillating in steady state. This chapter will derive the model and discuss its application to the problem of inversion of acoustic propagation characteristics. As this thesis is primarily concerned with oceanic bubble populations, it will be assumed that the bubbles referred to are air bubbles trapped in water. However the theory could equally be applied to any similar gas-liquid combination.

3.1 Model of acoustic propagation through a cloud of nonlinearly responding bubbles

The material in this section was developed in collaboration with Prof. T. G. Leighton. The text follows that of reference [65].

The initial approach taken to derive a model of acoustic propagation through a cloud of nonlinearly responding bubbles is analogous to that attempted by previous investigators [5, 22] (see chapter 1), namely to derive an expression for the complex sound speed in the medium. This approach, as will be shown below, is flawed in the nonlinear regime. However the reasons for this are illuminating, and their appreciation highlights potential sources of error in existing models, as well suggesting an alternative approach. Therefore the derivation of the complex sound speed is presented here in full, and forms the first section of this chapter [65].

Assume throughout that each bubble radius is much smaller than the acoustic wavelength. A cloud of bubbly water, having volume V_c and bulk modulus B_c, is made up of a volume V_w of bubble-free water (having sound speed c_w and bulk modulus B_w) and a volume V_g of free gas (having sound speed c_g and bulk modulus B_g) distributed in a population of bubbles. Hence

$$V_c = V_w + V_g \tag{3.1}$$

Mass conservation is simply expressed by multiplication of the volumes with the respective densities (of the cloud, ρ_c, bubble-free water, ρ_w and gas, ρ_g), i.e.

$$\rho_c V_c = \rho_w V_w + \rho_g V_g \tag{3.2}$$

Under the assumption that each of the three media separately conserve mass, the differential of equation 3.2 with respect to the applied pressure P is, of course, zero. In a infinite body of either water or gas *that contains no dissipation*, sound speeds (c_w and c_g respectively) may be defined:

$$c_\varepsilon^2 = \frac{B_\varepsilon}{\rho_\varepsilon} = \left[\frac{\partial P(\rho, S)}{\partial \rho}\right]_\varepsilon \qquad (\varepsilon = w, g) \tag{3.3}$$

where S is the entropy and the subscript ε can refer to application to water (w) or gas (g). Similarly, differentiation of equation 3.1 with respect to the applied pressure gives, with equation 3.3, the relationship between the bulk moduli [1]

$$\frac{1}{B_c} = \frac{V_w}{V_c}\frac{1}{B_w} + \frac{V_g}{V_c}\frac{1}{B_g} \tag{3.4}$$

Let us define a function ξ_c equal to the root of the ratio of the bulk modulus of the bubbly cloud to its density:

$$\xi_c = \sqrt{\frac{B_c}{\rho_c}} = \sqrt{\left(\frac{V_c}{\rho_w V_w + \rho_g V_g}\right) \Big/ \left(\frac{V_w}{V_c B_w} + \frac{V_g}{V_c B_g}\right)} \approx c_w \left(1 + \frac{B_w V_g(t)}{V_c B_g(t)}\right)^{-\frac{1}{2}} \tag{3.5}$$

where the final approximation is valid assuming the void fraction is not extremely high. Specifically it is assumed that the density and volume of the cloud are approximately equal to those of its bubble-free water component. If the bubbly cloud were not dissipative, then this would equal the sound speed in the cloud, but (as will be shown), such an identity is not rigorous in lossy bubble clouds.

Evaluation of equation 3.5 requires calculation of the bulk modulus of the gas, as it is distributed through a (presumably) numerous population of bubbles pulsating with a broad range of amplitudes, phases, frequency content, damping and start times. The inhomogeneous bubbly water must be divided into volume elements which are sufficiently small to ensure that all the bubbles in that element are subjected to the same pressure change $dP(t)$ simultaneously. This would allow calculation of a value for ξ_c for each volume element, since from equation 3.3 the bulk modulus B_{g_l} of the gas

[1] It should be noted that this expression is the same as that given by Terrill & Melville [20] in terms of the relationships of compressibilities, K and void fraction, $V_F K_c = V_F K_g + (1 - V_F) K_w$.

within the l^{th} element is related to the volume changes $\mathrm{d}V_i$ of the I bubbles in that volume element:

$$\frac{1}{B_{g_l}} = -\frac{1}{V_{g_l}} \sum_{i=1}^{I} \frac{\mathrm{d}V_i}{\mathrm{d}P_l} \tag{3.6}$$

where P_l denotes the pressure in the l^{th} volume element. Consider one such volume element V_{c_l} of a cloud which has total volume

$$V_c = \sum_{l=1}^{L} V_{c_l} \tag{3.7}$$

Substituting equation 3.6 into equation 3.5 gives ξ_{c_l}, the time history of ξ_c within the volume element V_{c_l}

$$\xi_{c_l} \simeq c_w \left(1 - \frac{\rho_w c_w^2}{V_{c_l}} \sum_{i=1}^{I} \frac{\mathrm{d}V_i}{\mathrm{d}P_l} \right)^{-1/2} \tag{3.8}$$

To evaluate equation 3.8, the bubble population of the volume element is classified into j discrete bins according to bubble size (as previously described). Every individual bubble in the j^{th} bin is replaced by another bubble which oscillates with radius $R_j(t)$ and volume $V_j(t)$ (about equilibrium values of R_{0_j} and V_{0_j}), such that the total number of bubbles N_j and total volume gas $N_j V_j(t)$ in the bin remain unchanged by the replacement. If the bin width increment is sufficiently small (1 μm is normally chosen), the time history of every bubble in that bin should closely resemble $V_j(t) = V(R_{0_j}, t)$ (the sensitivity being greatest around resonance). Hence the total volume of gas in the l^{th} volume element of bubbly water is

$$V_{g_l}(t) = \sum_{j=1}^{J} N_j(R_{0_j}, t) V_j(t) = V_{c_l} \sum_{j=1}^{J} n_j(R_{0_j}, t) V_j(t) \tag{3.9}$$

Here $n_j(R_{0_j}, t) = N_j(R_{0_j}, t)/V_{c_l}$ is the number of bubbles per unit volume of bubbly water within the j^{th} bin. It will vary more slowly than the acoustically driven pulsation $V_j(t)$, and so the approximation is made that it is stationary over the duration of the measurement. This in practice can be in

the range 0.001-1 s: smaller volume elements and more dynamic oceans would sensibly suggest finer time resolution. Expressing equation 3.8 in terms of this bin scheme gives [65]

$$\xi_{c_l} = c_w \left(1 - \rho_w c_w^2 \sum_{j=1}^{J} n_j(R_{0_j}) \frac{\mathrm{d}V_j(t)}{\mathrm{d}P_l(t)} \right)^{-1/2} \tag{3.10}$$

This form is suitable for numerical solution and is not limited by small amplitude, steady state, monochromatic or linear assumptions. Also note that the bubbles have not been assumed to be spherically symmetric. The multi-layer aspect of this model can be incorporated into the forward problem described in chapter 2 by dividing the medium into l layers, as described above, assigning a bubble population to each layer (the entirety of the cloud can either be considered homogeneous or inhomogeneous). The forward problem is then solved for each layer of the cloud in turn, using the propagation characteristics calculated in the previous layer to determine the appropriate driving pressure for the subsequent layer. In this manner the propagation undertaken by a plane wave traveling through such a medium can be calculated.

3.1.1 Linear expansion

A first order check upon equation 3.10 is that when low amplitude, linear constraints are imposed the solution reduces to that of Commander & Prosperetti [22]. While this will not expose any inaccuracies in the nonlinear aspect of the model (since these will be set to zero in by the process of linearisation) it will add some validity to the expression. Assuming that the bubble wall oscillations are of small amplitude then

$$\frac{dV}{V_0} = \left(1 + \left(\frac{dR}{R_0}\right)\right)^3 - 1 = 3\left(\frac{dR}{R_0}\right) + 3\left(\frac{dR}{R_0}\right)^2 + \left(\frac{dR}{R_0}\right)^3 \tag{3.11}$$

(assumes spherical symmetry)

Truncating after the first term in the expansion is a valid linear assumption, and with this $dV/dP = 4\pi R_0^2(dR/dP)$. Substitution of this limitation into equation 3.10 when the bubble population is re-expressed as a continuous integral gives:

$$\begin{aligned} \frac{c_w^2}{\xi_c^2} &\simeq 1 - \rho_w c_w^2 \int_0^\infty n \frac{dV}{dP} dR_0 \\ &\approx 1 - 4\pi\rho_w c_w^2 \int_0^\infty n R_0^2 \frac{dR}{dP} dR_0 \end{aligned} \tag{3.12}$$

where the subscript l has been dropped because the bubble cloud is considered to be homogeneous. If it is further assumed that the linear bubble pulsations are the steady state and monochromatic response to a constant-amplitude (P_A) monochromatic driving field of the form $P(t) = P_A \sin(\omega t)$, then from equation 1.27

$$\frac{dR}{dP} = \frac{-1}{R_0\rho_w((\omega_0^2 - \omega^2) + \mathrm{j}2\beta_{tot}\omega)} \tag{3.13}$$

(assumes linear steady state (monochromatic) spherical pulsations in response to monochromatic driving sound field)

where β_{tot} is the frame-independent damping constant having dimensions of time^{-1}, derived assuming monochromatic conditions, which accounts for the bubble damping by viscous, thermal and acoustic radiation mechanisms (see section 1.2.4).

Substitution of 3.13 into 3.12, and multiplication by the square of the angular frequency ω gives the complex wavenumber k_c within the bubbly medium, as derived by Commander & Prosperetti [22]

$$k_c^2 = \left(\frac{\omega}{c_w}\right)^2 + 4\pi\omega^2 \int_0^\infty \frac{R_0 n}{(\omega_0^2 - \omega^2) + \mathrm{j}2\beta_{tot}\omega} dR_0 \tag{3.14}$$

3.1.2 Discussion

Equation 3.10 is related to the sound speed in the medium. Indeed in the linear, lossless case ξ_{c_l} does indeed equal c_{c_l}, the sound speed within the l^{th} element of the cloud. In order to understand the reasoning behind this, consider a plot of pressure versus volume for an undamped bubble oscillating linearly within a driving pressure field. Because the bubble is linear and undamped during its expansion phase it will travel upon a line of constant gradient ($\mathrm{d}V_i/\mathrm{d}P_l$). Similarly, because the system is lossless, during its contraction phase it will traverse back along exactly the same line. Therefore over many pulsations the bubble will map out a straight line within the pressure-volume plane. This means that the sound speed calculated using equation 3.8 does not fluctuate within one cycle of the bubble response: the gradient of that line can be used to correctly determine the sound speed in the medium.

Next, consider a nonlinear but lossless bubble response. In this case the pressure-volume plot will be a curve between two points corresponding to the minimum and maximum excursion of the bubble wall. The path taken between these points will be the same during both the expansion and the contraction phase. The exact route of the path will depend upon the nonlinear dynamics of the driven bubble. However, the fact that the gradient of the curve is no longer constant within one bubble cycle means that the speed that the wave propagates at in the medium will vary within the cycle. Hence the propagation is nonlinear making the concept of a single sound speed in the medium invalid.

Finally, consider a nonlinear bubble that loses energy through various damping mechanisms such as viscous and thermal dissipation. Here the path mapped out between the maximum and minimum excursion points will be different during the expansion and contraction phases owing to the effect of damping on the system. This will result in two curves that no longer overlay each other, and hence it will map out a loop over a given cycle of bubble oscillation. A similar argument to that presented above means that

the concept of sound speed in such a medium is no longer valid.

However, the sound speed in nonlinear, dissipative media may be approximated by considering derivative term in equation 3.10 to be the best straight line fit connecting the two extremities of the loop, which can be thought of as the 'spine' of the loop. For systems with low dissipation, away from resonance this is a valid assumption. If we assume that this is the case we can equate the nonlinear propagation factor ξ_c with the sound speed c_c in the bubbly medium.

As discussed in chapter 4, measurements of phase speed (as opposed to group speed) are experimentally difficult to achieve, and the inversion techniques described so far have been based upon attenuation. Therefore it is desirable to investigate whether the attenuation experienced by the wave propagating in the bubbly medium can be inferred from equation 3.10. As discussed in chapter 2, the attenuation is related to the imaginary part of the complex speed of sound. This imaginary part can be recovered from equation 3.10 (which is purely real) by use of the Hilbert transform.

The Hilbert transform [66] is a signal processing technique that exploits *de Moivre's* theorem to calculate the imaginary part of a complex number from the real part. The imaginary part of the complex number is formed by adding a 90° phase shift to the real data, hence converting cosines to sines and visa versa.

Figure 3.1 shows the real and imaginary parts of ξ (calculated making use of the Hilbert transform) for a 71 μm bubble driven by a semi-infinite pulse at a frequency of 35.1 kHz and an amplitude of 7.95 kPa. Note the transient period at the onset of the driving signal caused by the impulse response of the bubble. This transient behaviour settles down to steady state oscillation approximately 200 μs after the onset of the driving pressure. The period required for the bubble to achieve steady state will vary as a function of bubble radius, frequency and the driving pressure.

The approached used by Commander & Prosperetti [22] is to use the complex sound speed ($c_c = u - jv$) to describe the pressure field resulting

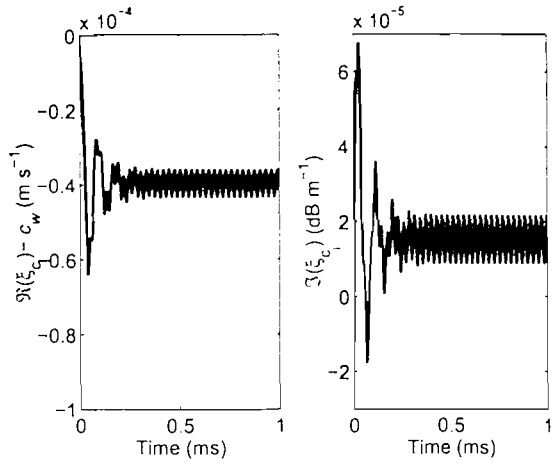

Figure 3.1: (a) $(\Re(\xi_{c_l}) - c_w)$ and (b) $\Im(\xi_{c_l})$, based respectively on the real and imaginary parts of equation 3.10 as constructed through use of a Hilbert transform for a single 71 μm bubble insonified by a 35.1 kHz semi-infinite pulse starting at t=0 with an amplitude of 7.95 kPa. There is an unstable period lasting approximately 200 μs caused by the transient response of the bubble before a steady state oscillation is achieved.

from a plane wave propagating in the $+x$ direction. The formulation is expressed in the form of a complex wavenumber ($k_c = \omega/c_c$)

$$P(x,t) \propto \mathrm{e}^{\mathrm{j}(\omega t - k_c x)} = \mathrm{e}^{\mathrm{j}\left(\omega t - \frac{\omega}{c_w} x\right)} \mathrm{e}^{-\frac{\omega v}{c_w} x} \tag{3.15}$$

From this phase speed and attenuation can be calculated as described in equations 2.12 and 2.13. However in the nonlinear case this complex representation is no longer valid. Consider a harmonic pressure field described in real notation as follows

$$P = P_A \cos \omega t \tag{3.16}$$

or in complex notation as

$$P = \Re\left\{P_A \mathrm{e}^{\mathrm{j}\omega t}\right\} \tag{3.17}$$

If a bubble with equilibrium volume V_0 has a nonlinear dependence on that pressure field then

$$V = V_0 + aP + bP^2 + cP^3 + \ldots \tag{3.18}$$

Now let us consider the quadratic component of that response, in real notation we have

$$V_{2\omega}(t) = bP^2 = bP_A^2 \cos^2 \omega t = \frac{bP_A^2}{2}(1 + \cos 2\omega t) \tag{3.19}$$

whereas the complex notation gives

$$V_{2\omega}(t) = \Re\left\{bP_A^2 e^{2j\omega t}\right\} = bP_A^2 \cos 2\omega t \tag{3.20}$$

As can be seen by comparing equations 3.19 and 3.20 the complex notation does not have the DC component included in the real formulation. The third harmonic component exacerbates the problem introducing a missing cosine term

$$V_{3\omega}(t) = cP^3 = cP_A^3 \cos^3 \omega t = \frac{cP_A^3}{4}(\cos 3\omega t + 3\cos \omega t) \tag{3.21}$$

$$V_{3\omega}(t) = \Re\left\{cP_A^3 e^{3j\omega t}\right\} = cP_A^3 \cos 3\omega t \tag{3.22}$$

The reason for these difference is that nonlinear systems transfer energy between frequency components, a fact that the complex representation fails to take into account. In the linear case these effects will not be seen since $b, c, \ldots \to 0$. However the extent to which this affects any solution in the nonlinear regime will increase with amplitude.

As has been seen two features of propagation through bubbly liquids make application of equation 3.10 incorrect, and both of these require invalid assumptions to be made in order to apply that equation in the nonlinear regime. The first feature, as discussed above, is that the transference of energy between frequencies in the nonlinear regime introduces errors into the complex sound speed representation proposed by Commander and Prosperetti [22].

The second effect, also discussed above, is that finite dissipation means that the locus of points in the pressure-volume plane map out a finite area over the oscillatory cycle. However it is this very feature which provides the solution by which the measured propagation characteristics can be inverted to obtain the size distribution of bubbles that are behaving nonlinearly.

3.2 Formulation of the nonlinear extinction cross section

The material in this section was developed in collaboration with Profs. T. G. Leighton & C. L. Morfey. The text follows that of reference [65].

As stated in chapter 1 the extinction cross section is defined as the ratio of the time averaged power subtracted from an incident plane wave due to the presence of a bubble, to the intensity of the incident acoustic beam [5].

$$\Omega_b^{ext} = \frac{< W >}{I} \tag{3.23}$$

The power subtracted from the acoustic beam by the presence of the bubble can be established by consideration of the thermodynamic properties of the system. Consider a plot of the volume of a (perfect) gas against applied pressure for a bubble driven by a semi-infinite pulse. The plot initially consists of a single point while the bubble is at rest. With the application of a driving pressure the bubble begins to respond and the plot begins to map out loops, the precise path of these loops depends upon the dynamics of the bubble. To begin with these loops may well be erratic owing to the initial transient response of the bubble. However the bubble will eventually settle into a steady state oscillation, whereupon the locus will repeatedly map out the same loop. This can be more formally described by consideration of the 1st Law of Thermodynamics which describes the relationship between the internal energy, U, of a gas and the heat and work transfer to and from that gas.

$$dU = \bar{d}Q + \bar{d}w = \bar{d}Q - PdV \tag{3.24}$$

where both the incremental heat supplied to the bubble, $(\bar{d}Q)$, and the work done on the bubble, $(\bar{d}w)$, are not exact differentials, while dU is. This is because the internal energy of the gas is a property of state, a fact that can be seen by considering that while for a given change in energy, dU, the corresponding points in a pressure-volume plot, U_1 and U_2, are fixed, the path taken between these points can vary.

Equation 3.24 requires careful consideration to determine whether the pressure used to calculate the work done by the acoustic field on the bubble should be the acoustic pressure applied to the bubble or the internal pressure within the bubble. This can be seen by considering the form of the bubble dynamics equation. All bubble dynamics equations (such as the Rayleigh-Plesset or the Herring-Keller equations described in chapter 1) can be considered to express the equality between the pressure difference, Δp, that is uniform across the entire bubble wall and a summation of other terms. These terms are p_i (the pressure within the bubble due to the gas, (p_g) and vapour, (p_v), pressures), p_σ, the pressure due to surface tension and p_{dyn} a collection of terms resulting from the motion of the liquid when the bubble wall is displaced. The signs of the various terms in equation 3.25 can be deduced from consideration of the balance of pressures across the bubble wall.

$$\Delta p = p_i - p_\sigma - p_{dyn} \tag{3.25}$$

Considering each term in equation 3.25 it can be seen that the work done on the bubble and hence the energy subtracted from the sound field per cycle of the insonifying pulse is

$$E_{loop} = -\oint p_i dV + \oint p_{dyn} dV + \oint p_\sigma dV \tag{3.26}$$

Equation 3.26 can be simplified by noting that Δp equals the spatial average over the bubble wall of the blocked pressure $\left\langle p_{blocked} \right\rangle$ (the pressure

seen if the bubble was replaced by a rigid sphere of equal radius). In the long wavelength limit the blocked pressure equals the applied acoustic pressure $P(t)$ that would be present at the bubble centre were the bubble not present. The equation can therefore be re-written to show that the area mapped in a loop of in the pressure-volume plane is the energy subtracted from the acoustic wave in the time interval corresponding to that loop:

$$E_{loop} = -\oint \Delta p \mathrm{d}V = -\oint \left\langle p_{blocked} \right\rangle \mathrm{d}V \approx -\oint P \mathrm{d}V \qquad (kR \ll 1) \quad (3.27)$$

Therefore the rate at which the acoustic field does work on the bubble can be found by integrating the area in the pressure-volume plane enclosed by the loops formed by the intersections described above, and dividing energy so obtained by the time interval taken to map out that loop T_{loop}. This, in theory, allows calculation of the rate of work done by the acoustic field on the bubble irrespective of the state of the bubble response. In practice the integration will be more problematic close to the onset of the driving field due to the initial response of the bubble and precise loops may be difficult to define. However once steady state is achieved a well defined loop can easily be found. Figure 3.2 illustrates this by showing the P-V loop for a 100 μm bubble driven at 38 kHz.

The rate of work done on the bubble by the acoustic field can be used with equation 3.23 to calculate the extinction cross section presented by that bubble. Assuming that the bubble is driven by plane wave oscillation the acoustic intensity, I, of the incident pressure is given by [67]

$$I = \frac{P_A^2}{\rho_w c_w} \qquad (3.28)$$

where P_A is the amplitude of the incident pressure wave. By combining equations 3.23, 3.27 and 3.28 the extinction cross section can be expressed as

$$\Omega_b^{ext} = \frac{< W >}{I} = \frac{E_{loop}/T_{loop}}{P_A^2/\rho_w c_w} = -\frac{\rho_w c_w \oint P \mathrm{d}V}{P_A^2 T_{loop}} \qquad (kR \ll 1) \qquad (3.29)$$

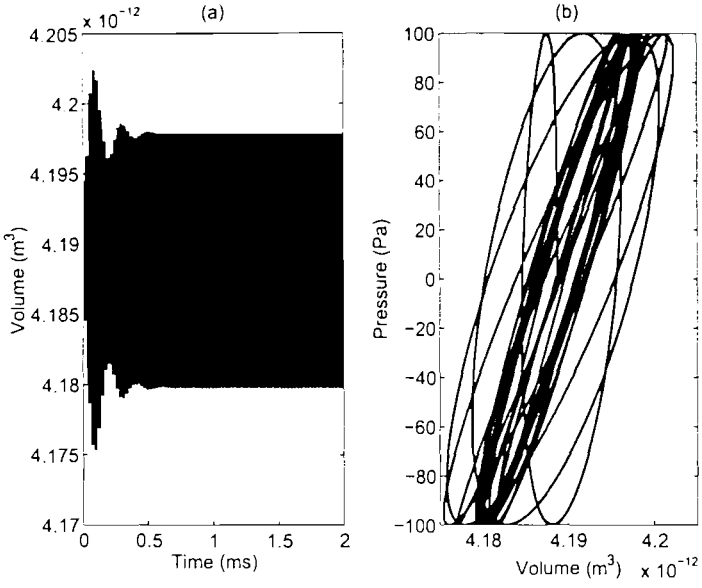

Figure 3.2: A 100 μm bubble driven by a semi-infinite pulse at 38 kHz with a pressure amplitude of 100 Pa (a) Volume vs time, the bubble initial responds at its natural frequency before adopting a steady state (b) Pressure vs volume, the locus consists of a single point until the onset of the driving pressure whereupon it describes erratic loops before settling into a steady state as seen by the dense section of the curve where to locus repeatedly describes the same path.

Attenuation can now be calculated from the calculated extinction cross section using the same method as shown in chapter 1 (equations 1.3 to 1.5) i.e. attenuation (in dB/m) is given by

$$A = 10\Omega_c^{ext} log_{10} e \approx 4.3429\Omega_c^{ext} \tag{3.30}$$

This formulation therefore presents the theory upon which an inversion could be based which so far has made no assumptions of linearity, steady state or monochromaticity. The remainder of this chapter will implement this theory and discuss its implications and how its use can improve our understanding of some fundamental properties of propagation in bubbly media.

3.3 Numerical calculation of nonlinear extinction cross section

The numerical code (and supporting theory) for solution of the bubble dynamics equation referred to in this section was developed by Mr. H. A. Dumbrell and Prof. T. G. Leighton.

In order to calculate a nonlinear, time dependent extinction cross section it is necessary to model the response of the bubble to a driving pressure (in order to obtain a volume-pressure map). There are a number of models that are suitable for this, but it is important to choose a model that does not impose assumptions that may be violated during the measurement process. This is because any solution will, at best, only be as accurate as the model used to obtain it. The model used in the work is the Herring-Keller equation, a form of which is given by Keller and Miksis [33]. This model is discussed in chapter 1. At low amplitude the model produces the same results as the existing linear theory but is also capable of modelling high amplitude, nonlinear behaviour. It has the advantage of assuming a finite, time invariant sound speed in the liquid and hence is able to model radiation damping. Dumbrell and Leighton [23] have incorporated thermal damping into the solution of the Herring-Keller equation by applying the perfect gas law to the spatially averaged pressure in the bubble as proposed by Nigmatulin *et al.* [34], Prosperetti *et al.* [35] and Prosperetti and Hao [36]. Because of these features, this model was judged to impose the fewest restrictions upon the solution, and hence will be used in the following sections to calculate the nonlinear extinction cross section.

M-files for MATLAB^{TM} which solve the Herring-Keller equation [33] using the technique of separation of variables were provided by Mr. Hugh Dumbrell of Dstl, UK. In order to illustrate the use of this code figure 3.3 shows the response of a 100 μm air bubble when driven below, close to and above its resonance frequency semi-infinite plane wave with a driving pressure of 10 kPa. The bubble is assumed to be at a depth of 1 m in a fluid with properties

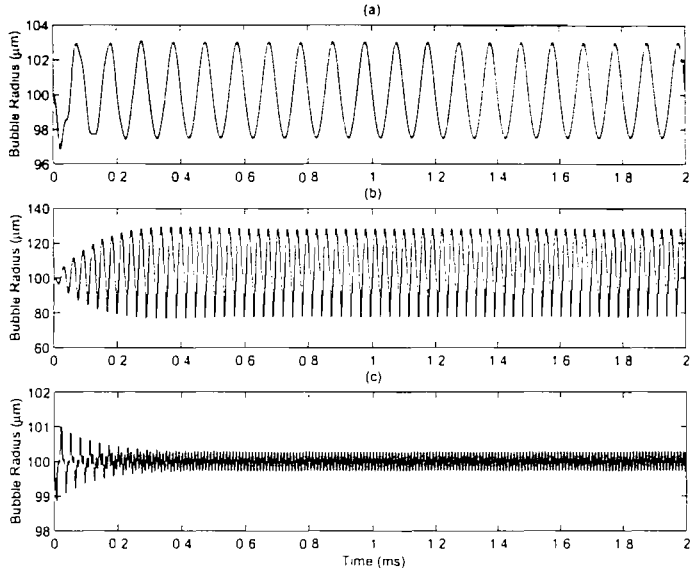

Figure 3.3: Bubble wall radius for a 100 μm bubble driven by a semi-infinite plane wave with a frequency of (a) 10 kHz (below resonance) (b) 32.8 kHz (close to resonance) and (c) 100 kHz (above resonance).

typical of sea water[2].

As can be seen from figure 3.3 the bubble's behaviour varies as a function of the driving frequency. When driven by a semi-infinite pulse the bubble will initially respond at its natural frequency owing to the broadband nature of the pulse close to the discontinuity. As time increases the bandwidth of the driving pulse will narrow, forcing the bubble to respond at the driving frequency and thereby settling into a steady state oscillation. This effect is most noticeable close to and above resonance.

In order to calculate the bubble volume from the radius time history, it is necessary to assume that the bubble is spherically symmetric at all times. Having made this assumption the conversion between radius and volume is trivial ($V = 4\pi R^3/3$). It should be noted that this limitation is due to the fact that the solution of the Herring-Keller equation is expressed in

[2]A surface tension of 7.28×10^{-2} N/m was assumed

terms of bubble radius, and not a limitation of this method of calculating the extinction cross section. Were a model available that directly computed bubble volume, this would enable the extinction cross section to be calculated for higher order oscillations of the bubble wall.

Having ascertained the pressure-volume curve, calculation of the contour integral in equation 3.27 is non-trivial, and an algorithm had to be developed within MATLAB^{TM} in order to accomplish this. The problem is complicated by the fact that equation 3.27 does not necessarily describe a straight-forward loop. It may be the case that the 'loop' contains one or more crossings forming a 'figure-of-eight' shape. In this case the sections of the loop that proceed in an anti-clockwise direction with respect to time were subtracted from those proceeding in a clockwise direction. This was confirmed by the fact that the cross section should, in most cases, be positive [3].

A disadvantage of this new technique is the amount of computation required to form the extinction cross section. The majority of the computation is involved in the numerical solution of the Herring-Keller equation and the calculation of the thermal damping terms. Calculation of the value of the extinction cross section for a single bubble at a single frequency took up to 30 minutes on a 1 GHz Pentuim IV with 512 MB of RAM. For a square K-matrix the computation time is proportional to the square of the number of bubble radius bins and hence the computation time for a single 10 by 10 matrix could be up to 50 hours. In order to make the computation time practical, all the bubble populations in this thesis are henceforth modelled using a single layer. This is not however an inherent limitation of the model, and more powerful computing facilities or more efficient computation algorithms may make multi-layer nonlinear forward models a practical proposition.

[3] While it would seem reasonable that the extinction cross section of a bubble should be positive, it was considered that there *may* be special cases, e.g. bubble-bubble interactions where this may not be the case. Therefore it was not considered sufficiently robust that the modulus of the answer be taken to calculate the extinction cross section.

3.4 Low amplitude nonlinear extinction cross section

As a check upon the validity of the above method of determining the extinction cross section of a bubble a low amplitude nonlinear extinction cross section was compared with an analytical expression of the linear extinction cross section. While this will not expose any errors due to high amplitude effects, it will create a first-order confidence in the technique. Figure 3.4 shows the extinction cross section for a 100 μm bubble driven between 1 and 100 kHz. The cross section is plotted using equation 2.14 and the new nonlinear formulation assuming an amplitude of 100 Pa. As can be seen the two lines are in excellent agreement, overlaying each other almost perfectly with maximum disagreement of less than 1% at resonance which can be attributed to differences in the damping models used.

3.5 High amplitude nonlinear extinction cross section

As a further check upon the validity of the new technique, a high amplitude nonlinear cross section was calculated. Unlike the low amplitude case there is no analytical expression that can be used as an independent check upon the validity of the model. However it is expected that the nonlinear response of the bubble will result in the spread of energy to other frequencies, for example to the second harmonic. It is expected that the resonance frequency of the bubble will shift down slightly due to the different dynamic properties of the bubble. Also the magnitude of the cross section at resonance should be lower than the linear cross section owing to the shift of energy to other frequencies. These qualitative observations will also add a degree of confidence in the validity of the technique.

The high amplitude extinction cross section is shown in figure 3.5. In order to provide a point of reference, it is compared against the same linear

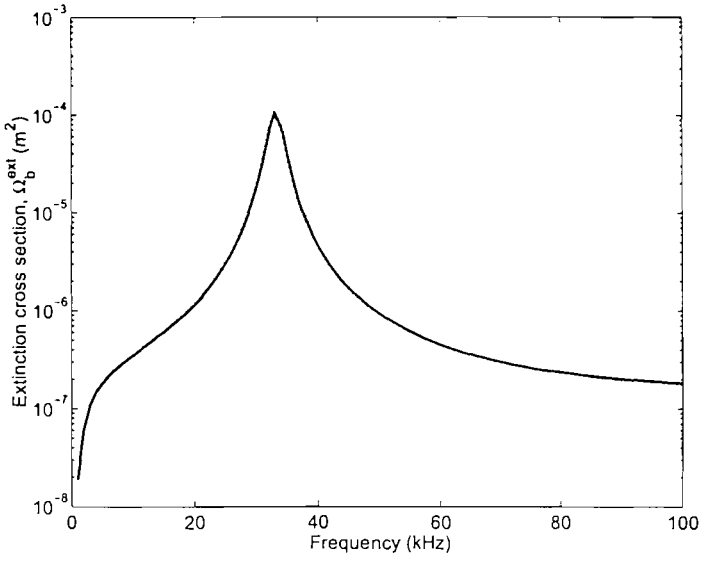

Figure 3.4: The extinction cross section of a 100 μm bubble driven between 1 and 100 kHz. The extinction cross section is calculated using a linear analytical expression (dotted line) and the new nonlinear formulation assuming a zero-to-peak driving pressure of 100 Pa (solid line). As can be seen the two curves overlay each other almost perfectly with any slight discrepancy attributable to differences in the damping values.

cross section as the previous section. The same driving signal is used. However the amplitude of the signal is now increased to 50 kPa. As can be seen from the graph the high amplitude nonlinear cross section does indeed include peaks at frequencies other that the resonance frequency of the bubble. Several subharmonic frequencies are present as well as the expected second harmonic. Also, as expected, the main resonance frequency of the bubble has also shifted down in frequency and is lower in amplitude than the linear cross section.

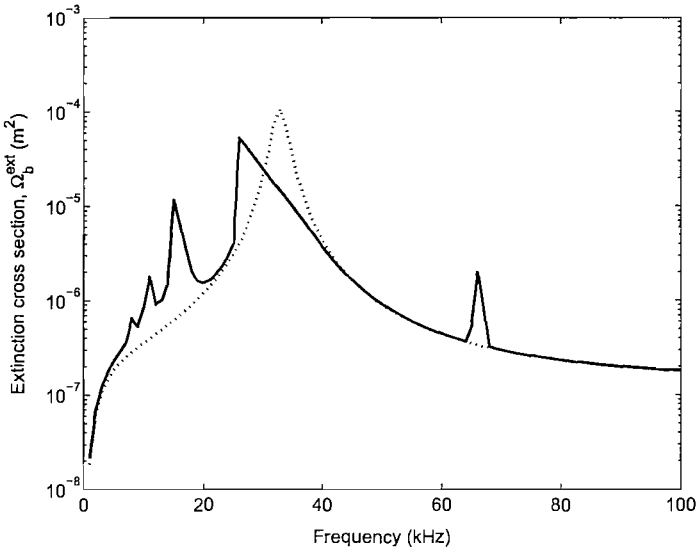

Figure 3.5: The extinction cross section of a 100 μm bubble driven between 1 and 100 kHz. The extinction cross section is calculated (for comparison) using a linear analytical expression (dotted line) and the new nonlinear formulation assuming a zero-to-peak driving pressure of 50 kPa (solid line). The nonlinear cross section contains several subharmonic peaks and also a peak at the second harmonic frequency. Also note that the main resonant peak has shifted down in frequency and is of lower amplitude than the corresponding linear peak.

3.6 Discussion

The plot of applied pressure versus the volume of the bubble contains a number of items of interest that highlight the behaviour of the bubble as well as giving an effective demonstration of the advantages of the use of the Herring-Keller equation [33] when compared to the linear solution given by Commander & Prosperetti [22].

Figure 3.6 shows a range of different responses for a 49 μm bubble excited by a semi-infinite pulse with an amplitude of 7.95 kPa at three different frequencies, above, close to and below resonance. The driving frequency is fixed in each of the three columns in the figure. In the left column, which corresponds to the bubble being driven above resonance, the bubble initially

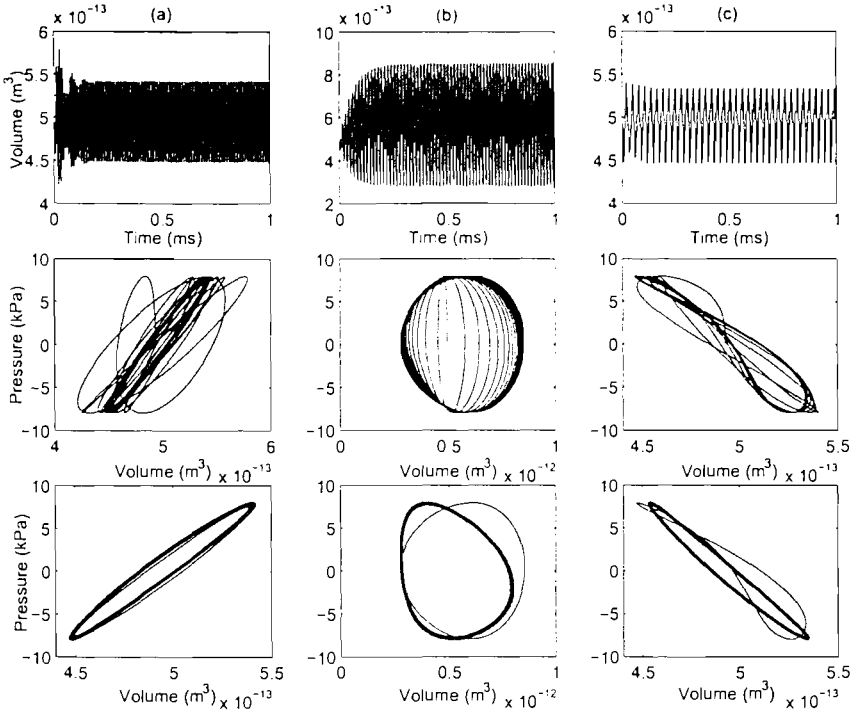

Figure 3.6: Bubble responses for a 45 μm bubble insonified by a semi-infinite pulse starting at t=0 with an amplitude of 7.95 kPa at (a) 84.2 kHz (b) 65.7 kHz and (c) 31.5 kHz. The top graph in each case shows the volume time history calculated using the Herring-Keller equation (with damping after Prosperetti *et al.* 1988). The middle row shows the corresponding pressure-volume curve starting at the onset of the driving pressure. The darker area shows the steady state regime, where the successive loci overlap each other. Nonlinear components will cause crossovers in a loop (a second- or sub-harmonic causing a figure-eight to appear, for example), as shown in figure 4(c), such that the integration of equation 3.27 causes the areas of the clockwise loops to be subtracted from those of the anticlockwise. The bottom row superimposes the steady-state loops of the middle row (thin line) with the corresponding linear solution using the steady-state formulation Commander & Prosperetti (thick line).

responds at its natural frequency before settling down to a steady state (in a similar fashion to that discussed in relation to figure 3.3). The steady state region appears as a constant loop with a thick black line caused by the continual overlapping of the locus. The corresponding pressure-volume plot describes erratic loops that directly relate to this 'ring-up' period. The extinction cross section of the bubble during ring-up could be calculated if a method of approximating the area of these erratic loops was developed. This would be an important development in bubble acoustics and is recommended as an area of future research. The middle column, where the bubble is driven close to resonance, shows a smooth ring-up period which achieves steady state approximately 200 μs after the onset of the driving pressure. The pressure-volume curve prescribes a series of ellipses before achieving a steady state condition that approximates a circle. It should be noted that the volume axis in this plot is a to different order of magnitude $O(10^{-12})$ than those either side of it $O(10^{-13})$. This is because of the larger excursion of the bubble wall and the peak in the extinction cross section at resonance. The final column, with the bubble driven below resonance, exhibits a 'cross-over' in the P-V curve. This cross-over may be caused by the excitation of a harmonic in the response of the bubble.

The bottom row of figure 3.6 is of special interest and shows the steady state portion of the P-V curve for the bubble excited at each of the three frequencies. These are compared to the P-V curve calculated using the linear formulation of Commander & Prosperetti [22] (calculated assuming that the bubble is spherical, $R = R_0(1 + R_\epsilon)$ and using equation 1.27). This comparison is of interest because it compares the new technique to the model used in all current state-of-the-art bubble inversion techniques. It should be noted that Commander & Prosperetti's formulation is a linearization of the same Herring-Keller equation which is used in its full nonlinear form in the new technique. Commander & Prosperetti note in their paper that 'In the presence of resonance effects the accuracy of the model is severely impaired'. Therefore any improvement that can be gained in this region will be valu-

able, especially considering that estimates of bubble populations resulting from inverse techniques will be strongly influenced by the modelled response of the bubble around resonance.

As can be seen from the first graph (column (a)) in the bottom row of figure 3.3, above resonance the curve predicted by the new nonlinear method agrees well with that predicted by the linear formulation. In this region the amount of energy dissipation is small, as indicated by the small area enclosed by the loop in comparison to the resonance condition (note the difference in orders of magnitude of the x axes between the three graphs).

In the case close to resonance (column (b)), the amount of dissipation is much larger and identification of a spine corresponding to a single sound speed within one cycle of the is no longer valid as discussed in section 3.1.2. It may be the case that this increase in dissipation is causing the inaccuracies of the method close to resonance. It is also of interest to note the different resonance frequencies of the linear and nonlinear bubbles causing a shift in the gradient of the spine of the loop.

Finally the third graph (column (c)) shows the case below resonance. As discussed above the P-V curve contains a 'cross-over' that may be caused by a second harmonic in the response of the bubble. This 'cross-over' is entirely lacking from the linear case and is due to the monochromaticity in the linearly modelled response of the bubble.

3.7 Summary

This chapter has developed a method of calculating the nonlinear extinction cross section of a bubble. The initial approach taken, while shown to reduce the same solution as the linear case, was ultimately shown to be inaccurate at high amplitudes. This was because of the failure of the complex sound speed model to take into account the transferral of energy between frequencies and the variation of the sound speed within a oscillatory cycle. However appreciation of these facts revealed an alternative approach based upon cal-

culation of the energy dissipated by the bubble from an incident plane wave. This parameter can be calculated from the area enclosed by a plot of incident pressure against bubble volume. Examination of these plots also reveals some understanding of the dynamic response of the bubbles. Comparing them to existing state-of-the-art linear theory exposed a possible explanation for the inaccuracies of that theory around bubble resonance.

The chapter then goes on to describe the algorithm developed for obtaining the extinction cross section of a bubble making use of the Herring-Keller equation to obtain a bubble radius time history. Owing to the intensive computational nature of the solution of this second order differential equation, the calculation was restricted to a single layer. As an example of the use of this code and a means of validating the model numerical solutions were found using the new nonlinear model for a 100 μm bubble driven between 1 and 100 kHz at both low amplitude (zero-peak pressure of 100 Pa) and high amplitude (zero-peak pressure of 50 kPa). The solutions were then compared to an analytical expression for the linear extinction cross section. As expected the nonlinear solution agreed with the linear solution at low amplitude but at high amplitude energy was spread into other frequencies which could not be represented by the current linear model.

This chapter has addressed the need expressed in chapter 2 for a model of acoustic propagation in bubbly liquids that does not include the assumptions of linearity, monochromaticity and steady-state inherent in the current theory. While the model has not made any of these assumptions it has been necessary to impose the assumptions of steady state and cloud homogeneity because of computational considerations. It was also necessary to assume a spherically symmetric bubble response, that the wavelength of the insonifying wave was large compared to the bubble radius and that the bubble void fraction is low . The following chapters will describe an experiment to measure the bubble population in the surf-zone, a region where use of this new theory may be potentially beneficial.

Chapter 4

Development of an experimental system for estimating oceanic bubble populations

Previous chapters have outlined the theoretical development of a nonlinear, inverse method of estimating bubble populations. This chapter will describe the development of the systems and techniques necessary to realize an experimental system capable of the estimation of ambient bubble populations in an oceanic surf-zone environment. This will require development or selection of suitable acoustic transducers (both for transmit and receive) and development of the associated apparatus necessary for generating high amplitude waveforms and making accurate received level measurements. It will also be necessary to design appropriate driving signals with which to insonify the bubble cloud and also to develop suitable techniques for extracting the propagation characteristics from the time histories. The chapter will conclude by describing and presenting the results from a set of trials characterizing an artificially generated bubble cloud in a laboratory environment.

4.1 Design of acoustic insonification signal

The signal used to drive the bubble cloud is of primary importance in the estimation of that cloud's population. This is because it determines the response of the bubbles and hence the extent to which the model that is used as part of the inversion process is valid. Factors that must be considered include the frequency content of the driving pulse, the pulse duration, its amplitude and the overall duration of any measurement. Two alternative schemes exist for the driving signal. The first, used by the majority of investigators [6, 19, 40, 45], is based upon narrowband pulses, and the second [20] is based upon broadband pulses. As the focus of this system is the surf-zone, the former of these two options was chosen as it was expected that this would provide a superior signal-to-noise ratio, a factor likely to be critical in the surf-zone.

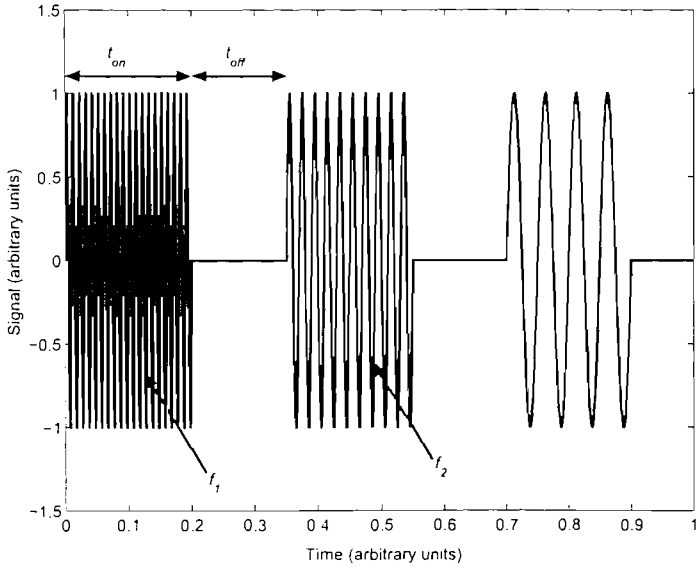

Figure 4.1: Illustration of the construction of a concatenated 'pulse train' of narrowband short duration pulses.

The narrowband signal was constructed using short pulses (of duration dictated by the arrival of the first multi-path reflection) of varying frequency

followed by an un-driven period to allow any reverberation to die away. Ten of these pulses were concatenated together to give a 'pulse train' covering the frequency range of interest. Figure 4.1 illustrates the construction of such a signal. The duration of the signal would be $G \times (t_{on} + t_{off})$ seconds (where G is the total number of frequencies used). An implicit assumption is that the bubble population remains stationary during this period.

4.1.1 Frequency content

Each tone within the pulse train is designed to cause bubbles at the centre of a radius bin to respond at their resonant frequency. As discussed in section 1.2, there are a number of different models of bubble dynamics and a number of different formulations for the resonant frequency of a bubble. The equation of motion used throughout this work (in both its linear and nonlinear forms) is the Herring-Keller equation [33]. However, no simple expression for the natural frequency of a bubble is yielded from this equation. In order to achieve a natural frequency close to that inherent in the Herring-Keller equation the Rayleigh-Plesset equation is used, with the natural frequency determined using equation 1.17.

In order to keep the number of elements in the matrix $\boldsymbol{K}$ small[1] the number of frequencies was constrained to ten (the number of elements to be calculated is the square of the number of frequencies used). As will be seen later, the system used through the laboratory and sea trials evaluates bubbles with an equilibrium radius between 16 μm and 115 μm. The resonant bubble radii and frequencies used are shown in table 4.1.

[1] This is especially important when considering the computation time involved in calculating the nonlinear extinction cross section as discussed in chapter 3.

Bubble radius (μm)	Frequency (kHz)
16	197.540
27	118.959
38	85.302
49	66.561
60	54.604
71	46.306
82	40.207
93	35.535
104	31.839
115	28.842

Table 4.1: Resonant bubble radii and driving frequencies used throughout the laboratory and sea trials. Assuming an air bubble enclosed by seawater.

4.1.2 Pulse duration

The desired pulse duration is influenced by different factors. However, as discussed in section 2.3.1, unless the source in use is sufficiently directional that only direct propagation is significant, the pulse duration must be determined by the distance to the nearest boundary. For most sources such an assumption cannot be safely made, and hence the pulse duration used during these trials was determined with reference to equation 2.38. Assuming that the measurement takes place in water 2 m deep and that the measurements are made in the centre of the water column, the maximum pulse duration that would exclude multi-path propagation would be 500 μs. The number of cycles at each frequency was restricted to an integer value such the the pulse duration was less than the this value.

Having determined the maximum pulse duration, radius time histories were generated in order to assess the response of the bubbles to such a pulse. In order to give an indication of the likely range of responses, four cases were examined, that of the smallest and largest bubbles excited by both the highest

and lowest frequencies used in the proposed experiment. Figure 4.2 shows these responses. In order to show the steady state region of the response the modelled pulse is semi-infinite. Examining the worst case (figure 4.2(d)) it can be seen that the amplitude does not deviate from the steady state values by more that 15 % after 500 μs.

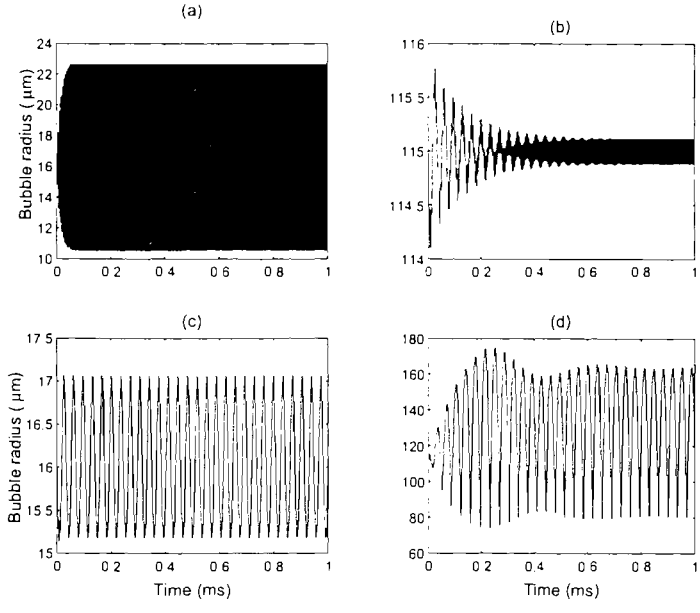

Figure 4.2: Four bubble responses calculated at both the smallest and largest radii as well as the lowest and highest frequencies used in the proposed experiment. (a) 16 μm bubble driven at 197.5 kHz (b) 115 μm bubble driven at 197.5 kHz (c) 16 μm bubble driven at 28.8 kHz and (d) 115 μm bubble driven at 28.8 kHz.

4.1.3 Pulse amplitude

Section 2.1.5 solved the forward problem for oceanic bubble populations. The open water population measured by Phelps & Leighton [45] gave a peak attenuation of 28 dB/m at 25.4 kHz. Bubble populations (and hence attenuation) in the surf-zone are expected to be considerably greater than those

encountered in open ocean although experimental measurements in such regions are scarce. Solution of the forward problem for an existing data set [6] (albeit at only four bubble radii and in extremely high void fractions) suggest an attenuation as great as 300 dB/m at 59 kHz. Measurements in the far field of a directional source in such an environment are obviously extremely difficult, although in more moderate surf-zone conditions a lower attenuation could be expected. For the purposes of system design an attenuation of approximately 100 dB/m was assumed, therefore implying the need for a source capable of source levels in the region of 200 dB re 1 μPa @ 1m in order to assure high signal to noise ratio at the receiver. At the time of thesystem design the extent of nonlinearity of response that such a driving pressure would cause in the bubble oscillations was unknown.

4.1.4 Overall duration of pulse

Given that a narrowband 'pulse train' was to be used, the separation between the pulses was important. It could be argued that such a separation is not necessary since consecutive pulses have different frequency content, and hence reverberation from one is unlikely to effect another. However the resonant frequencies of the larger bubbles can be similar and additionally it is also desirable (for modelling purposes) to assume that all the bubbles have fully rung down before the onset of the next driving pulse. For these reasons it was decided to include a delay between the driving pulses.

In order to determine an upper bound on this separation a 30 kHz pulse with a pulse duration of 100 μs was emitted at depth of 1.5 metres in a test tank. The tank was 8 metres by 8 metres by 5 metres deep and was concrete-walled. The signal was received by a Bruel & Kjaer hydrophone type 8103 position on-axis with the source at a distance of 1.5m. The output of the hydrophone was charge amplified by a Bruel & Kjaer type 2635 charge amplifier and then recorded using a National Instruments 6110E Data Acquisition Card. For more details of the source used see section 4.3. See figure 4.3 for a diagram of this experimental setup.

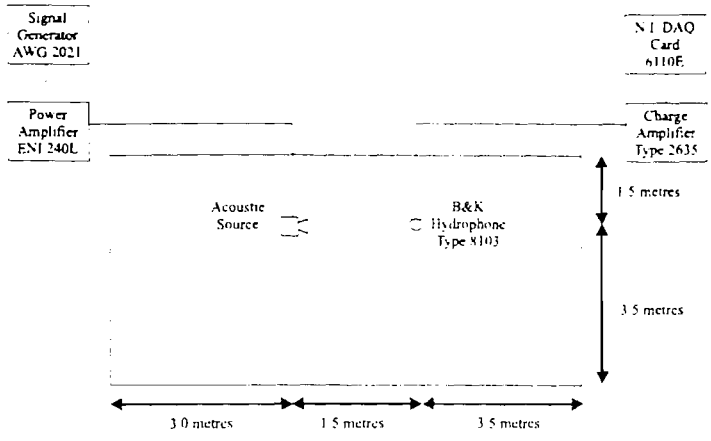

Figure 4.3: Experimental set-up for pulse separation tests. A 100 μs, 30 kHz pulse was generated and received at 1.5 m on-axis distance.

It is anticipated that this environment will be much more reverberant than any likely oceanic measurement. This is due to the fact that a concrete walled boundary will have a much higher reflection co-efficient than a sandy ocean bed. In addition the volume absorption will be much lower in a bubble-free environment than in a bubbly environment such as the oceanic surf-zone. All these factors will serve to reduce the reverberation time of the environment.

Figure 4.4 shows the time history for the short pulse emission. The reflections are small compared to the direct path pulse. Examination of the data reveals reflections occurring at $t = 2$ ms and $t = 6$ ms which, from the geometry shown in figure 4.3 can be identified as surface and wall reflections respectively. All reverberant effects drop beneath the measurement noise floor for $t > 10$ ms. In order to ensure no interference occurs, this figure was doubled to 20 ms when designing the pulses. Modelling of bubble responses reveals that the longest period expected for ring down of a bubble is less than 1 ms. Hence the bubbles can be assumed to be at rest at the onset of the driving signal.

Ideally the bubble distribution should be considered stationary over the time-frame of the measurement. In any measurement using the techniques described above, the turbidity of the environment being measured will deter-

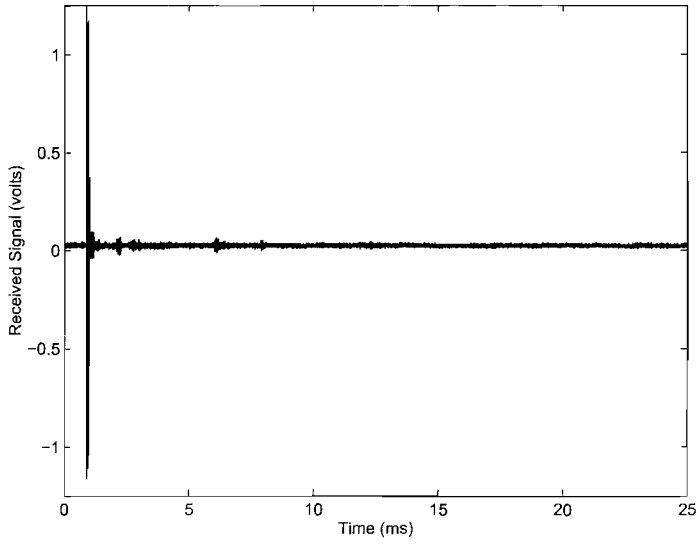

Figure 4.4: Received time history at 1.5 metres from the source. Notice the signal has dropped beneath the noise floor for $t > 10$ ms.

mine the overall duration of the pulse. The system discussed here is intended to measure the ambient bubble population generated in the surf-zone. While this environment is expected to be more turbulent than an open ocean environment, it will be significantly less turbulent than the environment directly beneath the breaking waves. For such measurements it would be necessary to use a short pulse separation (perhaps interleaving different frequencies to ensure good frequency separation) or to use broadband pulses to excite the bubble cloud. Figure 4.5 illustrates the difference between a measurement directly beneath a breaking wave and a measurement of the ambient bubble cloud in the surf-zone following the passage of the breaker. As can be clearly seen the velocity of the bubble field is considerably lower in the latter case .

For $t_{on} = 500\mu$s, $t_{off} = 20$ ms and $G = 10$ (where G is the total number of frequencies) the whole signal would take 205 ms to elapse. Given that the separation of the hydrophones is 0.15 m the maximum average velocity of the cloud should be less than 0.7 m/s for this pulse duration. While this velocity would certainly be exceeded directly within a breaking wave (or indeed as the

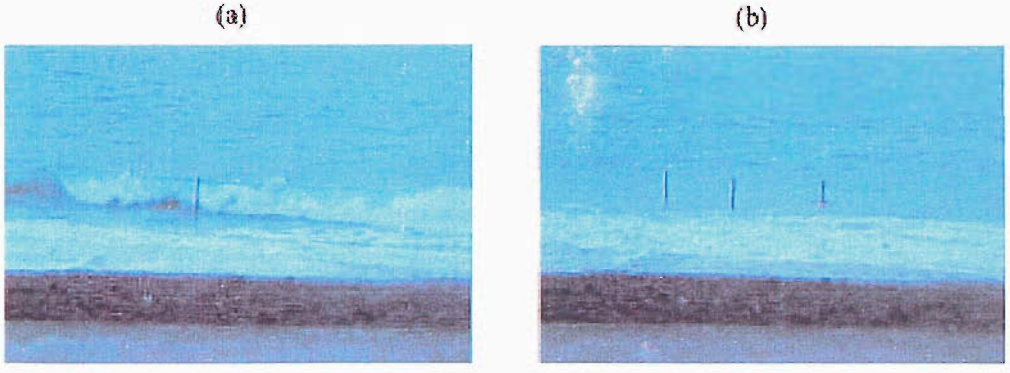

Figure 4.5: (a) Example of a breaking wave bubble population (b) Example of an ambient surf-zone bubble population. Measurement of (a) would require different pulse characteristics and may be invalidated by the high void fraction within the wave.

breaking wave travels toward the beach) the velocity of the bubbles within the *ambient* cloud is likely to be low. Hence, stationarity will be assumed for overall pulse durations O(0.1) seconds provided measurement relates to the ambient bubble cloud left behind the breaking waves rather than the breaking waves themselves.

4.2 Extraction of propagation characteristics from time histories

The method of extraction propagation characteristics from recorded time series data needs to be considered. Accurate determination of these terms is important because of the sensitivity of the inversion to noise (see section 2.2). The measurement is made more difficult still because the path lengths over which attenuation must be measured will be short (owing to the fact that the bubble population must be considered homogeneous between measurement positions). Any errors in measurement of the value over a short path length will be scaled when quoting the value per metre. The following section will

detail how these parameters may be measured for narrowband signals.

A system calibration undertaken prior to any bubble measurements being taken would improve the accuracy any measurements. This would require measuring the propagation characteristics in a bubble-free medium using the same set of transducers, driving signals and associated electronics. These measurements could then be compared to those taken in bubbly water and the *excess* attenuation calculated. It could be assumed that any excess attenuation was induced by bubbles. This process has the effect of removing any systematic errors from the measurement including hydrophone response, losses due to geometric spreading and attenuation due to absorption in the water (although this factor is likely to be very small over a short path length).

4.2.1 Attenuation

As discussed in chapter 1, attenuation is defined as the reduction in acoustic intensity of a sound field. The instantaneous acoustic intensity of a plane wave is proportional to the square of the instantaneous acoustic pressure (equation 3.28). Intensity is commonly expressed as a value in decibels calculated using a reference intensity, i.e. $10log_{10}(I/I_{ref})$, and hence the change in intensity levels, or the attenuation, can be expressed as

$$A = 10log_{10}\left(\frac{I_b}{I_{bf}}\right) \tag{4.1}$$

However, in practice, since the ratio will remain the same, the attenuation may be determined from the incident pressure upon the hydrophone, which squared, is proportional to the intensity. Therefore the total bubble-induced *excess* attenuation at the i^{th} hydrophone in dB, $A_i(f)$, can be calculated as a function of frequency:

$$A_i(f_g) = 20log_{10}\left(\frac{H_i^b(f_g)}{H_i^{bf}(f_g)}\right) \tag{4.2}$$

where $H_i^b(f)$ and $H_i^{bf}(f)$ are the amplitudes of the Fourier transforms at the measurement frequency in the bubbly and bubble-free environments respec-

tively at the i^{th} measurement position. The attenuation per unit length, A, between two measurement positions can then be simply calculated using x_d, the distance between the two measurement positions.

$$A = \frac{A_{i+1} - A_i}{x_d} \tag{4.3}$$

4.2.2 Phase Speed

Previous investigators [19,20] discuss methods of measuring the phase speed in the medium using cross-correlation to determine the arrival times of the signal traveling between two measurement positions. While this does measure the travel time and hence, with knowledge of the distance, speed of sound this is, in fact, not a measure of the *phase speed* but a measure of the group speed. The distinction between the two is not crucial unless the medium in which the wave is propagating is dispersive, as is the case in bubbly media. In a non-dispersive medium all frequencies travel at the same speed whereas in a dispersive medium the propagation speed will vary as a function of frequency. The group speed, which is the speed at which the centre of the wave packet will travel is given by $\partial\omega/\partial k$ where as the phase speed is given by ω/k [5].

Review of the literature yielded no suitable technique for measuring the phase speed that could be based upon a series of pulses. The only system found that is capable of true oceanic phase speed measurements makes use of a resonant cavity [39]. The disadvantage of this technique is that the plates that form the cavity are intrusive and their presence may well affect the measurement. As no clear benefit was found in basing inversion data on both phase speed and attenuation [19] it was decided to measure attenuation only in the oceanic system.

4.3 Choice of Appropriate Acoustic Source

The transducer design discussed in this section was carried out in collaboration with Mr. P. Doust of Thorn Marine Systems.

Measurement of bubble populations in a surf-zone environment places a demanding set of requirements upon the acoustic source and as such care must be taken when selecting such a source. The source must have sufficient power to penetrate the bubbly medium and still be received with a high signal to noise ratio at the receiver, the beam-width must be narrow so as not to cause multi-path reflections and well defined in order that a sensing volume can be established. Each of these parameters will be discussed in the following sub-sections.

A transducer able to fulfill these criteria was developed in collaboration with Alba Ultrasound and Thorn Marine Systems. In order to achieve a wide bandwidth, flat frequency response, high power transducer it was necessary to employ a three element array and to exploit broadband matching techniques [69]. Figure 4.6 shows the dimensions and construction of the array.

Each element in the array was manufactured to a different dimension in order to maintain a constant near-field/far-field interaction. The near-field/far-field interaction d was calculated by considering each element to be a line array of length s, where s is the largest dimension of the piezo-ceramic crystal. The resonant frequencies, broadband frequency ranges, dimensions and near-field extents of each of the three elements which make up the array are shown in table 4.2.

Broadband matching was used to extend the frequency response of the transducer. This was necessary because an unmatched electro-acoustic transducer is essentially a narrowband device and is only efficient around its own natural frequency. In order to extend the bandwidth, a network of inductors, transformers and capacitors can be combined with the transducer to create a band-pass filter of significantly greater bandwidth [69 71].

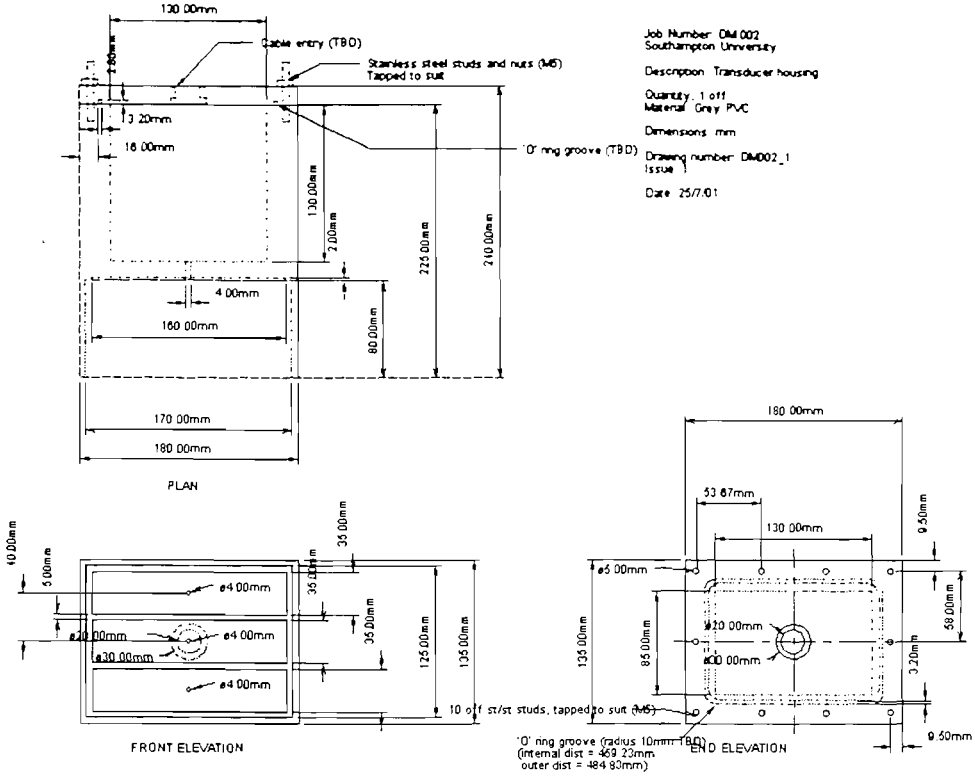

Figure 4.6: Engineering drawing of three-element acoustic array. *Acknowledgement: Alba Ultrasound*

f_{res} (kHz)	f_{low} (kHz)	f_{high} (kHz)	s (mm)	d (m)
50	30	80	158	1.33
160	80	270	91.3	1.50
400	270	800	53	1.49

Table 4.2: Operating Parameters of Broadband Transducer. Note that the high frequency element of the transducer was not used during the experiments described here.

4.3.1 Frequency Response

There are several reasons why the frequency response of the acoustic source is of importance in the estimation of bubble population. The first of these is that the transducer bandwidth determines the range of bubble radii that can be excited at their resonant frequency. Therefore in order to evaluate the population across a wide spectrum it is desirable to employ a broadband transducer. Secondly the transducer's amplitude frequency response should reasonably flat, this is for two reasons. The first is that pulses of an even and repeatable amplitude are obtainable without digital correction. For example, a transducer with an uneven frequency response may require a large voltage input to achieve a fixed pressure output at one frequency but at a different frequency much smaller voltage may be required to achieve the same pressure. While this would nominally re-create a flat frequency response, any instability in the input voltage (or some change in the source characteristics e.g. surface loading pressure) would greatly affect the output of the transducer and would invalidate any system calibration that had taken place. The second effect is that by achieving a flat spectral response from the transducer the full dynamic range of an analog-to-digital converter can be utilized on the receiver input, thus adding to the accuracy of the measurements.

Figure 4.7 shows the frequency response of the mid-frequency range element in the array calculated using equivalent circuit theory with and without broadband matching. Such a response is typical of all three elements in the source. As can be seen, without broadband matching the response of the matched element is essentially narrowband, centred on the resonant frequency of the active element. However when broadband matching [69] is used the resultant frequency response is flat over a large frequency range. All three elements comprising the source were matched to give a radiated pressure level of 195 dB re 1μPa at 1 metre. Such a source level will provide a high signal to noise measurement even in relatively dense surf-zone bubble clouds provided the range is kept small. The -3 dB points at either end of the middle element's frequency range were overlapped with the -3 dB point

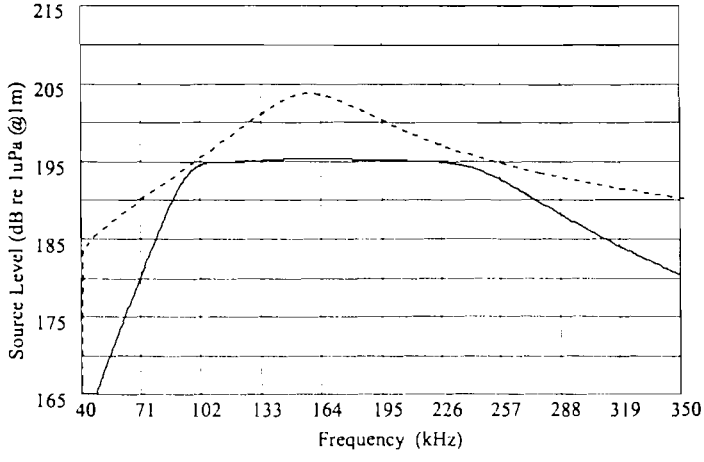

Figure 4.7: Frequency Response of mid-frequency element in array with and without matching. Theoretically calculated using equivalent circuit theory. Dashed line shows unmatched response and solid line shows matched response. *Acknowledgement: P.E. Doust*

of the adjacent element in order to give a smooth frequency variation across the entire frequency range of the source. The actual frequency response of the source was not measured but is not critical since all measurements are based upon the ratio of bubbly to bubble-free measurements. For the purposes of these experiments the transducer was only used up to 200 kHz (as this was the highest frequency for which a calibrated receiver was available). A consequence of this was that it was not possible to use the third element of the transducer however the high frequency element of the source was intended for use in another project investigating high frequency sediment acoustics.

4.3.2 Directivity

As discussed in section 2.3 it is desirable to have a highly directional transducer with a strong main beam and weak side lobes in order to minimize any multi-path reflections that may impinge on the receiver.

Theoretical calculation made by Alba Ultrasound on the directivity of the

	θ_{low}	θ_{high}
Element 1 (30 kHz-80 kHz)	16°	5.4°
Element 2 (80 kHz-270 kHz)	9.3°	3.1°
Element 3 (270 kHz-800 kHz)	5.3°	1.8°

Table 4.3: Theoretically calculated beam-widths of Transducer. The beamwidth is defined as the angle between the axis of the source and the −3 dB point of the directivity pattern.

3 element array show it to be highly directional and shading techniques used by Alba Ultrasound in the design of the source mean side lobes are expected to be small. The predicted beam-widths for each element at its upper and lower frequency bounds are shown in table 4.3. The actual directivity pattern of the transducer was not measured owing to time constraints within the study and such a measurement is recommended for future work. In place of a measured directivity pattern a linear interpolation between the theoretically predicted values has been assumed. A radial symmetry will be also assumed when calculating the sampling volume from these values.

4.4 Experimental Apparatus

Development of apparatus suitable for measuring bubble populations in shallow water or in the surf-zone is a challenging task in its own right. The range of bubble radii under consideration and the attenuating nature of the medium necessitate a high amplitude, high frequency driving signal. The apparatus either has to be driven and powered from the shore (or from a boat) and connected via an umbilical cable carrying the signals; or must be autonomous and self-sufficient either sending its data back to shore wirelessly; or be designed for retrieval and download of data after a set period. Owing to the limited equipment, facilities, time and funds available, it was decided to focus on a set of apparatus that could be deployed by hand in the surf-zone envi-

ronment and operated on shore via an umbilical. The rig would be retrieved within a short time scale (several hours or days) and constantly monitored over this period. This section aims to describe the transducers, electronics, software and associated apparatus that was developed for use in a surf-zone oceanic environment. While there was an inevitable amount of re-design and improvement between trials, this section will only discuss the final system used, variations from this system will be discussed on a trial-by-trial basis in chapters 5 and 6.

4.4.1 Signal Generation

Two methods of signal generation were employed in parallel. One that relied upon equipment readily available that had been used for similar work previously, and the other which offered great benefits over the existing apparatus.

The first of these two systems employed a Sony Tektronix 2010 Arbitrary Waveform Generator (AWG) in order to create the waveforms. This device is capable of outputting the contents of a buffer at a maximum rate of 250 MHz on two channels simultaneously. The maximum buffer size is 262,144 points. In order to generate the 'pulse train' (as discussed in section 4.1) the clock frequency was set to 100 MHz and waveforms generated corresponding to one cycle. These waveforms were then queued in a sequence file which generated the appropriate number of cycles dependent upon the frequency being emitted. The two channels were used to drive element one and element two of the transducer independently and the sequence files were concatenated in such a way that appropriate signals were sent concurrently to each element. The frequencies were selected by calculation of the resonant frequencies of ten bubble radii equally spaced in the radius domain (as shown in section 4.1). Figure 4.8 shows the signals generated for a ten tone pulse with a pulse length of 500 μs.

Each waveform was then loaded onto the AWG using a GPIB interface. After signal generation each channel was then amplified by an ENI 240L power amplifier. This power amplifier has an output of 100 watts and a

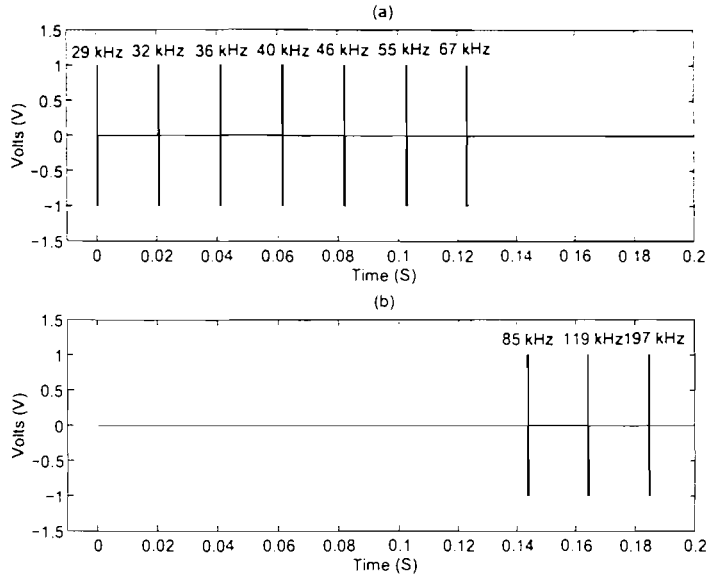

Figure 4.8: Signals generated by arbitrary waveform generator for 10 tone tests at 500 μs pulse lengths. (a) Signal sent to element 1 (30 kHz to 80 kHz) (b) Signal sent to element 2 (80 kHz to 270 kHz).

frequency range of 10 kHz to 10 MHz which will easily cover the operating frequency range of the transducer. The output of the power amplifiers is then transmitted via 2 twisted pairs in a 200 metre long. 18 screened twisted pair armoured cable. This cable is used to send and receive signals from the measurement site to shore. Figure 4.9 illustrates the experimental set-up for signal generation.

The second system of signal generation was used as a backup system and replaces the AWG with a National Instruments 6110E Data Acquisition (DAQ) card. This is a PC based PCI card having two analog outputs capable of outputting at 4MS/s (one channel) or 2.5 MS/s (both channels) with a 16 bit accuracy. This card can be simply controlled from within Matlab using the Data Acquisition Toolbox allowing any vector generated within Matlab to be output as a driving signal. This is desirable as it greatly improves the flexibility of the system, reduces setup times, removes the need for extra instruments and also eliminates the slow GPIB interface. Also the card holds

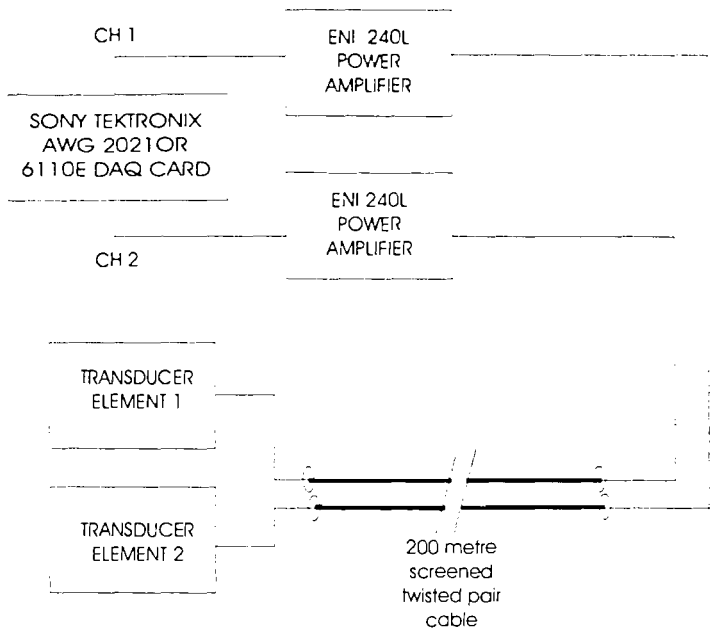

Figure 4.9: Diagram of apparatus on signal generation.

4 analog input channels which can be used for signal acquisition. This further reduced the need for external apparatus and allowed all signal generation and acquisition to be simply controlled using one standard PC within a Matlab environment. This is discussed further in section 4.4.2.

4.4.2 Signal Acquisition

Signal acquisition was performed using an array of Bruel & Kjaer type 8103 hydrophones. The calibrated frequency range of the 8103 hydrophone is 0.1 Hz to 200 kHz. This precluded use of the element 3 (270 kHz - 800 kHz) of the acoustic source (see section 4.3.1) but this will be employed in other experiments not reported here. The output from each hydrophone was amplified using a charge amplifier, to generate a voltage proportional to the pressure incident on the hydrophone. This voltage was then amplified by a gain factor determined via a voltage transmitted on a single channel from shore (due to limitations on the number of channels, the hydrophone gain

factors were set on groups of two i.e. hydrophones 1 and 2 had the same gain factor). This allowed the operator to adjust the sensitivity of the hydrophones in order to optimise signal to noise. The acoustic data was transmitted using a twisted pair in the 200 m armoured cable using a 'push-pull' system. This essentially divides the signal received at the shore end on one of the twisted pairs by a reference signal on the second twisted pair. Any inducted currents such as cross-talk will be picked up by both channels and hence can be divided out when received. The remaining channels in the 36 channel cable were used to carry the driving signals, to supply power to the electronics and for other experiments being run using the same apparatus. The printed-circuit boards (PCBs) were securely mounted on aluminum plates both to provide a robust mounting for the circuitry and also to act as a heat-sink for any excess heat that may be generated by the operational amplifiers mounted on the boards. For more details of the design of the rig see chapter 5. Figure 4.10 shows a photograph of the electronics used to received the signal and to transmit down the cable. Prior to each trial the gain factors in the internal electronic were adjusted with a Bruel & Kjaer type 4229 hydrophone calibrator driving the hydrophone. Each channel was adjusted to give 1 mV/Pa output. While not strictly necessary because the attenuation is calculated via a comparison with bubble-free water, it helped ensured that a high signal to noise ratio would be received and provided a secondary level of confidence in the received data.

In order to receive the signals on shore a signal 'break-out' box was constructed with terminals for the send and received signals. This not only provided an interface to the cable but contained the shore based DC power supply. with which the canister mounted electronics would be powered. This also incorporated a number of fail-safe shutdown devices and the gain controls for the hydrophones.

The received signals were acquired using a Lecroy 9344L 4 channel digital storage oscilloscope sampling at 1 MS/s and using 8 bit quantization. As the highest frequency contained with the signal is 200 kHz (with the hydrophone

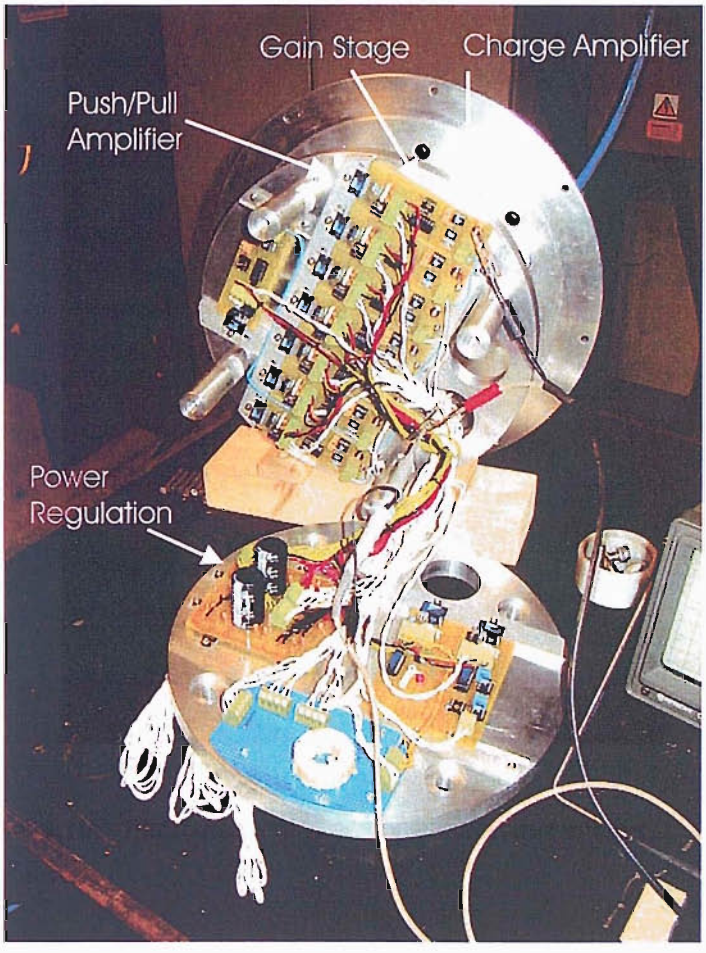

Figure 4.10: Photograph of internal electronics required for signal receive and transmit.

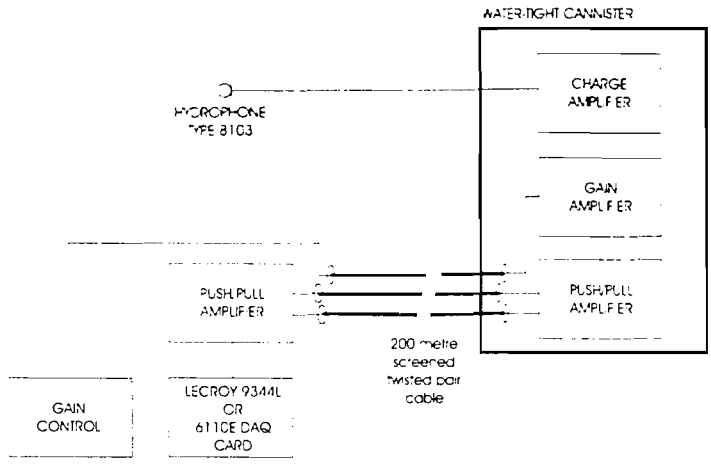

Figure 4.11: Diagram of one hydrophone channel apparatus on signal receive.

effectively acting as a low pass filter) this sampling rate is well in excess of the Nyquist frequency and hence when combined with a suitable low-pass filter should prevent aliasing. After each acquisition the waveforms were downloaded using a GPIB interface onto a PC and stored on the local hard drive for subsequent analysis. This process was slow however due to the number of channels being used, the high sampling rate and the slow speed of the GPIB link meaning downloading all channels took in excess of 1 minute. Figure 4.11 illustrates the experimental set-up for one hydrophone channel.

The National Instruments DAQ card was used as a backup means of acquiring data. This card is capable of acquiring up to 5 MS/s/ch simultaneously on 4 channels using 12 bit quantization and writing the data simultaneously to hard disc. Because the transfer of data from the card to the hard disc drive utilizes the PC's PCI bus and IDE interface, the data can be recorded in real time. When operating at the highest sampling frequency on all 4 channels the IDE interface to the hard drive may not support the data rate which is 2 bytes/sample $\times$ 5 MS/s $\times$ 4 channels = 40 MB/s. In order to overcome this two hard discs were configured as a Redundant Array of Independent Discs (RAID) using a FastTrack TX2 RAID controller giving a hard drive capable of a sustained transfer rate of 45 MB/s with a capacity

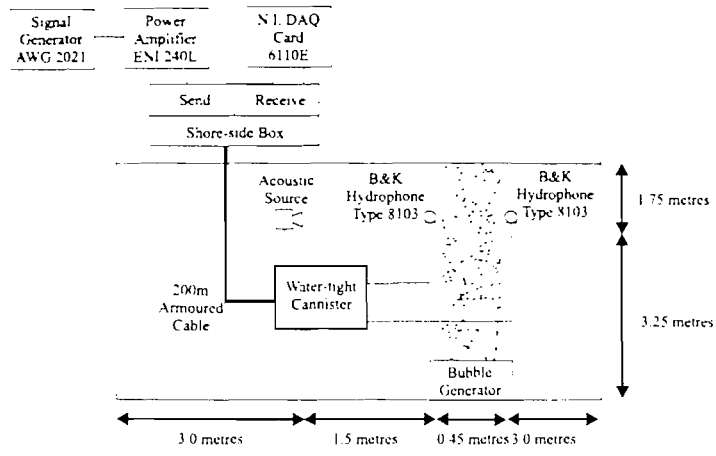

Figure 4.12: Experimental setup for characterization of electrolysis bubble cloud.

of 40 GB, enough for 15 minutes of continuous acquisition at the maximum sampling rate or 75 minutes at the 1 MHz rate used in these experiments.

4.5 Laboratory Tests

In order to test the system in a laboratory environment an artificial bubble cloud was generated using electrolysis. To do this a 14 amp current was passed through a submerged copper plate which formed an anode and a horizontal parallel copper plate positioned approximately 3 cm above the current-carrying plate which formed a cathode. Oxygen bubble formed on the underside of the cathode which, in order to disperse the bubbles, was rotated at 30 rpm. Hydrogen bubbles were formed on the upper face of the anode over which was placed filter paper in an attempt to trap and dissolve these bubbles before they could rise with the main cloud. This separation was felt necessary as the hydrogen bubbles will have different properties from those formed by oxygen.

The bubble generator was placed at the bottom of a 8 metre by 8 metre by 5 metre deep concrete walled tank filled with fresh water. Visual inspection

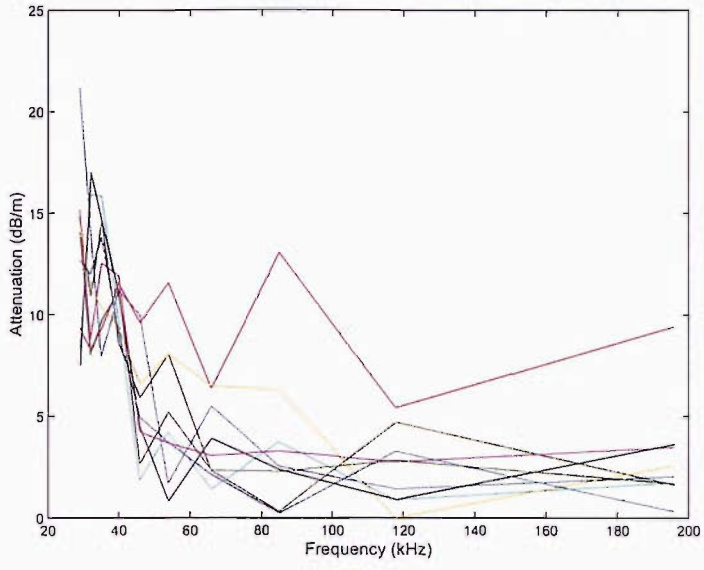

Figure 4.13: Measured attenuation from bubble cloud generated by electrolysis. The attenuation was determined using equation 4.3. The different colour lines correspond to different attenuation measurements taken approximately every 5-10 seconds (due to limitations of the available colour palette some colours are repeated). The two hydrophones were separated by 45 cm in order to maximize the homogeneity of the measured bubble population. The system was calibrated in bubble-free water prior to the measurement thus accounting for any losses due to geometrical spreading.

(by reflection of light from bubbles as they break the water surface) showed the bubble cloud generated to be circular with an approximate diameter of 5 metres and a roughly homogeneous spread of bubbles across this diameter. Two 8103 Bruel & Kjaer hydrophones were placed at a depth of 1.75 metres 0.45 metres apart and were centered on the cloud of rising bubbles. Figure 4.12 shows a diagram of this experimental layout.

Attenuation measurements were taken using the system described above with pulse trains consisting of 10 frequencies corresponding to equally spaced radii between 16 μm and 115 μm. The pulse duration used was 500 μs ensuring that there was no interference from multi-path reflections. The

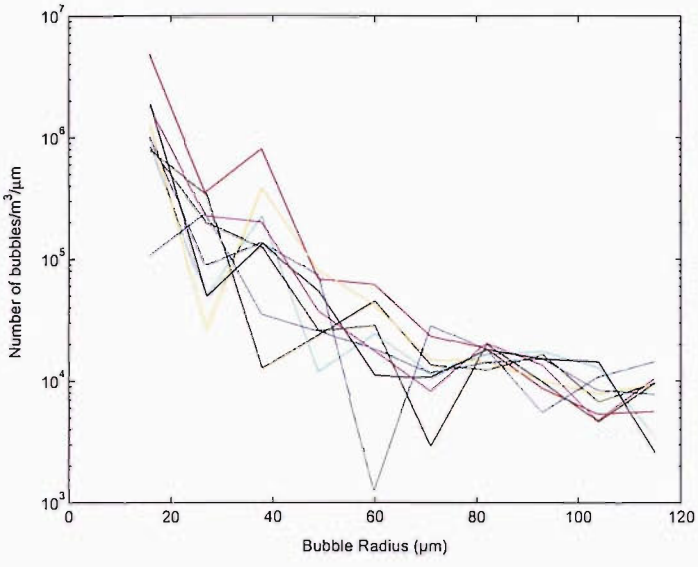

Figure 4.14: Estimated bubble populations from a cloud generated by electrolysis. The coloured lines correspond to the attenuation shown in figure 4.13. The estimated populations are calculated using linear theory only (due to limitations of the available colour palette some colours are repeated). The water in the tank is supplied from the mains water supply and is constantly filtered. Measurements were taken approximately every 5-10 seconds.

pulse separation used was 20 ms meaning that the whole signal took slightly over 200 ms to elapse. Figure 4.13 shows the attenuation as a function of frequency for each of the separate measurements. The attenuation at each measurement position was calculated by taking the magnitude of the Fast Fourier transform of each pulse. The ratio of this magnitude in bubble-free water to that in bubbly water was then taken in order to calculate the attenuation at each frequency (equation 4.2).

These attenuation measurements were used as the input into the inversion algorithm developed in section 2.2. At the time of the laboratory tests the nonlinear theory was not sufficiently advanced to attempt a nonlinear inversion and hence the results were calculated using linear theory. This was deemed sufficient as the laboratory tests were mainly intended to test

the system prior to a sea trial. The regularisation parameter, β, was chosen using the L-curve technique. Each population radius bin was scaled by the estimate of the sampling volume as described in section 4.3.2. The estimated populations are shown in figure 4.14.

As can be seen in figures 4.13 and 4.14 there is a considerable amount of inter-measurement variability, especially at the smaller bubble radii. This can be attributed to the stability of the bubble cloud as a function of time, which may be caused by fluctuations in the current drawn or inconsistent rates of bubble release from the electrode plates. While the estimated populations seem reasonable there is no independent measurement of the population against which to verify them.

4.6 Summary

This section has described the implementation of a system capable of making the measurements necessary to measure the ambient bubble cloud in the surf-zone. Discussion was made of techniques for extracting the necessary propagation characteristics from the recorded time histories. This highlighted an error in the methods used by previous investigators to measure phase speed. However, no practical method of measuring phase speed was found and hence it was decided to base the system upon attenuation only. Transducer designs and techniques for signal generation/acquisition were developed. Finally laboratory tests were undertaken to characterize an artificial bubble cloud generated by electrolysis and perform a test of the system prior to deployment. The next two chapter describe the deployment of an experimental rig in the surf-zone and the analysis of the data acquired respectively.

Chapter 5

Acquisition of sea trial data

Two multi-disciplinary sea trials [65, 72] were undertaken during the course of this study involving (at different times) five postgraduate students, four undergraduate students, three members of staff and seven technicians from two different departments at the University of Southampton. The aim of these trials was to simultaneously characterize the surf-zone bubble population using multiple techniques. Four different techniques were fielded

1. Passive bubble sizing [73]
2. Combination frequency [6]
3. Acousto-electrochemical [74]
4. Inversion of acoustic propagation

The first trial in November 2000 suffered from very stormy conditions and resulted in the experimental apparatus becoming damaged. However, experience gained during this trial enabled a considerable more successful trial to take place a year later. This chapter will describe the experimental setups used during both trials, the environmental conditions encountered and an initial quality check of the data. Chapter 6 will go on to describe the detailed analysis of the data acquired during these trials.

Figure 5.1: Photograph of the beach at Hurst Spit where the field trials were carried out. The beach has a steep shingle profile which was observed to change rapidly during poor weather.

5.1 Trials site

The site used for both the field trials was just at the base of Hurst Spit which is a man-made spit on the south coast of the UK (50° 42.48'N, 1° 35.01'W). As it is situated near the westerly mouth of the Solent, the site has a 'double-tide' and also can suffer from large waves due to the long fetch of the waves entering the English Channel from the Atlantic Ocean.

The site is a steeply sloping shingle beach turning to a sandy bed around the low water mark. There is a cluster of very large rocks on the eastern side of the beach which form the start of Hurst Spit. Figure 5.1 shows a photograph of the beach and figure 5.2 shows the transition of the bed from shingle to sand at the low water mark. It is assumed that the ocean bed at the measurement site, which is approximately 10-20 m from the low water mark, is sandy. The profile of the beach was found to change considerably during bad weather and 20 cm vertical bed movement was observed in one hour.

Figure 5.2: Photograph of transition between shingle and sandy bed. The bed at the measurement site is assumed to be sandy.

Two surveys of the site were available (figure 5.3). Each consists of a topographical land-based measurement taken as far out into the surf-zone as practical and a hydrographical ship-based sounding coming toward the beach. The two measurements approximately converge, however in one case an uncharted area of approximately 100 m exists. The two surveys show changes in vertical depth of up to 5 m over a four year period indicating the dynamic nature of the site. However the cut-out, which shows the surf-zone region is more constant with a slope of approximately 1 in 9. The figure also shows the position of the measurement rig. In both cases the rig was placed just beyond a small shelf in the surf-zone. This enabled the rig to be deployed safely in the maximum possible water depth.

5.2 First sea trial: Hurst Spit 2000

The first sea trial took place at Hurst Spit between 5th and the 15th November 2000. Tidal predictions showed a tidal range of 1.8 m which was antic-

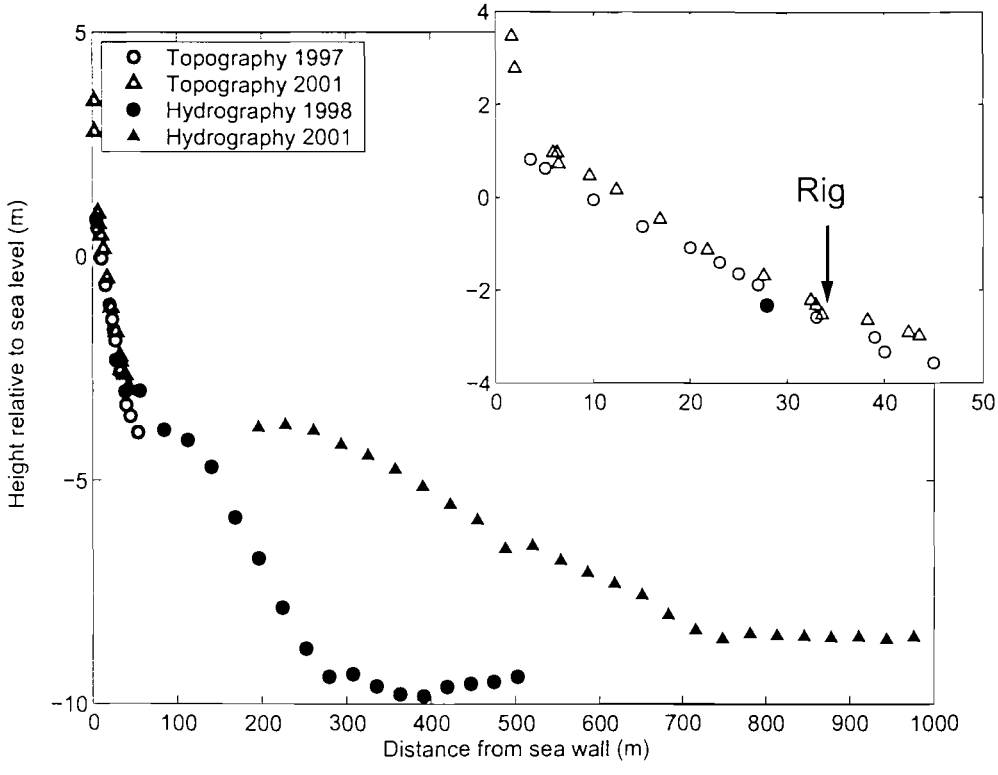

Figure 5.3: Topographical profile of the measurement site. The results of four surveys are shown: topographical surveys carried out on 01/09/1997 and 01/05/2001 and hydrographical surveys carried out on 01/12/1998 and 19/06/2001. Changes of up to 5 m in bed height between surveys are indicative of the dynamic nature of the site. The insert at the top right of the figure shows the topographical data in close-up and indicates the position of the measurement rig. Heights in metres corrected from Ordnance Datum Newlyn using tidal data at 16:00 GMT on 24-11-2001 to give height relative to sea level. Data supplied by C. Eastwick & A. Bradbury.

ipated to be enough to submerge the rig at high tide. The instrumentation used in this deployment was different to that described in chapter 4 and while it essentially performed the same function it consisted primarily of standard bench-top equipment rather than custom designed electronics. This meant that the apparatus required considerably more volume and hence two large water-tight canisters were used to house the wet-end electronics. The two cylinders were 35 cm in diameter and 1.5 m in length. The water displaced by such a large bodies was considerable and while both cylinders were packed with electronics, the buoyancy associated with each was very great. This, combined with the surface area that was presented to the breaking waves, made managing these objects in the surf-zone very difficult.

During the trial a wide range of weather conditions were experienced with wind speeds varying from 0.5 m/s to over 25 m/s. This resulted in very large waves, sometimes over two metres in height. Because of this, deployment of the experimental apparatus in the surf-zone was very difficult and three separate rig designs were used before successful measurements were made. Detailed description of the experimental setup will only be made where successful measurements were taken.

5.2.1 First deployment

The first deployment employed a rig that was designed to be built in shallow water (<1 m) at low tide with measurements being taken at high tide, when the rig was submerged. The rig was designed using scaffolding bars and clamps since it was anticipated that this would provide a strong but relatively light structure that also presented a minimal surface area to the wave motion. The design was cubic, measuring roughly 2.5 m on each side and 1.0 m high as the main structure to which the canisters and transducer arrays could be attached. At the base of each vertical element a large steel plate was welded. These plates would be buried in the sand and would counteract the buoyancy due to the air trapped with the water-tight canisters. Figure 5.4 shows a schematic of this design.

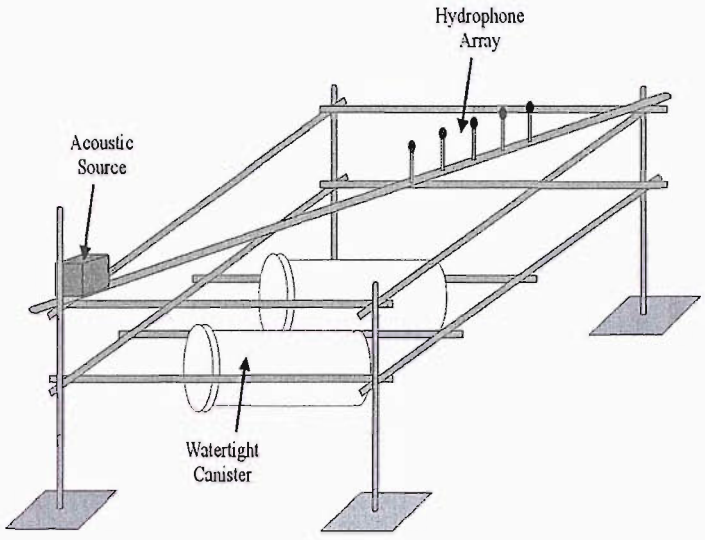

Figure 5.4: Schematic of rig design for the Hurst Spit 2000 [72, 75] sea trial, first deployment. The rig was designed to be constructed at the measurement site at low tide and to be submerged by the incoming tide at high tide when measurements would be taken.

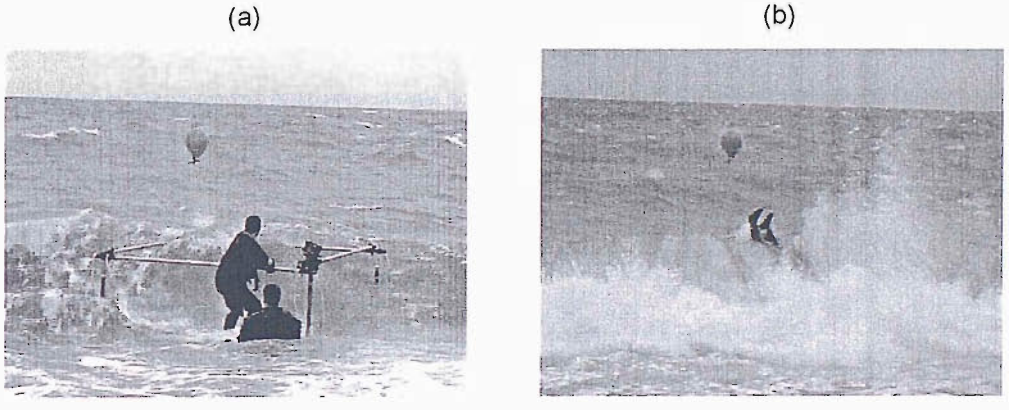

Figure 5.5: Two photographs, taken a fraction of a second apart in November 2000, showing (a) two postgraduate students (Meers and Simpson) attempting to bolt sensors to a scaffolding rig just deployed at sea; (b) Mr Simpson's feet (Mr Meers is completely buried by the wave).

However, construction of the rig in shallow water proved to be extremely difficult in even mild sea states due to the action of the breaking waves as illustrated in figure 5.5. The deployment of this rig was duly abandoned as unsafe and an alternative design considered.

5.2.2 Second deployment

A second deployment was then attempted using a rig that was entirely constructed prior to deployment and was then maneuvered to the measurement site. Four buoys were inflated and positioned on an axle at the front of the rig. The rig was then lifted and wheeled to the measurement position on these buoys. Over 125 kgs of extra weight was attached to the rig in order to counteract the buoyancy. Figure 5.6 shows a photograph of this rig.

This rig was deployed at low tide in shallow water and a tether attached in order to facilitate recovery at a subsequent low tide. However soon after deployment an unexpected storm formed with wind speeds in excess of 25 m/s and wave heights of several metres. Despite the rig having a total mass of over 500 kgs and being embedded in the sea-bed the energy within the waves was sufficient sufficient to lift the rig from the measurement site and deposit it upside down on the beach. As can be seen in figure 5.7 extremely heavy damage was sustained to the rig preventing any further data from being collected using this set of apparatus.

5.2.3 Third deployment

Having sustained damage to the main set of apparatus, an alternative experiment was undertaken. This made use of a secondary acoustic source that was available on loan from DERA Bincleaves. The transducer is a monostatic (i.e. source and receiver are co-located) sonar array with a calibrated frequency range of 200 kHz to 340 kHz with a beamwidth of between 4.7° and 15.4° depending on frequency.

Owing to the bandwidth of the acoustic source the range of resonant bub-

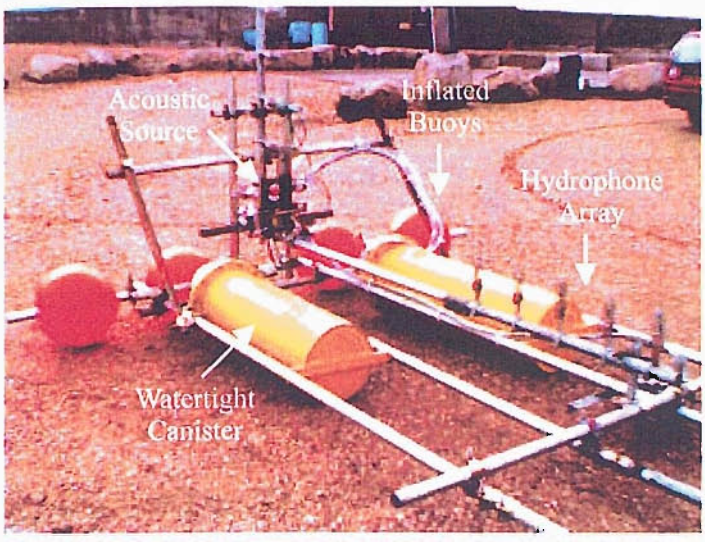

Figure 5.6: Photograph of the second rig designed for Hurst Spit 2000 sea trial. The rig was assembled on the beach and then wheeled to the measurement position using the inflated buoys as wheels.

Figure 5.7: Damage sustained to the second rig. Obviously the damage to the rig was so severe that no further measurements could be taken using this set of apparatus.

ble radii was restricted to 8.5-15.0 μm. This part of the spectrum of bubble radii has been seldom measured yet is close to the peak in the size distribution (at $\sim 20\mu$m) as measured by previous investigators [43,45]. Narrowband pulses at the appropriate frequencies (as described in section 4.1.1) were used to assess the bubble cloud in 0.5 μm radius bins over the above radius range.

In order to make an assessment of bubble numbers the backscatter from a target was measured, in this case the target was an inflated buoy mounted on a scaffolding pole. The buoy was positioned 0.5 m from the ocean bed and at high tide was submerged by approximately 1.0 m. The horizontal distance between the source and receiver was 2.35 m making a 4.7 m total path length. Figure 5.8 shows a schematic of this setup.

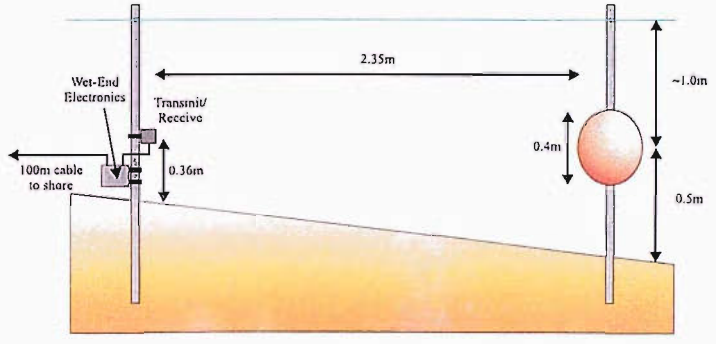

Figure 5.8: Schematic of rig design for first sea trial, deployment three. A mono-static sonar source was used to measure the back-scatter from an air filled buoy positioned 2.35 m away.

A schematic diagram of the apparatus used in the third deployment is shown in figure 5.9. The same system that was to be used in deployments one and two was used to generate the signals and to acquire the measured waveforms but the source and receiver were replaced by the borrowed mono-static system. The system had many similar characteristics to that described in section 4.4 including push-pull amplifiers to transmit and receive the signal down a 100 m armoured cable. The entire system had been calibrated both for transmit and receive so its sensitivity was known, although these

parameters were not strictly necessary since the attenuation was calculated as a ratio with respect to a nominally bubble-free condition.

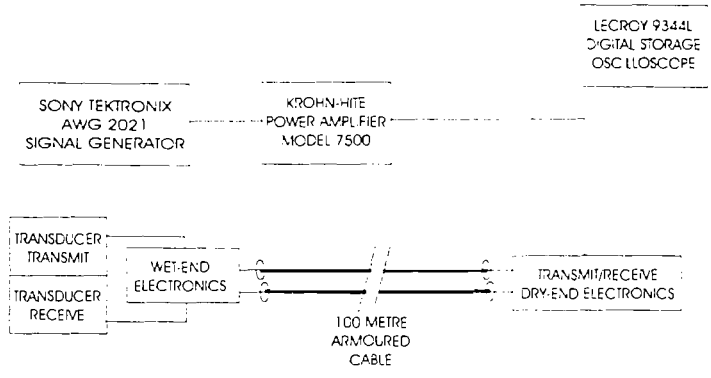

Figure 5.9: Schematic diagram of experimental apparatus used in the first sea trial, deployment three. Owing to damage sustained to the original set of experimental apparatus (similar to that described in chapter 4 an alternative setup was used.

Figure 5.10 shows the voltage time series acquired during one typical experiment. Each pulse consists of 20 cycles ranging between 200 and 340 kHz. The initial transmission in each case is followed approximately 3 ms later by the backscattered return from the buoy. The results from these data are presented in chapter 6.

5.3 Second sea trial: Hurst Spit 2001

The second sea trial also took place at Hurst Spit on 23rd-24th November 2001. Experience gained during the first sea trial enabled an improved design to be implemented for deployment of the apparatus. An entire trial could be carried out in under eight hours. In the event two trials on consecutive days were necessary, because on the first day the sea was very calm with minimal wave breaking activity. The second day brought a moderate SW breeze and stronger breaking waves (wave heights up to 1 m). During this trial no damage was sustained to the rig partly owing to the improved design and partly

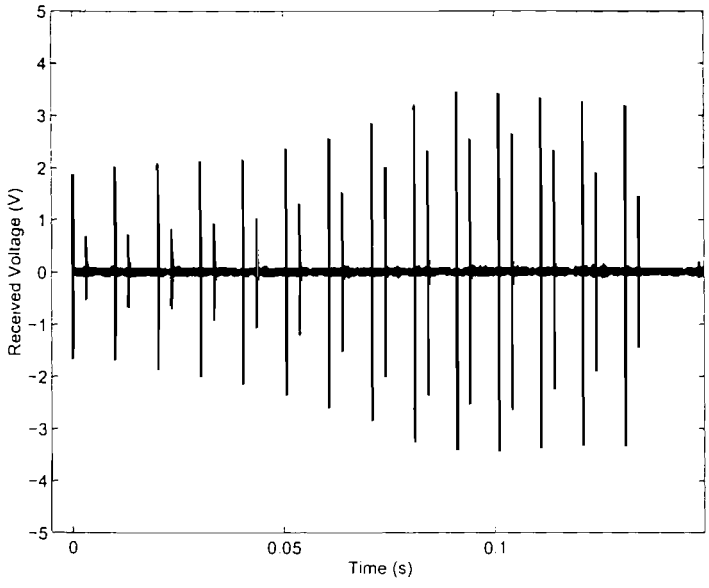

Figure 5.10: Typical voltage time history acquired during the third deployment at the Hurst Spit 2000 sea trial. The initial transmission from the mono-static sonar set is closely followed by the backscatter from the buoy position 2.35 m away.

because of the less hostile weather. This meant that the system described in section 4.4 could be used, enabling a broader range of bubble radii (16-115 μm) to be evaluated. The system used was a bi-static system where measurements are made over the direct path between source and receiver rather than from the back-scatter from a target (as in the previous trial).

5.3.1 Rig design

The primary change in the design or the rig was the miniaturization of the electronics contained within the water-tight canister. During the first trial the wet-end electronics consisted primarily of bench-top equipment and one of the major difficulties encountered was the buoyancy presented by the large canister necessary to contain this equipment. Therefore printed circuit board solutions (as described in section 4.4.2) were developed to replace this equip-

ment and reduce the volume required inside the water-tight canister. Before miniaturization two canisters of 35 cm diameter and 1.5 m length were required. After miniaturization one canister of 35 cm diameter and 50 cm length contained all the necessary electronics. This greatly reduced the buoyancy that had to be counteracted and also reduced the overall mass of the rig, making handling easier.

The issue of deployment and retrieval of the rig was also addressed. The dependence on the tide times in the first trial was partly responsible for the damage that occurred to the rig since it could not be safely retrieved when the storm begun. Therefore a rig was designed which could be deployed and retrieved irrespective of the tide time and sea state. The design made use of a tall 'mast' over 3.5 m long which could be used to push the rig out in a horizontal configuration. Once the rig was in position the mast was pushed vertical thereby 'flipping' the whole rig through 90°. This enabled the experimenters deploying the rig to stand in shallower water than the eventual measurement site. Once deployed the rig was held in position by some short lengths of scaffolding that dug into the sand and acted as anchors holding the rig stationary during measurements. The mast acted as a convenient position for a marker buoy and also was used to gauge the approximate depth of the transducers. During the measurements made for this trial it was estimated that the rig was in water approximately 3.5 m deep.

Upon retrieval a shore based winch was used to pull on a rope attached to the top of the mast. This provided a large amount of leverage sufficient to break any scaffolding bars out of the sand in which they had become buried. The winch would then tip the rig horizontal again and the rig would roll out of the surf without any need for any experimenters to enter the water and hence could be safely undertaken at any time, irrespective of the tide. The marker buoy on top of the mast was used to prevent the top of the mast digging into the sand during retrieval. Figure 5.11 illustrates the design of the rig and its positions during deployment/retrieval and measurement.

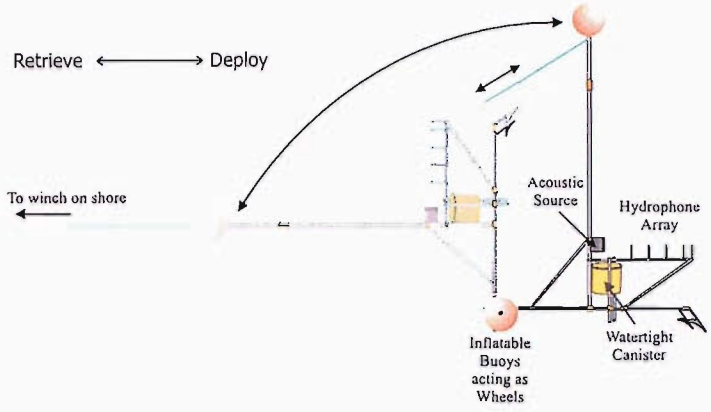

Figure 5.11: Schematic of rig design for the second sea trial [65]. The rig was wheeled down the beach in a horizontal configuration and into the water to a depth of approximately 2 m where it was flipped into a vertical configuration.

5.3.2 Experimental setup

Several different sets of apparatus for evaluating bubble population were fielded on the rig in an attempt to characterize the bubble population using multiple techniques. One passive technique and two active techniques were employed. The acoustic source (described in section 4.3) was securely mounted in front of the mast. The direct acoustic path between source and receiver was kept clear of any obstruction and the rig was designed in such a manner so as to ensure that the presence of the rig would cause minimal bias to the estimated bubble population. The signal transmitted by the source was a ten frequency pulse train using a pulse length of 500 μs (as described in section 4.1). The source level used was approximately 195 dB (re 1 μPa @ 1m).

A set of seven Bruel & Kjaer type 8103 hydrophones were positioned in a 'T' shaped array at a distance of 1.65 m from the source. Five of these were positioned along a straight line in order to take inversion data (although owing to software problems experienced during the trial only 4 hydrophone signals were acquired) and were spaced at 0.15 m intervals. The spacing was determined by the typical size of oceanic bubble formations which is O(10)

Figure 5.12: Photograph of the hydrophone array used in the second sea trial. One of the experimenters (Mr. Yim) makes final adjustments to the rig prior to deployment. Note the wire gauze around each hydrophone to protect it from impact with wave-borne stones. Also to the right of the image the edge of the acoustic source and water-tight canister can be seen. In the background the 200m (blue) umbilical cable has been paid out ready for deployment.

cm [21]. The first of these hydrophones was positioned on-axis at 1.65 m from the face of the acoustic source. This distance was assessed to be in the far field of the source (see section 4.3), hence plane wave propagation could be assumed.

The final two hydrophones were positioned off-axis for use in the triangulation of bubble positions from passive emission data. The cables for all the hydrophones were run inside the scaffolding tubes to protect them from any damage before passing into the instrumentation canisters via water-tight glands. The signals from the hydrophones were then passed up a 200 m armoured cable (as described in section 4.4.2) for acquisition.

Since the beach at Hurst Spit is composed of shingle it was deemed necessary to protect the hydrophones from impact with any wave-borne stones. To this end each hydrophone was protected by a wire mesh. The mesh chosen had a thin gauge and gaps of approximately one centimetre (see figure 5.12). While it was accepted that this would have some impact on the performance of the hydrophones it was deemed necessary rather than risk damage to these delicate instruments.

The effect of the gauze was investigated in bubble-free water in the laboratory by measuring the attenuation across the array with and without the gauze in place. Figure 5.13 shows ten measurements of the excess attenuation caused by the presence of the gauze. As can be seen the measurement was extremely repeatable with all ten curves overlying each other. A peak in the attenuation exists around 70 kHz, where the wave length corresponds to the dimension of the gauze wrapped around the hydrophone. At higher frequencies the attenuation increases as the wavelength shortens. However, the attenuation measured in this trial is the *excess* attenuation caused by the presence of bubbles. Since this was calculated from the ratio of bubbly to bubble-free measurements, the effect of the gauze is accounted for as the bubble-free calibration was performed with the gauze in place. Therefore any increase in attenuation can be attributed to the presence of bubbles.

Finally a 1 MHz receiver and emitter were placed with their beam-

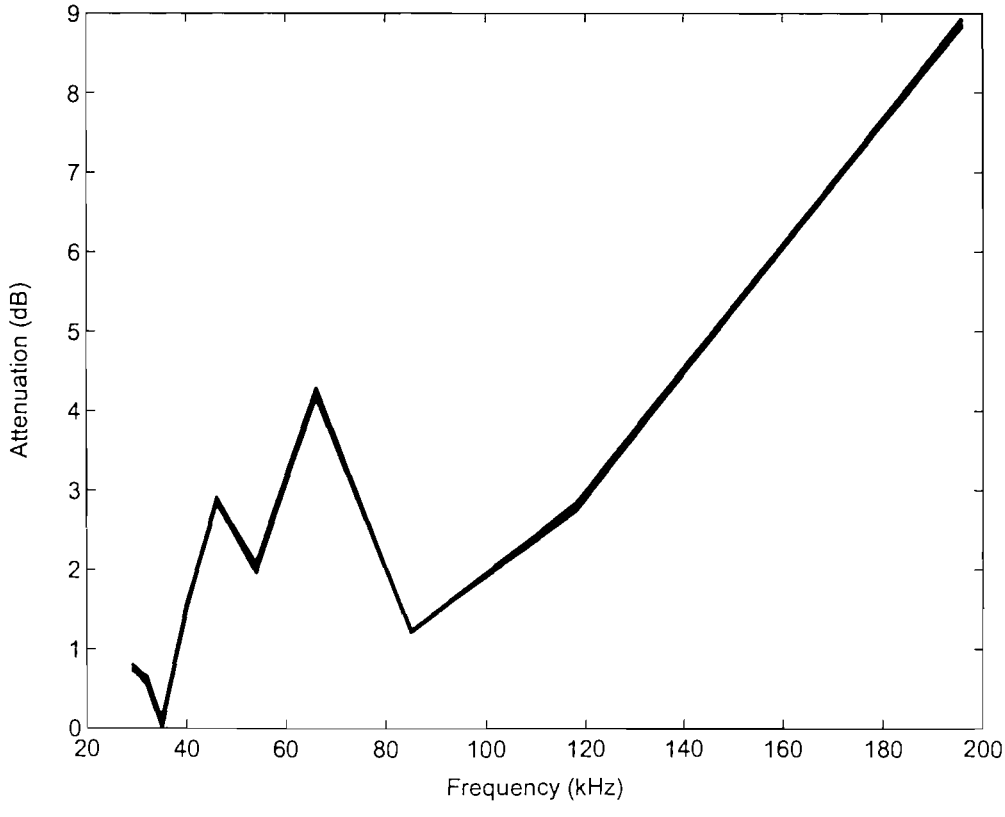

Figure 5.13: Attenuation caused by the presence of the wire gauze around the hydrophones. Ten measurements were taken over a path length of 45 cm and proved extremely repeatable (all ten measurement overlay one another). Since the bubble-free calibration was performed with the gauze in place, its effect is accounted for in any measured attenuation.

patterns overlapping the main lobe of the acoustic source with which to collect combination frequency data. Unfortunately no populations have been estimated from the passive and combination frequency techniques therefore no comparison with any inversion result is possible. The electronics, signal generation and data acquisition used for the inversion measurement were as given in chapter 4. The configuration of the acoustic transducers is shown in figure 5.14.

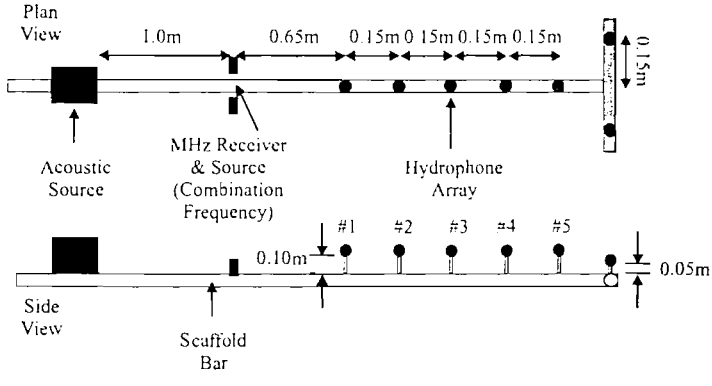

Figure 5.14: Schematic diagram of experimental apparatus used in the second sea trial. Multiple methods were used in an attempt to characterize the bubble population using multiple acoustic methods.

5.3.3 Initial data check

Initial data analysis revealed that cross-talk between the driving and the received signal had affected the data. This was because the 200 m umbilical cable was carrying both the driving and received signals and the driving signal was being amplified on shore before being transmitted to the rig. This high power signal induced a signal in neighbouring channels despite the use of screened twisted pair channels and the push-pull amplifiers described in section 4.4.2. However, this did not prevent analysis of the data because the interference only occurred while the driving signal was being transmitted. Because of the separation of the source and receivers, the acoustic pulse did

not arrive at the first receiver until approximately 1 ms after the transmission of the pulse. Therefore the received signal (500 μs pulse length) used in these experiments was un-corrupted. However some other experiments taken during this trial used pulse lengths greater then 1 ms and hence the cross-talk and received signal interfered. This is illustrated in figure 5.15 which firstly shows a 500 μs pulse length (as used in these inversion experiments) where the effect is easily removed by simple windowing and secondly with a longer pulse (as used in other experiments) where cross-talk and received signal interfere. Since the cross-talk and the received signal will have predominantly the same frequency content it is expected to be extremely difficult to separate these two phenomena.

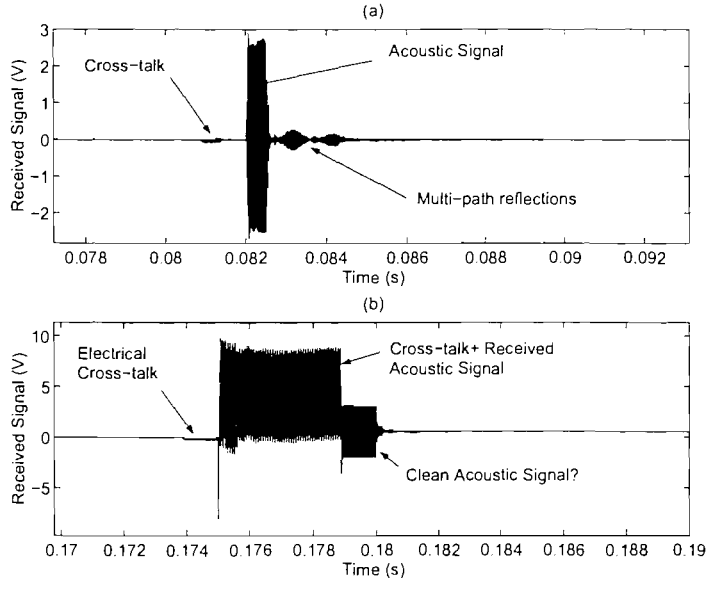

Figure 5.15: Illustration of received cross-talk interference between transmit and received channels (a) Pulse duration = 500 μs, here the pulse duration was less than the travel time to the first receiver therefore cross-talk could simply be windowed out (b) Pulse duration = 5 ms, here cross-talk interferes with received signal making analysis difficult or impossible. Data suffering from cross-talk was not used in this study.

5.4 Summary

Making scientific measurements in an environment as hostile as the surf-zone is a challenge in itself. This chapter has outlined two trials and showed the line of development of apparatus suitable for use in such an environment. The first sea trial was undertaken in extremely difficult conditions and collection of any data at all can be viewed as a success in such a harsh environment. The second trial learned many lessons from the first and consequently met with considerably more success. The chapter has outlined the experimental setups used in both trials and the environmental conditions encounter. The analysis of the data collected during these trials is presented in the next chapter.

Chapter 6

Analysis of sea trial data and discussion

This chapter analyses and discusses the data collected during the two sea trials described in chapter 5. The results from the first sea trial are only analysed using linear methods (see chapter 2) as the sound pressure used was not expected to be sufficient to excite any nonlinear behaviour. The second trial is analysed using both linear and nonlinear (chapter 3) methods and the results obtained are compared and discussed. In all cases the inversions are based upon either the linear or non-linear extinction cross section.

6.1 First sea trial: Hurst Spit 2000

During the successful third deployment of the first sea trial (see section 5.2.3) attenuation was measured by the backscatter from an air-filled buoy positioned 2.35 m away from a mono-static acoustic source. Owing to the bandwidth of the source, measurements were confined to small bubble radii (8.5 - 16.5 μm). However, this is a region of high interest since it is close to a previously reported peak in the oceanic bubble size distribution [20, 39, 45]. Sixteen sets of measurements were made, each consisting of ten individual measurements of the bubble population. During the trial extremely calm

conditions (wind speed < 0.5 m/s) were initially experienced and it was not until the final six sets of measurements that the wind speed increased (up to 7 m/s) causing significant bubble populations to be measured.

The extended period of calm conditions was used to perform a measurement of the attenuation experienced in a nominally bubble-free environment. The average of ten measurements taken in these conditions was then subtracted from all following measurements and to account for geometric spreading and other 'systematic' effects. Any excess attenuation was then attributed to the presence of bubbles. This assumption could be compromised by the fact that the more turbulent conditions that will accompany bubble activity in the surf-zone is likely to cause a greater quantity of suspended sediment to be present in the water column. However, the sediment is acoustically less active than the bubbles when both are found in concentrations that could be expected in the surf zone [76]. The sediment can be expected to make a negligible contribution to the attenuation over the short measurement distance used. This can be seen by calculating the attenuation imparted by a suspension of sand particles (the seabed type at the measurement position, see figure 5.2) over the frequency range of interest, using the technique described in [77]. Modelling the suspension as a Gaussian particle size distribution with a mean diameter of 70 microns and a standard deviation of 10 microns (with minimum of 10 microns and maximum of 120 microns) gives the normalised attenuation shown in figure 6.1. This shows that a concentration of suspended sediment in excess of 30 kg/m^3 would be required to give a peak attenuation of 1 dB/m. Estimates of sediment concentrations are typically less than 1 kg/m^3 [78] but could be expected to peak at 10 kg/m^3 [79] in the surf zone.

Figure 6.2 shows the average attenuation measured during three of the final sets of ten measurements. As the wind speed increases so does the attenuation. The wind speed rose from 0.5 m/s to 7 m/s through the course of the tests. It is of interest to note the large increase in attenuation at 7 m/s. This is around the speed observed by Thorpe and others [50,80] where

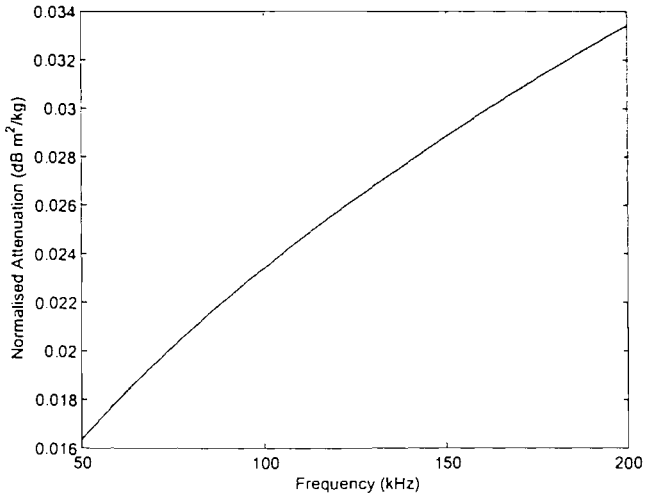

Figure 6.1: Normalised attenuation resulting from a Gaussian size distribution with properties similar to that of sand. *Acknowledgement: Dr. Simon Richards, QinetiQ Ltd.*

bubbles are generated in large quantities in the open ocean.

Figure 6.3 shows three single populations taken from each of the three sets of measurements described above. The data has been scaled to adjust the bin size in which the bubbles are reported to the standard 1 μm. During the measurements the height of the breaking waves varied from approximately 10 cm to in excess of 1 m. The air temperature varied between 8°C and 14°C and the water temperature was constant at 11°C. Measurements were taken at random times throughout the wave breaking cycle. It is of interest to note that no peak is apparent in the bubble size distributions shown in figure 6.3. Previous investigators [43, 45] have noted a peak the bubble population at approximately 20 μm. However both of these measurements were made in open ocean rather than the surf-zone and it may be the case that the different dynamics experience by the bubbles in the surf-zone alter the balance between buoyancy and dissolution that is thought to contribute to the peak in the open ocean data.

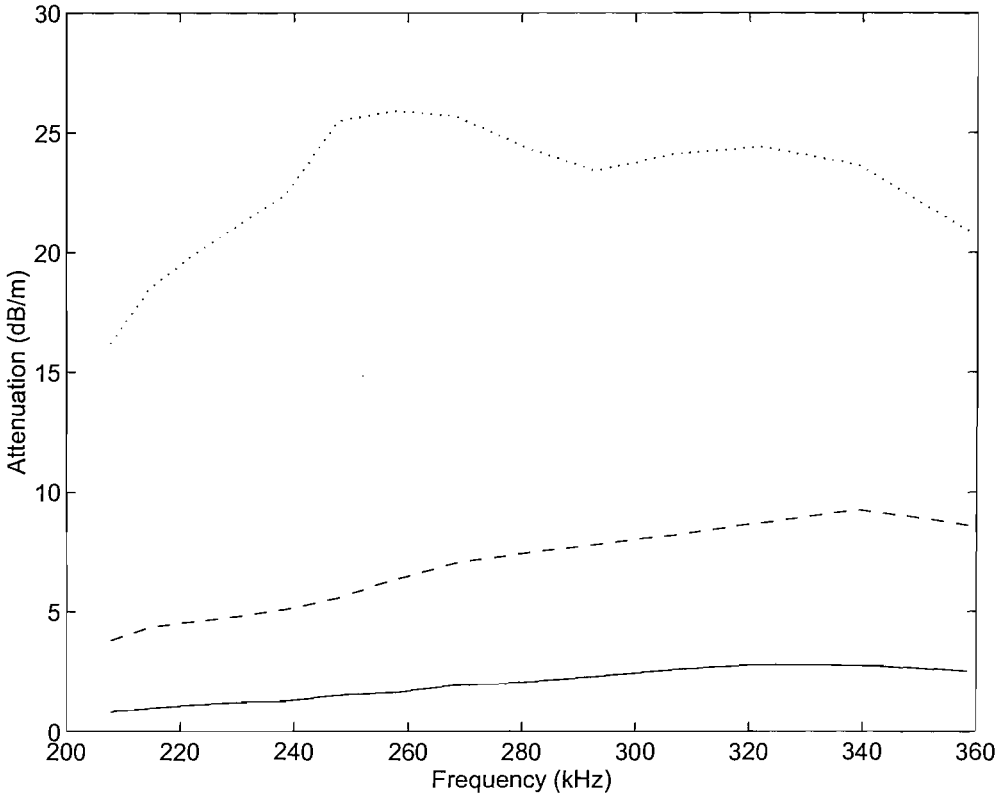

Figure 6.2: Average attenuation measured during three sets of ten measurements. Measurements taken on the 15th November 2000 at 1350h - wind speed 5.5 m/s (solid), 1510h - wind speed 6 m/s (dashed) and 1610h - windspeed 7 m/s (dotted).

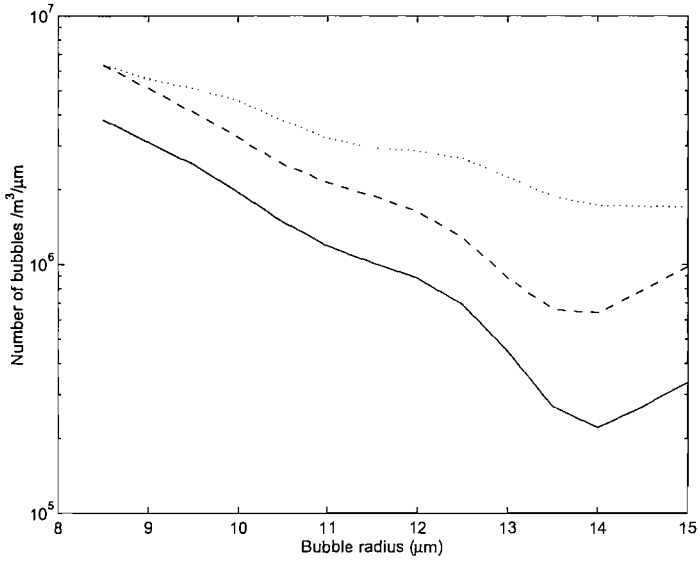

Figure 6.3: Computed bubble size distributions in the range 8.5 to 15.5 μm. The solid, dashed and dotted lines correspond to single measurements taken during the three sets of measurements described in the caption to figure 6.2.

Figure 6.4 plots the average population measured during the trial (with errorbars showing the minimum and maximum values measured in each radius bin) plot alongside other historical populations. Two other surf zone measurements are shown. Phelps *et al.* [6] used an acoustical technique exploiting combination frequencies to make measurements at four radii between 37 and 150 μm. This measurement was made on the North Yorkshire coast in water approximately 3 m deep with wind speeds of 11 m/s and wave heights of in excess of 2 m. Deane & Stokes [44] deployed an optical technique at Scripps Pier in California. They made measurements at larger bubble radii than the other (acoustical) techniques shown. The open ocean population measured by Johnson & Cooke [46] was obtained using optical methods in water of 20-30 m depth with wind speeds of 11-13 m/s. It is of interest to note that this population shows a lower number of bubbles at small radii compared to the other measurements. This may be caused by larger bubble obscuring smaller bubbles. The population measured by Farmer & Vagle was

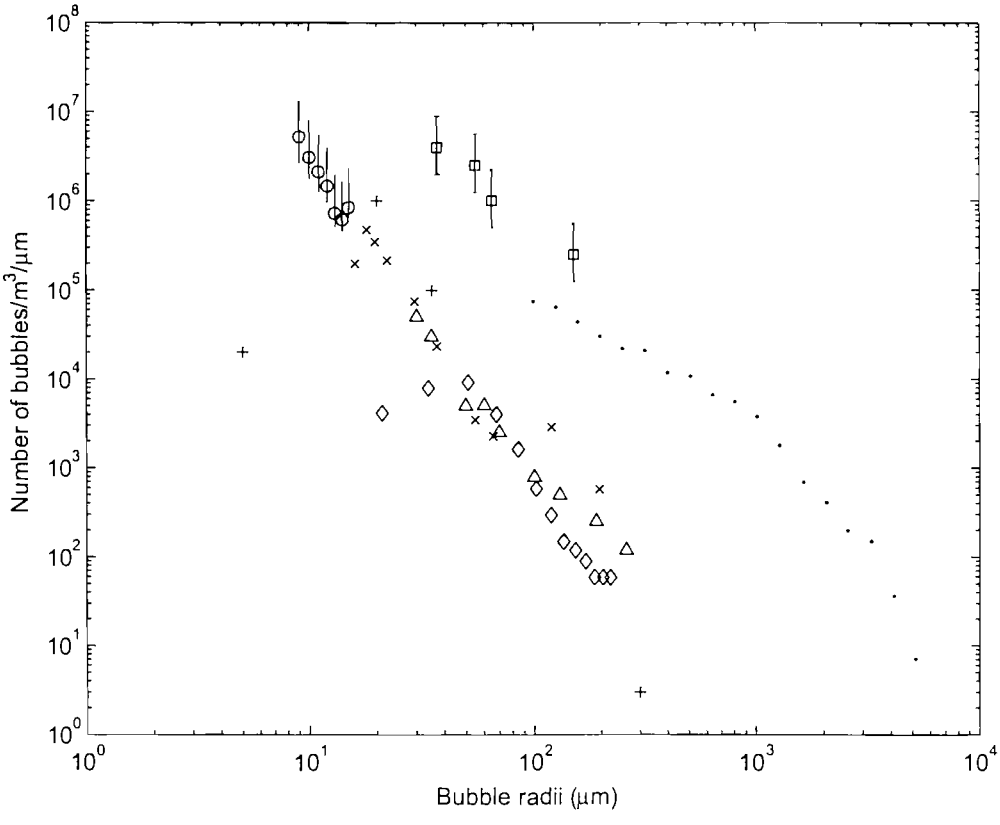

Figure 6.4: Average bubble populations estimated during the first sea trial compared to historical data. The data collected during the first sea trial (circles) is plotted along with errorbars to indicate minimum and maximum values. The data is compared to historical data including: surf-zone data collected by Phelps *et al.* [6] with errorbars indicating uncertainty due to the sampling volume (squares), Deane & Stokes [44] (dots) and open ocean data collected by Farmer & Vagle [43] (plus signs), Breitz & Medin [38] (triangles), Johnson & Cooke [46] (diamonds) and Phelps & Leighton [45] (crosses).

in extremely deep water (4 km) and used a upward looking sonar to measure backscatter from surface bubble plumes. The wind speed during this measurement was 12-14 m/s. Finally Breitz & Medwin [38] used a resonator system to make measurements in water 120 m deep with wind speeds of 12-15 m/s. It should be noted that the absolute number and the gradient of the new surf-zone measurements are similar to the open ocean measurements.

However, the data shown here should be treated with caution, since the bandwidth of the acoustic source meant that the bubble size distribution could only be estimated over a small portion of the full spectrum. Therefore the measurement may be affected by the presence of bubbles outside this range which are not accounted for in the estimate. The next section will analyse the data collected during the second, more successful, sea trial.

6.2 Second sea trial: Hurst Spit 2001

As discussed in section 5.3 the second sea trial was considerably more successful than the first. A wideband (30 - 200 kHz), high amplitude (195 dB re 1 μPa @ 1m) transducer was employed along with an improved rig design that allowed simple deployment and retrieval of the apparatus. This allowed successful measurements to be made across a broader spectrum of bubble radii at an amplitude that might excite bubble nonlinearities. Signals were received using seven Bruel & Kjaer 8103 hydrophones. Unfortunately, technical difficulties experienced with the LeCroy oscilloscopes during the trial meant that a backup system (a National Instruments 6110E DAQ card, see figure 4.11) had to be used to acquire the data. This limited the data acquisition to the four hydrophones closest to the source. These difficulties prevented data being taken through the majority of the single day trial but once they had been resolved data was successfully collected between 1500h and 1600h before retrieval of the rig.

Prior to the sea trial the apparatus was calibrated in an 8 m by 8 m by 5 m deep concrete walled tank containing bubble-free water (see section 4.2).

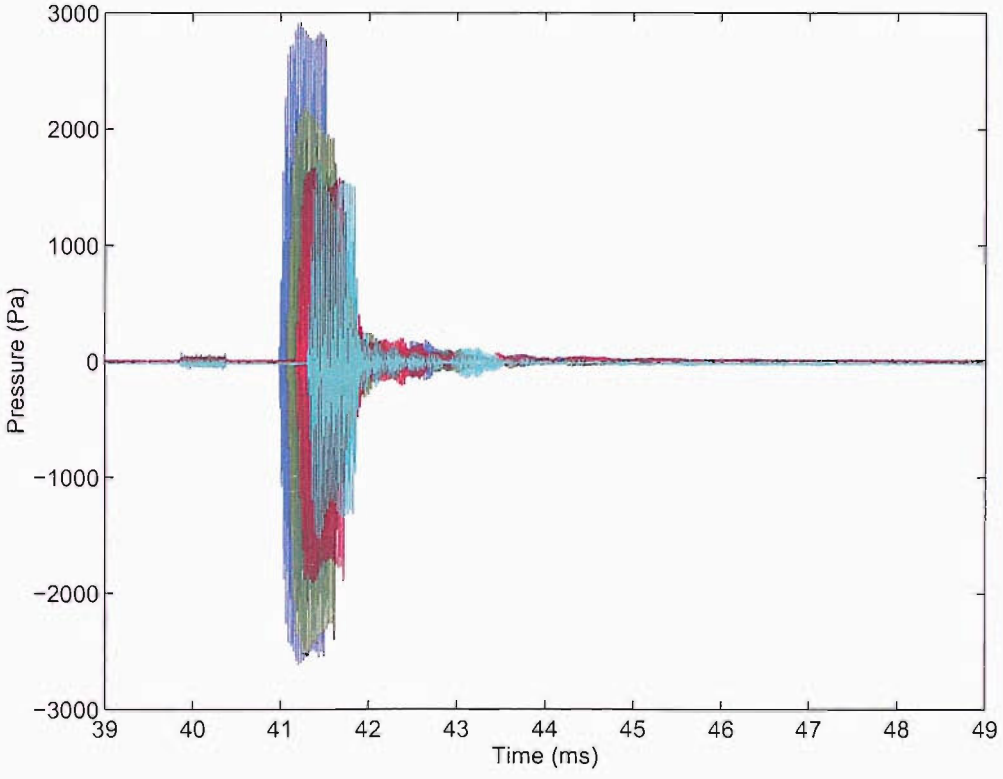

Figure 6.5: The signal received from the four hydrophones as a single pulse (part of the ten pulse 'train') propagates over them. Note the arrival times of the pulses at each of the individual hydrophones and the period of cross-talk proceeding the pulse.

As discussed above any increase in attenuation in the oceanic environment was then attributed to the presence of bubbles. Figure 6.5 shows the signal received from the four hydrophones as a single pulse from the 'train' of ten pulses propagates past them. It should be noted that because of the electronics required to transmit the signal along the 200 m umbilical cable, the sensitivities used to convert voltage to pressure are not absolute and hence caution should be exercised when comparing the amplitudes of the signals. Attenuation is calculated by using equations 4.2 and 4.3 and which circumvents the need for an absolute calibration. Figure 6.6 shows a sample of the attenuation measurements made during the trial. As can be seen, due to the relatively calm conditions experienced, the attenuations measured are comparatively small, less than 15 dB/m. Attempting to accurately measure these values over the small path length between the individual hydrophones was considered impractical because of the low signal to noise of the measurement. In order to overcome this the attenuation was measured between the first and fourth hydrophones. This gave a total path length of 0.45 m, thus improving the signal-to-noise of the measurement.

Figure 6.7 shows the bubble populations estimated using the current state-of-the-art techniques outlined in chapter 2. Again the data has been scaled to adjust the bin size to the conventional 1 μm. During the measurements the rig was estimated to be in water of approximately 3.5 metres depth. The location of the rig was similar to the previous year (as marked on figure 5.3) and was slightly behind the breaking waves. The average air and water temperatures were 11°C and 8°C respectively. Average wind speed was 4 m/s from a SW direction. Samples of water were taken in sterile bottles for chemical analysis. This revealed that the electrical conductivity was 49.5 mS/cm, the pH was 8.07 and the salinity was 34.1 ppt. The void fraction of the bubble populations shown in figure 6.7 was calculated by linearly extrapolating the population in log space (omitting the largest three radii) from 10 μm to 300 μm. The average void fraction was approximately 5×10^{-6}.

Figure 6.8 adds the data collected during the second sea trial to the his-

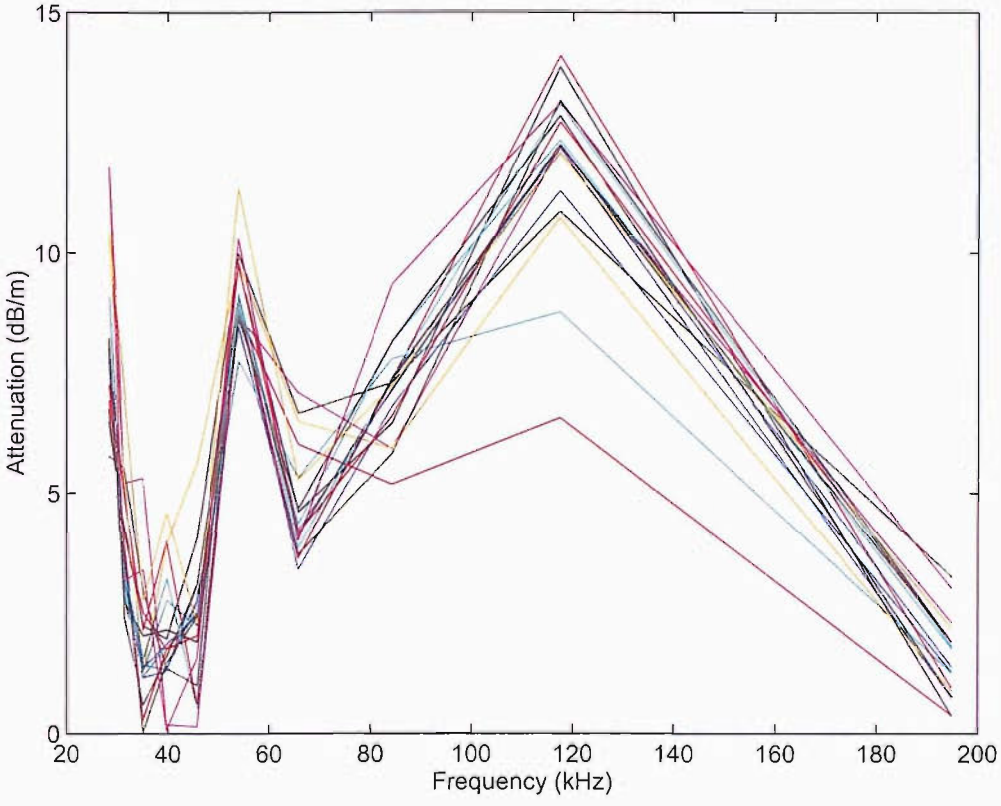

Figure 6.6: Measurements of attenuation made between the first and fourth hydrophones during the second sea trial. Each colour represents an individual measurement made between 15:20 and 16:00 GMT on 24-11-2001 (due to limitations of the available colour palette some colours are repeated).

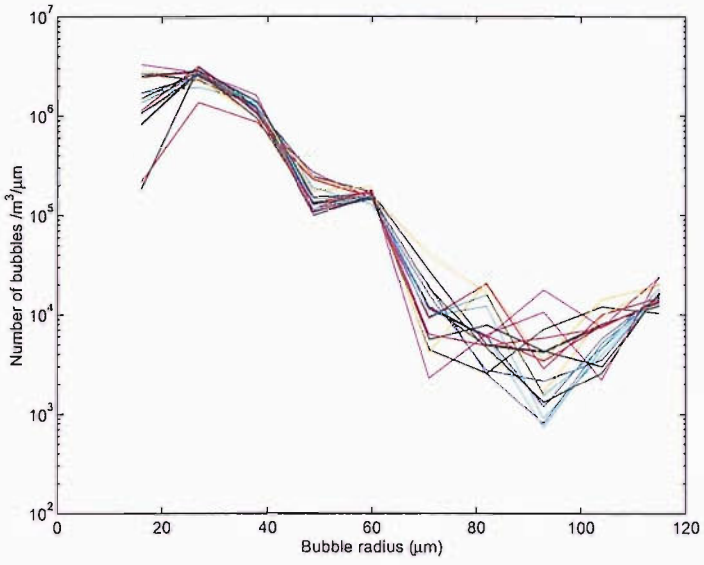

Figure 6.7: Linear estimates of the number of bubbles per cubic metre of sea water, per μm increment in radius made using the current state-of-the-art linear inversion. The colours correspond to the attenuation measurements shown in figure 6.6. The average wind speed during these measurements was 4 m s^{-1} from a south-westerly direction, the water temperature was 8°C and the air temperature was 11°C. The electrical conductivity was 49.5 mS cm^{-1}, the pH was 8.07 and the salinity was 34.1 ppt.

torical data plotted in figure 6.4. As can be seen in the figure the number of bubbles is slightly greater than the open water populations but considerably less than the surf-zone population measured by Phelps & Leighton [45]. This is in keeping with the relatively calm conditions experienced during the second sea trial. Several features in the data are apparent. Firstly the position of the peak in the distribution. Previous open ocean measurements [43, 45] have reported a peak in the distribution around 20 μm. In the new, surf-zone measurement the peak in the data is at 27 μm. However, the radius bin size used during the experiment was 11 μm and hence the true peak in the distribution lies in the range 21.5 μm to 32.5 μm. In any case it is not surprising that in the surf-zone the peak in the size distribution lies at a different radius.

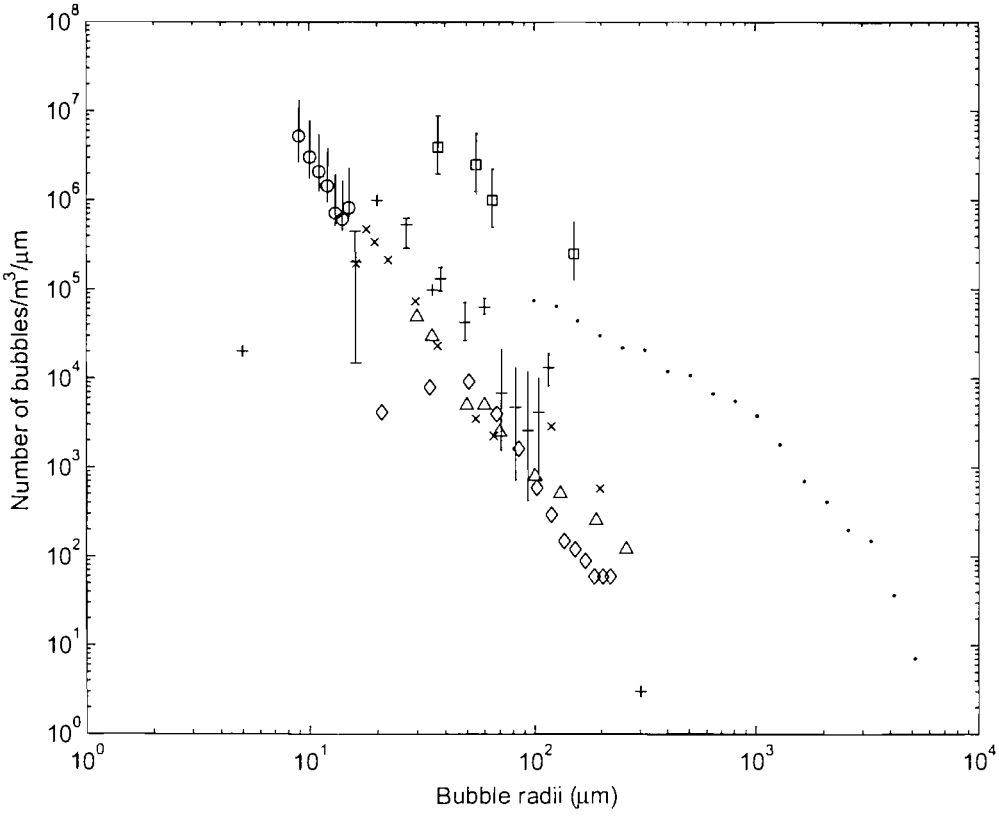

Figure 6.8: Average bubble populations estimated during the first sea trial compared to historical data. The data is plotted as in figure 6.8 with the addition of the mean estimate of the bubble population from the second sea trial (horizontal bars). The error bars indicate the minima and maxima of the measurements.

The position of the peak is determined by the balance between the rate at which bubbles are removed from the water column by dissolution of gas and buoyancy. In the surf-zone the turbulent forces caused by breaking waves must also be considered in this balance and hence may shift the position of the peak. The presence of a peak in the data was not apparent in the data collected during the first sea trial. Two possible explanations may exist for this: 1) the peak existed during the first sea trial but was at a radius outside the range of bubble radii assessed or 2) the peak existed within the measured radii but was obscured during the inversion process due to the small radius range of the measurement.

Secondly the small peak in the distribution at 60 μm and the rise in the bubble numbers above 93 μm. Examination of figure 6.6 reveals similar trends in the raw attenuation data at the corresponding frequencies. This indicates that these features are not products of the inversion process but are either related to systematic errors in the measurement system or are representative of the actual population. It should be noted that while no other population displays a similar peak at 60 μm, a secondary peak is shown in the population measured by Phelps & Leighton [45] at 119 μm. Finally the wide errorbars on the new data (which show the maxima and minima of the measured data) can be attributed by the randomization of measurements within the wave-breaking cycle.

6.3 Nonlinear analysis

Having performed the current state-of-the-art (linear) analysis on the data collected during the second sea trial, a comparison will now be made between the results already achieved and those obtained using the nonlinear techniques outlined in chapter 3. The matrix of bubble responses was recalculated using the nonlinear extinction cross section based upon pressure-volume loops as described in section 3.2. This calculation was extremely computationally intensive since a numerical solution to the Herring-Keller

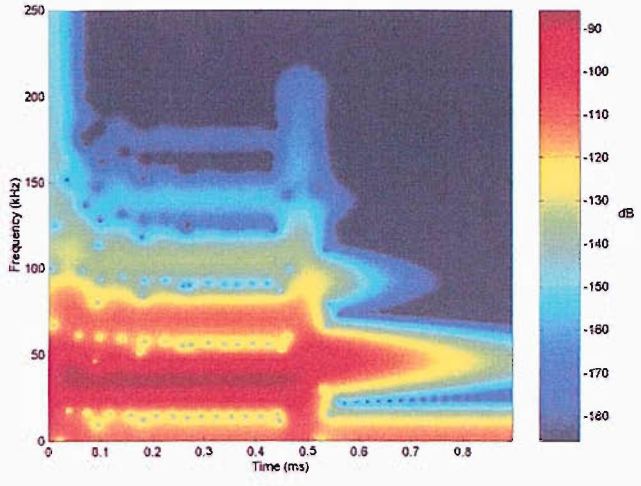

Figure 6.9: A spectogram plot of power spectral density (arbitrary reference) calculated for the radius time history of a 106 μm bubble being driven at 30987 Hz and 7.95 kPa. Significant energy is present at higher harmonics, indicating a departure from the monochromatic, linear regime. The drive frequency, which is close to the bubble fundamental during steady-state (200-500 μs), is lower than the bubble pulsation natural frequency, which can be seen both during ring-down (>500 μs) and the transient period.

equation (equation 1.34) had to be found for each element of the matrix. Because of this two simplifying assumptions were made. These were, that the all the bubbles were driven by the same pressure amplitude i.e. the medium was modelling using a single layer, and that the bubbles responded at steady-state. Despite these simplifications a small (ten-by-ten) matrix still took over 24 hours to calculate using a 1 GHz Pentium IV PC with 512 MB of RAM. Neither of the assumptions made are inherent in the technique.

Figure 6.9 shows the frequency response of a 106 μm bubble driven close to resonance by the peak sound pressure level used during the trial (7.95 kPa). As can be seen the response is non-monochromatic and therefore some difference between linear and nonlinear estimates of the bubble population might be expected. Despite this violation of the assumption of monochro-

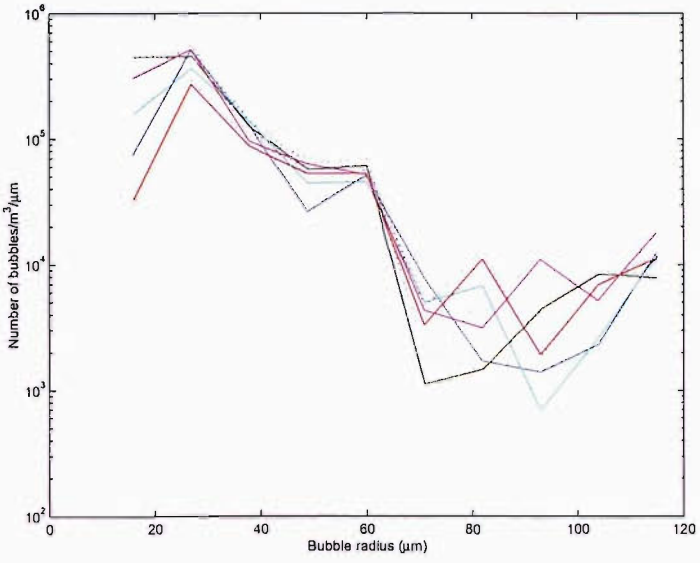

Figure 6.10: Linear and nonlinear estimates of the number of bubbles per cubic metre of sea water, per μm increment in radius. Each colour corresponds to the appropriate attenuation measurement in figure 6.6 (for clarity a subset of the data is shown). For a given colour, the dotted curves show the bubble population obtained by applying the state-of-the-art inversion to the acoustic data. The solid curve of the same colour show the population obtained when the same acoustic data is inverted using the new theory. Hence the solid curves present, for the first time, bubble populations obtained by an inversion which does not assume linear monochromatic conditions. The void fractions are around 5×10^{-6}.

matic linearity, the bubble populations estimated using both linear and nonlinear methods show little difference (see figure 6.10). This indicates that the driving pressure used (7.95 kPa zero-to-peak) was insufficient to cause a significant difference between the two estimates of bubble population.

The effects of increasing the amplitude of the driving signal are illuminating and illustrate the potential benefit that can be gained by including bubble nonlinearity in an estimate of bubble population. A single bubble population, calculated using the linear kernel, was used as the basis for the

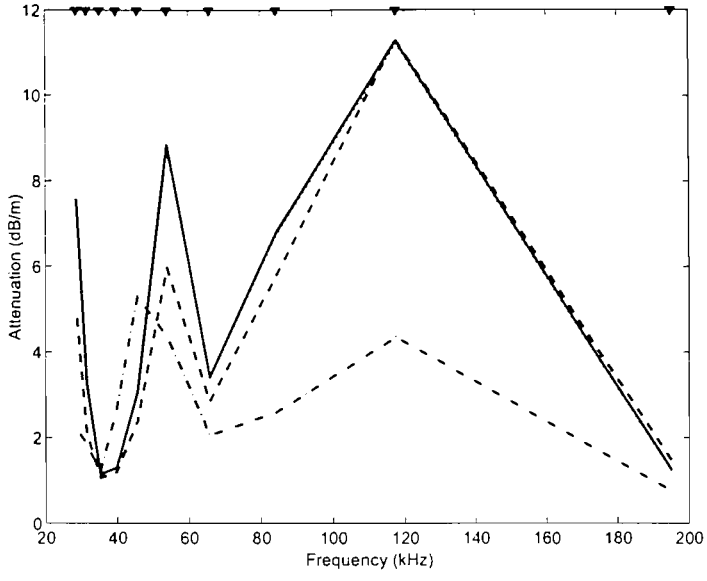

Figure 6.11: Steady-state attenuation calculated using a single bubble population taken from figure 6.7 as a basis. The calculation is performed using the linear formulation of Commander & Prosperetti (solid line) as well as the new nonlinear formulation assuming different driving pressures; 100 Pa (dotted), 20 kPa (dashed) and 50 kPa (dash-dot). The 100 Pa nonlinear solution (dotted) almost overlies the linear solution (solid). Note that the lines do not imply data across a continuum of frequencies: the calculation is performed at the ten specific pump frequencies used in the experiment (indicated by arrows at the top of the figure). Since these frequencies were chosen to give even point spacing in radii, the spacing of points is sparse at high frequencies.

calculation of attenuation. This linearly calculated attenuation was then compared with attenuations calculated using the new, nonlinear kernel, making the assumption that the driving pressures were 100 Pa, 20 kPa and 50 kPa (zero-to-peak). Linear mathematics would predict that the attenuation is independent of the driving amplitude. Figure 6.11 shows that the low amplitude, nonlinear solution is indistinguishable from the linear solution. However, as the driving amplitude increases the attenuation experienced by the pressure wave decreases. These higher amplitudes are easily achievable

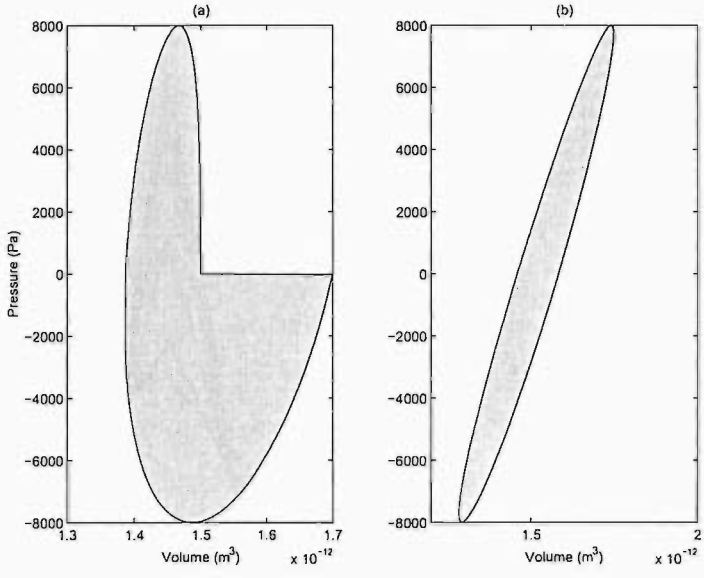

Figure 6.12: A sixty micron bubble driven by a semi-infinite pressure wave. (a) The approximation to the contour integral shortly after the onset of oscillation and (b) evaluation of the contour integral during steady-state oscillations.

by many commercial and military ocean acoustic systems [3]. Examination of the figure shows that nonlinear effects begin to become significant with driving pressures in excess of 10 kPa and it is at these pressures that the calculation of the nonlinear effects becomes increasingly important. If higher driving pressures tend to produce lower-than-expected attenuations, the bubble population inferred by a purely linear system may be an underestimate.

In addition to the amplitude dependency shown above, the new technique is also capable of indicating time dependent effects. A similar process to that described above was used, whereby a single bubble population taken from figure 6.7 was used as the input into a forward problem which was then solved using the nonlinear technique. In order to incorporate the time dependent element, the bubble cloud (again treated as a single layer) was exposed to a semi-infinite driving pulse. The contour integral formed by each consecutive pressure-volume loop was summed before dividing by the number of loops undertaken in order to determine the average extinction

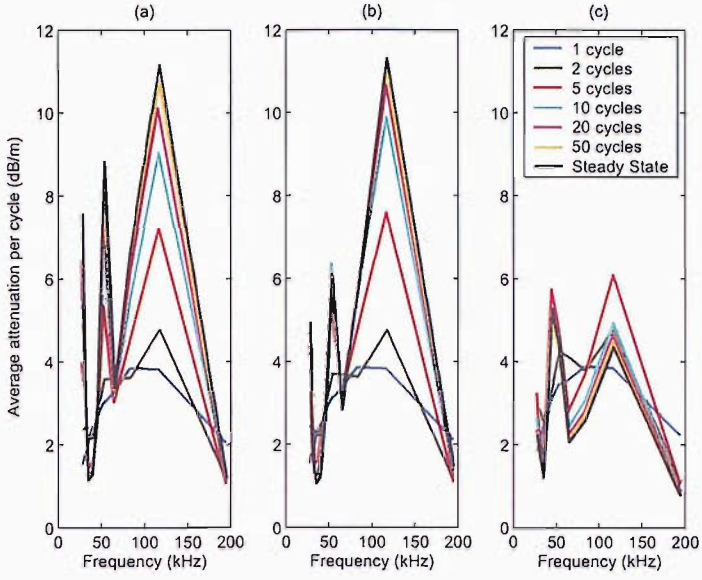

Figure 6.13: Averaged attenuation per cycle calculated for different pulse lengths and amplitudes. Each graph shows the effect of increasing pulse length for a fixed driving amplitude. Note that as the pulse length increases the attenuation tends toward the steady state solution of figure 6.11 (black line). The driving amplitudes used are (a) 100 Pa (b) 20 kPa and (c) 50 kPa. As with figure 6.11 the data are plotted at ten discrete frequencies corresponding to a linear spacing of bubble radii and hence there are few data points at high frequency.

cross section per cycle as a function of the number of cycles. Shortly after the onset of oscillation, where, due to the erratic behaviour of the bubble, closed loops are not formed, the contour integral was approximated by closing the loop with a straight line (see figure 6.12(a)). Such approximations are minimized during the steady state period of oscillation (figure 6.12(b)).

In order to explore fully the behaviour both as a function of time and amplitude the time-dependent forward problem was solved for three driving pressures used above, at a range of pulse durations. The results are shown in figure 6.13 and shows, as expected, that as the number of cycles increases the attenuation tends towards the steady state solution shown in figure 6.11.

More detailed examination of the data indicates some interesting effects. The attenuation experienced by a 1 or 2 cycle pulse is low and is largely unaffected by the amplitude of the pulse. The low amplitude (100 Pa) data shows a steadily increasing attenuation from the very short pulses to the steady state solution. Qualitative examination of the 20 kPa data seems similar to the 100 Pa data, however it should be noted that the solution converges to the steady state in a fewer number of cycles. The behaviour of the 50 kPa data is more complex, and shows less dependence upon number of cycles. The maximum attenuation is experienced by a five cycle pulse and, in this case, the steady state solution shows the least attenuation at many frequencies. Such investigations are of interest in a number of applications and have been the subject of previous investigation [81 83]. However, as no data has been collected to support such pulse length calculations they are included here primarily to illustrate how time dependence may be included in the new technique.

As discussed in section 2.3.2, in bubble clouds with high void fraction (a scenario in which high amplitude pulses might be used) interactions between bubbles can become important. In order to assess the magnitude of this effect in bubble clouds of sufficiently high void fraction to necessitate the use of high amplitude pulses, one of the populations from figure 6.7 has again been selected for further analysis. In this case, the population has been scaled from its original void fraction of 5×10^{-6} to void fractions of 1×10^{-5}, 1×10^{-4} and 1×10^{-3}. Figure 6.14 shows the attenuation calculated from these scaled populations using both the standard linear formulation (equation 2.3) and Kargl's effective medium equation (equation 2.39). As can be seen in the figure increasing the void fraction in excess of 1×10^{-4} would make measurements over path lengths O(1)m untenable. In this instance a short path length (O(0.1)m) between source and receiver would have to be used in conjunction with a high amplitude transducer with a short near/far field interaction to ensure plane wave propagation.

Consider a cloud of bubbles with a size distribution that imparts the at-

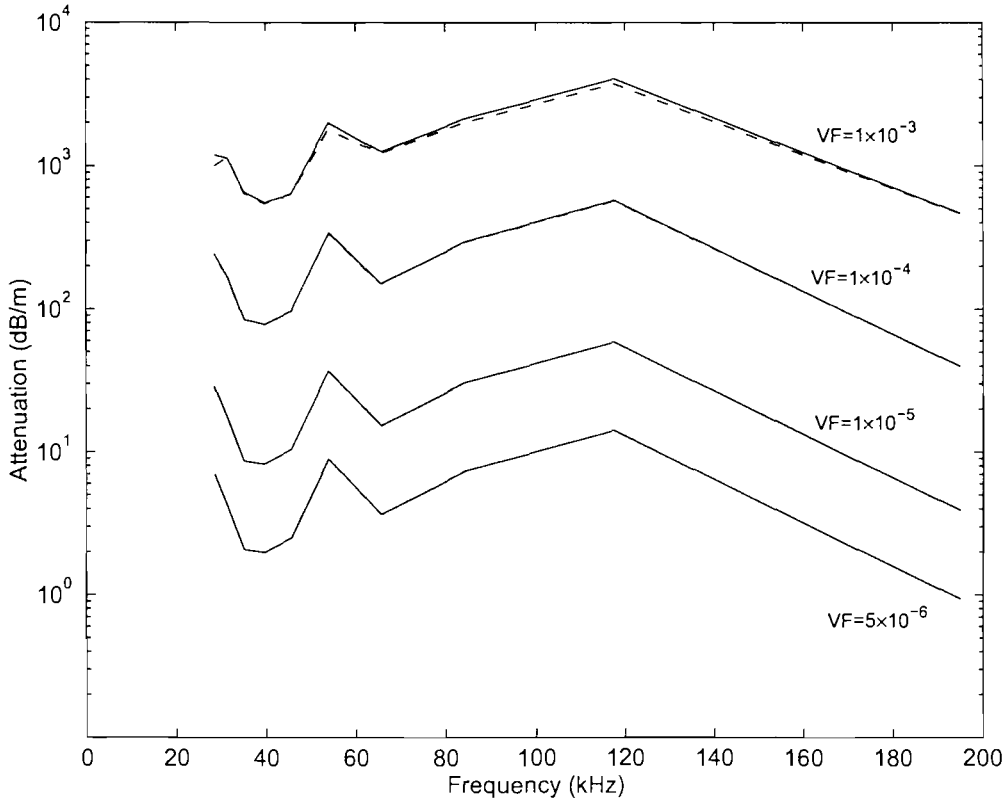

Figure 6.14: Attenuation predicted using both standard linear theory (solid) and Kargl's theory (dashed) that accounts for bubble-bubble interactions. A typical bubble population from figure 6.7 is scaled up to void fractions of 10^{-5}, 10^{-4} and 10^{-3}, and compared to the attenuation caused by the original void fraction (5×10^{-6}).

frequency (kHz)	Difference due to bubble nonlinearity (dB)	Difference due to bubble interactions (dB)
28.5	5.3	8.4
31.5	1.4	1.5
35.1	0.1	0.3
39.7	1.3	0.2
45.7	2.2	0.2
53.9	4.5	6.4
65.7	1.3	0.6
84.2	4.1	2.2
117.4	6.8	6.6
195.0	0.5	0.1

Table 6.1: The difference in attenuation due to bubble interactions and bubble nonlinearity for a cloud with a void fraction of 1×10^{-4} driven by a 50 kPa plane wave.

tenuation shown by the 1×10^{-4} curve in figure 6.14. Let us assume that the bubble cloud is excited by a plane wave with amplitude 50 kPa and that the attenuation through the cloud is calculated using the standard linear formulation. The relative importance of bubble interactions and bubble nonlinearity can be assessed by the difference between that attenuation and either the attenuation calculated using the Kargl's equation or the new nonlinear formulation respectively. As can be seen in table 6.1, at this driving pressure the magnitudes of the two effects are similar. However, for the surf zone data presented earlier in the chapter, both the void fraction and the driving pressure were below the threshold where such effects begin to become significant and thus these terms can safely be neglected.

Kargl's formulation of the effective wavenumber suggests, for the first time, a means of including the effect of bubble-bubble interactions in an

inverse estimate of the bubble population. The iterative approach used by Kargl requires knowledge of the bubble population in order that the radiation damping term may incorporate the effect of interactions. Therefore an iterative approach to the inversion could also be adopted with respect to the inverse estimate. The first pass would compute a population using the standard formulation of Commander & Prosperetti (equation 2.3). Subsequent passes would use the size distribution estimated during the previous pass as an input into Kargl's equation (equation 2.39). The iteration process would continue until the solution converged within an acceptable tolerance. Kargl's equation typically converges in less than ten iterations. Development of such a scheme is recommended as an area of future work.

It should not be thought that the use of bubble nonlinearity is only of benefit in cases of high bubble void fraction. The ability to excite and exploit time dependent nonlinear effects can be a valuable diagnostic tool in a wide range of fields, not just the estimation of oceanographic bubble populations. Other applications might included the enhancement of signals from biomedical ultrasonic contrast agents or the detection of solid targets (such as mines) in the surf-zone.

6.4 Summary

This chapter has presented the data from two sea trials carried out during the course of this study. Analysis of data collected during the first sea trial yielded the first ever estimate of the bubble size distribution at small radii in the surf-zone. This data was compared with other historical measurements. However, owing to the limited spectrum of bubble radii measured the result should be treated with caution. The second, more successful, sea trial yielded more estimates of the bubble population in the surf-zone across a much wider spectrum of radii. This initial analysis was all performed using the standard linear formulation described in previous chapters. The data was then re-analysed using the new nonlinear technique developed in chap-

ter 3. Unfortunately, the driving pressure (7.95 kPa) used during the trial was insufficient to cause a significant change in the estimated bubble population. The chapter then went on to demonstrate the changes in measured attenuation that would be expected for higher driving pressures and showed that the threshold where nonlinear effects begin to become important is 10 kPa. A demonstration of the capability of the new nonlinear technique to model time dependent effects was performed. However no supporting data was available to verify the results of the model. The relative importance of bubble nonlinearity and bubble interactions in very dense bubble clouds (where high amplitude pulses might be used) was assessed and it was shown that the magnitude of the two effects is similar in such circumstances. A scheme was suggested that would enable the inclusion of bubble interactions in a linear inversion based upon Kargl's equation. This is recommended as an area of further study. The chapter concludes by emphasizing that dense clouds are not the only reason for modelling bubble nonlinearity and briefly discussing some other techniques that may benefit from application of the principles described within this work.

Chapter 7

Conclusions and discussion

This study has successfully made measurements of the bubble population in the surf-zone. The measurements made here add to the very sparse set of measurements in this high-interest region. Of the other studies that have attempted to make surf-zone measurements [7, 20, 44, 45, 84] only Phelps & Leighton [45] and Deane & Stokes [44] have made measurements at distances of less than 100 m from the water-line (the active region in which these measurements were also made). Such measurements are of importance in areas such physical oceanography and underwater acoustics. For example knowledge of likely bubble populations is crucial in the design of systems to detect solid targets in the surf-zone.

As part of the process of designing a system suitable for surf-zone measurements, the key assumptions made in the current state-of-the-art theory were examined. This highlighted the need for a new, time dependent, nonlinear model. Initially an attempt to derive an expression for the nonlinear complex wavenumber was made, however this was shown to be flawed for a number of reasons. Further consideration of the problem gave rise to an expression of the nonlinear extinction cross section of a bubble in terms of the loci mapped out by pressure-volume curves. The new model makes no restrictive assumptions of steady state or linear oscillations and hence is expected to be suitable for use in a variety of problems. In the low amplitude

limit the nonlinear extinction cross section was shown to converge with its linear counterpart while high amplitude modelling exhibited the presence of higher harmonics which are unaccounted for in conventional techniques. One difficulty presented by the new technique is that it can be computationally intensive, as the nonlinear equations of motion involved typically require numerical solution. In this study the Herring-Keller equation was chosen as it imposes the fewest assumptions upon any solution. Even small kernels (10 by 10) took long periods to calculate. During this study it was decided to model the bubble cloud as a single layer with the consequence that all the bubbles in the cloud were assumed to be driven by the same pressure. This neglected the effect of 'layering' the bubble cloud and this is recommended as an area for future study. Such an approach would allow the impact of inhomogeneous bubble clouds to be assessed.

However, as computing power increases and more numerically efficient methods of solving the nonlinear equations are found, the problem of long computation times will decrease. A particular strength of the technique is that it is not specific to a particular equation to describe the response of the bubble. Therefore the most appropriate equation for a particular problem may be substituted in place of the Herring-Keller equation. An example might be in the use of echo-contrast agents in biomedical ultrasound [65]. If an equation of motion could be formulated for the volume of an oscillating bubble passing through a capillary vein (a situation in which free field conditions would certainly not apply) then that equation could be used as the basis for the extinction cross section. As can be seen, while the new model was formulated for the specific problem of measuring surf-zone bubble populations, it can be applied to a wide range of problems.

Unfortunately the new model was formulated in the midst of the preparations for the second sea trial (described in chapters 5 and 6). This meant that the necessary tools for evaluating the onset of the nonlinear response were not available when designing the acoustic source. As a consequence the driving pressures used in the trial were below the threshold where nonlinear

effects have been shown to become important. Laboratory work to experimentally verify the effects predicted by the model is recommended for future work. Such work should investigate the amplitude and time dependence of the attenuation through an artificial bubble cloud (as predicted in figures 6.11 and 6.13).

The effect of bubble interactions was assessed and was shown to become important at void fractions of around 1×10^{-4}. This corresponds with attenuations of O(100) dB and hence is a situation in which high driving pressures are likely to be required. Assuming a driving pressure of 50 kPa, the magnitudes of errors resulting from the neglect of bubble nonlinearity or bubble interactions were shown to be similar. A method of incorporating bubble interactions in a linear inversion was suggested and again is a recommended area of further study. Other areas of related research that may be of interest but have not been discussed in great detail include:

- The effect of over-determining the system of equations. In this study the kernel matrix has been square i.e. the number of frequencies was equal to the number of bubble radii under consideration. This is not a requirement for solution of the inverse problem and there may be benefit in basing the inversion upon a rectangular matrix.

- Singular value analysis of matrices of bubble response. Performing singular value decomposition upon the matrix of bubble responses enables the eigenvalues and eigenvectors of the matrix to be determined. Analysis of these values may provide valuable insights into the structure of the matrix and allow improved results to be inverted using it.

- A suitable method of measuring phase speed. No such method was found during the course of this study but might yield superior results to an attenuation based inversion due to improved resilience to noise. In addition the concept of complex valued kernels could be further investigated.

- An expanded set of surf-zone measurements across a broader range of bubble radii in a variety of surf-zone conditions would be a valuable addition to the sparse data from this important region.

- Further work on the use of broadband pulses, expanding on the work of Terrill & Melville [20], would be of benefit and may help investigate formation of bubble clouds.

- Consideration of the nonlinear, time-dependent response of a bubble may yield enhancements in the penetration of bubble clouds using active sonar. This would be of benefit in a number of applications.

- The use of nonlinear, time-dependent pulses may assist in distinguishing solid targets in the surf-zone from bubbles. Proposals for such exploitation of nonlinear effects have been made by Leighton [85].

- The ultimate aim of both of the trials conducted during this study was to attempt to characterize the surf-zone bubble population using a number of different techniques. This would provide independent verification of the measured size distribution and, since different techniques employ different assumptions, would allow the extent to which any of these assumptions have been violated to be assessed. Unfortunately in both instances only the inverse measurements detailed here were successful and hence no such checks could be performed. A fully successful experiment of this nature would be of significant interest.

This study has yielded a number of results that might be considered an advancement of the field. These include

1. A new nonlinear formulation of a bubble's extinction cross section.

2. The estimation of bubble populations in the surf-zone.

3. Application of a systematic method [49] of determining the optimal regularisation parameter to the inversion of matrices of bubble responses.

4. Assessment of the relative importance of bubble nonlinearity and bubble interactions.

5. An indication regarding the pressure threshold at which the affect of bubble nonlinearity becomes significant.

6. Some observations regarding effective deployment of apparatus in the extremely hostile conditions presented by the surf zone.

Such advances contribute to our knowledge and understanding of the estimation of the size distributions in bubbly environments and the propagation of sound through those environments. The primary motivator for these studies has been to enhance the understanding of oceanographic processes and also to provide the necessary science to enable the advancement of both military and commercial sonar systems. It is hoped, however, that the science laid down here may find many other applications in the increasingly diverse field of bubble acoustics.

Bibliography

[1] Munk, W. & Baggeroer, A. B., *The Heard Island Papers: a contribution to global acoustics*, J. Acoust. Soc. Am., 1994, **96**, 2327

[2] Stepnowski, A. & Mossynski S., *Inverse problem solution techniques as applied to indirect in situ estimation of fish target strength*, J. Acoust. Soc. Am., 2000, **107**(5), 2554-2562

[3] Urick, R. J., *Principles of underwater sound*, 1983, McGraw-Hill

[4] Siegenthaler, U., Sarmiento, J. L., *Atmospheric carbon dioxide and the ocean*, Nature, 1993. **365**(9)

[5] Leighton, T. G., *The Acoustic Bubble*, 1994, Academic Press

[6] Phelps, A.D., Ramble, D.G. & Leighton, T.G., *The use of a combination frequency technique to measure the surf zone bubble population*, J. Acoust. Soc. Am., 1997, **101**, 1981-1989

[7] Deane, G. B. *Sound generation and air entrainment by breaking waves in the surf zone*, J. Acoust. Soc. Am., 1997, **102**(5), 2671-2689

[8] Terrill, E. J., Lada, G. & Melville, W. K., Surf zone bubble populations. in 'Acoustical Oceanography' (eds. T. G. Leighton, G. J. Heald, H. Griffiths & G. Griffiths), Proc. Inst. Acoust., 2001, **23**(2), 212-219

[9] Farmer, D. M. 2001 Acoustic remote sensing near the air-sea interface. In *Acoustical Oceanography* (eds. T. G. Leighton, G. J. Heald, H. Griffiths & G. Griffiths), Proc. Inst. Acoust., 2001, **23**(2), 128-134

[10] Minneart, M., *On musical air-bubbles and the sounds of running water*, Phil. Mag., 1933, **16**, 155-210

[11] Medwin, H., *In situ acoustic measurements of bubble populations in coastal ocean waters*, J. Geophys. Res., 1970, **75**(3), 599-611

[12] Blanchard, D. C. & Woodcock A. H., *Bubble formation and modification in the sea and its meteorological significance*, Tellus, 1957, **9**, 145-158

[13] Foldy, L. L. *The multiple scattering of waves. I. General theory of isotropic scattering by randomly distributed scatterers*, Phys. Rev., 1945, **67**, 107-119

[14] Carstensen, E. L. & Foldy, L. L., *Propagation of sound through a liquid containing bubbles*, J. Acoust. Soc. Am., 1947, **19**(3), 481-501

[15] Medwin, H., *In situ acoustic measurements of microbubbles at sea*, J. Geophys. Res., 1977, **82**(6), 971-976

[16] Medwin, H., *Acoustical determinations of bubble-size spectra*, J. Acoust. Soc. Am., 1977, **62**(4), 1041-1044

[17] Commander, K. W. & Moritz, E., *Off-resonance contributions to acoustical bubble spectra*, J. Acoust. Soc. Am., 1989, **85**(6), 2665-2669

[18] Commander, K. W. & McDonald, R. J., *Finite-element solution of the inverse problem in bubble swarm acoustics*, J. Acoust. Soc. Am., 1991, **89**(2), 592-597

[19] Duraiswami, R., Sankar, P. & Chahine, G. L., *Bubble counting using an inverse acoustic scattering method*, J. Acoust. Soc. Am., 1998, **104**(5), 2699-2717

[20] Terrill, E. J. & Melville, M. K., *A broadband acoustic technique for measuring bubble size distribution: laboratory and shallow water measurements*, J. Atmos. Oc. Tech., 2000, **17**, 220-239

[21] Medwin, H. & Clay, C.S., *Fundamentals of Acoustical Oceanography*, 1997, Acedemic Press

[22] Commander, K. W. & Prosperetti, A., *Linear pressure waves in bubbly liquids: Comparison between theory and experiments*, J. Acoust. Soc. Am., 1989, **85**, 732-746

[23] Dumbrell, H. A. & Leighton, T. G., *Private communication*, 2000

[24] Morfey, C. L. *Dictionary of Acoustics*, 2000, Academic Press

[25] Plesset, M. S., *The dynamics of cavitation bubbles*, J. Appl. Mech., 1949, **16**, 227-282

[26] Noltingk, B. E. & Neppiras, E. A., *Caviation produced by ultrasonics*, Proc. Phys. Soc., 1950, **B63**, 674-685

[27] Neppiras, E. A. & Noltingk, B. E., *Cavitation produced by ultrasonics: theoretical conditions for the onset of caviation*, Proc. Phys. Soc., 1951, **B64**, 1032-1038

[28] Poritsky, H., *The collapse or growth of a spherical bubble or cavity in a viscous fluid*, in 'Proceedings of the first US National Congress on Applied Mechanics', 1952, New York, ed. E. Sternberg, 813-812

[29] Rayleigh, *On the pressure developed in a liquid during the collapse of a spherical cavity*, Phil. Mag., 1917, **34**, pp. 94-98

[30] Gilmore, F. R., *The growth or collapse of a spherical bubble in a viscous compressible liquid*, California Institute of Technology, Rep. No. 26-4, 1-40

[31] Akulichev, V. A., in 'High intensity ultrasonic fields', ed. L. D. Rozenburg, 1985, Plenum, New York, 239-259

[32] Herring, C. *Theory of the pulsations of the gas bubble produced by an underwater explosion*, 1941, OSRD, Rep. No. 236

[33] Keller, J. B. & Miksis, M., *Bubble oscillations of large amplitude* J. Acoust. Soc. Am., 1980, **68** 628-633

[34] Nigmatulin, R. I., Khabeev, N. S. & Nagiev, F. B., *Dynamics, heat and mass transfer of vapour-gas bubbles in a liquid*, Int. J. Heat Mass Transfer, 1981, **24**, 1033-1044

[35] Prosperetti, A. Crum, L. A. & Commander, K. W., *Nonlinear bubble dynamics*, J. Acoust. Soc. Am., 1988, **83**, 502-514

[36] Prosperetti, A. & Hao Y., *Modelling of spherical gas bubble oscillations and sonoluminescence*, Phil. Trans. R. Soc. Lond. A, 1999, **357**, 203-223

[37] Eller, A. I., *Damping constants of pulsating bubbles*, J. Acoust. Soc. Am., 1970, **47**, 1469-1470

[38] Breitz, N. & Medwin, H., *Instrumentation for* in situ *acoustical measurements of bubble spectra under breaking waves*, J. Acoust. Soc. Am., 1989, **86**(2), 739-743

[39] Farmer, D. M., Vagle, S., & Booth, A.D., *A free-flooding acoustical resonator for measurement of bubble size distributions*, J. Atmos. Oc. Tech., 1998, **15**, 1132-1146

[40] Dumbrell, H. A., *Comparison of excess attenuation and backscatter measurement of ship wakes*, in 'Natural physical processes associated with sea surface sound' ed. T. G. Leighton, 1997, University of Southampton, 171-178

[41] Lamarre, E. & Melville, M.K., *Sound speed measurements near the ocean surface. Instrumentation for the measurement of sound speed near the ocean surface*, J. Acoust. Soc. Am., 1994, **96**, 3605-3616

[42] Farmer, D.M. & Vagle, S., *Bubble measurements using a resonator system*, in 'Natural physical processes associated with sea surface sound' ed. T.G. Leighton, 1997, University of Southampton, 155-162

[43] Farmer, D.M. & Vagle, S. *Waveguide propagation of ambient sound in the ocean-surface bubble layer*, J. Acoust. Soc. Am., 1989, **86**, 1897-1908

[44] Deane, G.B. & Stokes, M. D., *Air entrainment processes and bubble size distributions in the surf zone*, J. Phys. Oc., 1999, **29**, 1393-1403

[45] Phelps, A. D. & Leighton, T.G. *Oceanic Bubble Population Measurements Using a Buoy-Deployed Combination Frequency Technique*. IEEE J. Oc. Eng., 1998, **23**(4), 400-410

[46] Johnson, B.D. & Cooke, R.C., *Bubble populations and spectra in coastal waters; a photographic approach*, J. Geophys. Res., 1979, **84**(C7), 3761-3766

[47] Tikhonov, A.N. & Arsenin, V.Y., *Solution of ill-posed problems*, 1977, Wiley

[48] Hansen, P.C., *Analysis of discrete ill-posed problems by means of the L-curve*, 1992, SIAM Rev., **34**(4), 561-580

[49] Hansen, P. C., *Rank-deficient and discrete ill-posed problems: Numerical aspects of linear inversion*, 1998, SIAM

[50] Fahy, F. & Walker, J., *Fundamentals of Noise and Vibration*, 1998, E & FN Spon, §7.2.2.5(c)

[51] Leighton, T. G., Ramble, D.G., Phelps, A.D., Morfey, C.L. & Harris, P. P., *Acoustic detection of gas bubbles in a pipe*, Actu Acustica, 1998, **84**, 1897-1908

[52] Leighton, T. G., White, P. R., Morfey, C. L., Clarke, J. W. L., Heald, G. J., Dumbrell, H. A. & Holland, K. R. *The effect of reverberation on the damping of bubbles*, J. Acoust. Soc. Am., 2002, **112(4)**, 1366-1376

[53] Crum, L.A., *Bjerknes forces on bubbles in a stationary field*, J. Acoust. Soc. Am., 1975, **57**(6), 1363-1370

[54] Rubinstein, J., *Bubble interaction effects on waves in bubbly liquids*, J. Acoust. Soc. Am., 1985, **77**(6), 2061-2066

[55] Yoon, S.W., Crum, L.A., Prosperetti, A. & Lu, N.Q., *An investigation of the collective oscillations of a bubble cloud*, J. Acoust. Soc. Am., 1991, **89**(2), 700-706

[56] Longuet-Higgins, M.S., *Nonlinear damping of bubble oscillations by resonant interaction*, J. Acoust. Soc. Am., 1992, **91**(3), 1414-1422

[57] Feuillade, C., *Scattering from collective modes of air bubbles in water and the physical mechanism of superresonances*, J. Acoust. Soc. Am., 1995, **98**(2), 1178-1189

[58] Feuillade, C., *The attenuation and dispersion of sound in water containing multiply interacting air bubbles*, J. Acoust. Soc. Am., 1996, **99**(6), 3412-3430

[59] Ilinskii, Y.A. & Zabolotskaya, E.A., *Cooperative radiation and scattering of acoustic waves by gas bubbles in liquids*, J. Acoust. Soc. Am., 1992, **92**(5), 2837-2841

[60] Kapodistrias G. & Dahl, P. H., *Effects of interaction between two bubble scatterers*, J. Acoust. Soc. Am., 2000, **107**(6), 3006-3017

[61] Ye., Z. *Acoustic scattering by periodic arrays of air-bubbles*, Acta Acustica, 2003, **89**, 435-444

[62] Kargl, S. G., *Effective medium approach to linear acoustics in bubbly liquids*, J. Acoust. Soc. Am., 2002, **111**(1), 168-173

[63] Ye., Z. & Ding, L. *Acoustic dispersion and attenuation relations in bubbly mixture*, J. Acoust. Soc. Am., 1995, **98**, 1629-1636

[64] Henyey, F. S., *Corrections to foldy's effective medium theory for propagation tin bubble clouds and other collections of very small scatterers*, J. Acoust. Soc. Am., 1999, **105**, 2149-2154

[65] Leighton, T. G., Meers, S. D. & White, P. R., *Propagation through nonlinear time-dependent bubble clouds, and the estimation of bubble populations from measured acoustic characteristics*. Proc. R. Soc. Lond. A. 2004, **460**, 2521-2550

[66] Oppenheim, A.V. & Schafer, R.W., *Discrete-Time Signal Processing*, 1989, Prentice-Hall

[67] Kinsler, L.E., Frey, A.R., Coppens, A.B. & Sanders JV, *Fundamentals of Acoustics*, 1999, Wiley

[68] Silberman, E., *Sound velocity and attenuation in bubbly mixtures measured in standing wave tubes*, J. Acoust. Soc. Am., 1957, **29**, 925-933

[69] Doust, P.E. & Dix, J.F., *The impact of improved transducer matching and equilisation techniques on the accuracy and validity of underwater measurements*, In 'Acoustical Oceanography' (eds. T. G. Leighton, G. J. Heald, H. Griffiths & G. Griffiths), Proc. Inst. Acoust., 2001, **23**(2), 100-109

[70] Mole, J.H., *Filter Design Data for Communications Engineers*, 1952, E & F Spon, 233-246

[71] Fano, R.M., *Theoretical Limitation on the Broadband Matching of Arbituary Impedances*, Proc. J. Franklin Inst., 1950, **249**, 57-83

[72] Leighton T. G., Meers S. D., Simpson M. D., Clarke J. W. L., Yim G. T., Birkin P. R., Watson Y. E., White P. R., Heald G. J., Dumbrell H. A. , CulverR. L. & Richards S. D. *The Hurst Spit experiment: The characterisation of bubbles in the surf zone using multiple acoustic techniques*, In 'Acoustical Oceanography' (eds. T. G. Leighton, G. J. Heald, H. Griffiths & G. Griffiths), Proc. Inst. Acoust., 2001, **23**(2), 227-234

[73] Yim, G. T., White, P. R. & Leighton, T. G. *Estimation of the time, location and natural frequency of entrained bubbles, through identification*

of individual bubble signitures in a severely overlapping, noisy surf zone environment, in 'Acoustical Oceanography' (eds. T. G. Leighton, G. J. Heald, H. Griffiths & G. Griffiths), Proc. Inst. Acoust., 2001, **23**(2), 250-256

[74] Birkin, P. R., Watson, Y. E., Smith, K. L., Leighton, T. G. & Simpson, M. D. *Measurement of species flux from a bubble using an acousto-electrochemical technique*, in 'Acoustical Oceanography' (eds. T. G. Leighton, G. J. Heald, H. Griffiths & G. Griffiths), Proc. Inst. Acoust., 2001, **23**(2), 242-249

[75] Meers, S. D., Leighton, T. G., Clarke, J. W. L., Heald, G. J., Dumbrell, H. A. & White, P. R., *The importance of bubble ring-up and pulse length in estimating the bubble distribution from acoustic propagation measurements*, in 'Acoustical Oceanography' (eds. T. G. Leighton, G. J. Heald, H. Griffiths & G. Griffiths), Proc. Inst. Acoust., 2001, **23**(2), 235-241

[76] Richards, S. D., Heathershaw, A. D. & Thorne, P. D. *The effects of suspended particulate matter on sound attenuation in seawater*, J. Acoust. Soc. Am., 1996, **100**, 1447-1450

[77] Richards, S. D. & Leighton, T. G., *Acoustic sensor performance in coastal waters: solid suspensions and bubbles*, in 'Acoustical Oceanography' (eds. T. G. Leighton, G. J. Heald, H. Griffiths & G. Griffiths), Proc. Inst. Acoust., 2001, **23**(2), 399-406

[78] Thorne, P. D. & Hardcastle, P. J., *Acoustic measurements of suspended sediments in turbulent currents and comparison with in-situ samples*, J. Acoust. Soc. Am., 1997, **101**, 2603-2614

[79] Thorne, P. D., Watkins, P. K. & Williams, J. J., *A study of intra-wave suspended sediment entrainment using acoustics*, in 'Acoustical Oceanography' (eds. T. G. Leighton, G. J. Heald, H. Griffiths & G. Griffiths), Proc. Inst. Acoust., 2001, **23**(2), 415-422

[80] Thorpe, S., *On the clouds of bubbles formed by breaking wind-waves in deep water, and their role in air-sea gas transfer*, Phil. Trans. R. Soc. Lond A, 1982, **304**, 155-210

[81] Akulichev, V.A., Bulanov, V.A. & Klenin, S.A., *Acoustic sensing of gas bubbles in the ocean medium*, Sov. Phys. Acoust, 1986, **32**(3), 177-180

[82] Pace, N.G., Cowley, A. & Campbell, A.M., *Short pulse acoustic excitation of microbubbles*, J. Acoust. Soc. Am., 1997, **102**(3), 1474-1479

[83] Suiter, H.R., *Pulse length effects on the transmissivity of bubbly water*, J. Acoust. Soc. Am., 1992, **91**(3), 1383-1387

[84] Caruthers, J. W., Stanic, S. J., Elmore, P. A. & Goodman, R. R., *Acoustic attenuation in very shallow water due to the presence of bubbles in rip currents*, J. Acoust. Soc. Am., 1999, **106**(2), 617-625.

[85] Leighton, T. G., *Nonlinear Bubble Dynamics And The Effects On Propagation Through Near-Surface Bubble Layers*, in 'High-Frequency Ocean Acoustics' (Eds. M.B. Porter, M. Siderius, and W. Kuperman), 2004, American Institute of Physics, Melville, New York